AUTOHESION MODEL FOR THERMOPLASTIC COMPOSITES

by

Min-Chung Li

Thesis submitted to the Faculty of the

Virginia Polytechnic Institute and State University

in partial fulfillment of the requirements for the degree of

Master of Science

in

Engineering Mechanics

APPROVED:

Alfred C. Loos, Chairman

John C. Duke, Jr.

Michael W. Hyer

November, 1989

Blacksburg, Virginia

AUTOHESION MODEL FOR THERMOPLASTIC COMPOSITES

by

Min-Chung Li

Alfred C. Loos, Chairman

Engineering Mechanics

(ABSTRACT)

A non-isothermal autohesion model was developed by combining a transient finite element heat transfer model with the isothermal autohesion model. Heat transfer analyses and the interfacial strength development analyses were conducted using the non-isothermal autohesion model on a polysulfone (Udel P1700) compact tension specimen, a 64-ply graphite (Thornel T300)/P1700 unidirectional composite, and a 192-ply graphite (Hercules AS4)/P1700 unidirectional composite. A 64-ply T300/P1700 unidirectional composite was processed in a matched metal mold. Temperature data were taken and compared with the calculated values. Good agreement was observed between the calculated and the measured temperature values.

A healing test which aimed at studying the interply bond development in AS4/P1700 unidirectional composites was performed. The double cantilevered beam (DCB) Mode I fracture toughness test was selected. The DCB specimens were fractured and healed in a special fixture with different combinations of temperature, pressure, and time. The healed DCB specimens were refractured and the critical strain energy release rates (G_{IC}) were measured. The pressure was found to be a key factor in the healing process. Temperature and time dependencies of the interply bond development were also observed.

The non-isothermal autohesion model predicted a higher strength achieved in a shorter time. This was due to the extra time which was needed for the fracture interface to achieve intimate contact, and the assumption of the initial intimate contact achievement of the non-isothermal autohesion model.

Acknowledgements

I wish to express my gratitude to Dr. Alfred C. Loos, my major advisor and chairman of the graduate committee, for his continuing support and encouragement throughout the course of this research. A very strong debt of gratitude is also owed to the other two members of my graduate committee, Dr. John C. Duke, Jr. and Dr. Michael W. Hyer. Their willingness to help me is greatly appreciated. The work was sponsored by Virginia Institute for Material Systems (VIMS) and NSF Science and Technology Center; High-Performance Polymeric Adhesives and Composites. I am also grateful to the NASA Langley Research Center and Amoco Performance Products for donating materials. Finally, I want to express my appreciation to the constant help and have given me. Without their help, the experimental work could not have been completed.

Table of Contents

1. Introduction 1

2. Literature Review 5

2.1 Autohesion 5

2.2 Autohesion Test Methods 7

3. Non-isothermal Autohesion Model for Amorphous Thermoplastic Resin 10

3.1 Compact Tension Specimen Heat Transfer Analysis 11

3.2 Isothermal Autohesion Model 15

3.3 Non-isothermal Autohesion Model 22

4. Double Cantilevered Beam Test and Autohesive Bonding of Thermoplastic Matrix Composites 31

4.1 Literature Review 32

4.2 Sample Preparation 37

4.2.1 Solvent Removal 37

4.2.2 Laminate Consolidation 39

4.2.3 NDT Evaluation of the panels 39

4.2.4 DCB Specimens 44
4.3 Testing Procedures 44
4.4 Healing Procedures 47
4.5 Results 49
4.5.1 Double Cantilevered Beam Test 49
4.5.2 Ultrasonic C-Scan 54
4.5.3 Microscopy of the Cross-Sections of the Undamaged and Healed Specimens 54
4.5.4 Scanning Electron Microscopy 56

5. Non-Isothermal Autohesion Model for Amorphous Thermoplastic Composites 64
5.1 Heat Transfer Analysis of Thermoplastic Composite Material 65
5.1 Micromechanics Equations for Thermal Properties of Composites 70
5.3 Experimental Procedures 72
5.4 Comparison Between Heat Transfer Analysis and Experimental Data 75

6. Summary of Results 95

Reference 98

Vita 101

List of Illustrations

Figure 1. Typical processing cycle for a thermoplastic composite. 3

Figure 2. Schematic of autohesive bond development across an interface. 6

Figure 3. Dimensions of CT specimen based on the ASTM Standard Test Method for Plane-Strain Fracture Toughness of Metallic Materials (E 399-81). 12

Figure 4. Coordinate system used in the heat transfer analysis of the CT specimen 14

Figure 5. Finite element mesh and the boundary conditions used in the heat transfer analysis of the CT specimen. 16

Figure 6. Comparison between the calculated and measured results of temperature variation at the center of the polysulfone CT specimen. Data reported by Howes and Loos [2]. 17

Figure 7. Temperature distribution of the polysulfone CT specimen across the crack surface being bonded. The bonding temperature is 245°C. 18

Figure 8. Temperature distribution of the polysulfone CT specimen along the vertical centerline (y-axis). The bonding temperature is 245°C. 19

Figure 9. Healing function, R versus square root of time. Symbols represent data from reference 2. Solid lines represents the isothermal healing model solution. 21

Figure 10. Flowchart of non-isothermal autohesion model. 24

Figure 11. Healing function, R versus square root of time for polysulfone CT specimens bonded at 196°C. Comparison between data (symbols) and the non-isothermal autohesion model (solid line). 25

Figure 12. Healing function, R versus square root of time for polysulfone CT specimens bonded at 200°C. Comparison between data (symbols) and the non-isothermal autohesion model (solid line). 26

Figure 13. Healing function, R versus square root of time for polysulfone CT specimens bonded at 205°C. Comparison between data (symbols) and the non-isothermal autohesion model (solid line). 27

Figure 14. Healing function, R versus square root of time for polysulfone CT specimens bonded at 213.5°C. Comparison between data (symbols) and the non-isothermal autohesion model (solid line). 28

Figure 15. Healing function, R versus square root of time for polysulfone CT specimens bonded at 225°C. Comparison between data (symbols) and the non-isothermal autohesion model (solid line). 29

Figure 16. Healing function, R versus square root of time for polysulfone CT specimens bonded at 245°C. Comparison between data (symbols) and the non-isothermal autohesion model (solid line). 30

Figure 17. Load-deflection relation for an linear elastic, isotropic cantilevered beam. 36

Figure 18. Solvent removal bagging assembly on the tool plate of the autoclave. 38

Figure 19. Matched mold laminate consolidation assembly. 40

Figure 20. C-scan result of a good 152.4 mm X 152.4 mm panel. 41

Figure 21. C-scan result of a "bad" 152.4 mm X 152.4 mm panel. 42

Figure 22. C-scan result of the panel shown in Figure 21 after reprocessing. 43

Figure 23. Schematic diagram of the DCB specimen. 45

Figure 24. Typical chart recorder output from DCB test for one specimen. 46

Figure 25. Healing assembly of the DCB specimen. 48

Figure 26. Healing function versus pressure for AS4/P1700 unidirectional composites bonded at 245°C for (a)30 minutes and (b)60 minutes. 51

Figure 27. Healing function versus time for AS4/P1700 unidirectional composites bonded at 245°C and 690 kPa (100 psi). 52

Figure 28. Healing function versus temperature for AS4/P1700 unidirectional composites bonded at 2068 kPa (300 psi) and 30 minutes. 53

Figure 29. Ultrasonic C-scan results of typical AS4/P1700 unidirectional DCB specimens bonded at different set of parameters. Kapton inserts are at the left ends of the specimens. 55

Figure 30. Cross-sections of (a)undamaged specimen at 100X, (b)specimen healed at 245°C/690kPa(100psi)/60min at 50X. 57

Figure 31. Cross-sections of specimens healed at (a)245°C/6895kPa(1000psi)/60min at 1000X, (b)288°C/2068kPa(300psi)/30min at 250X. 58

Figure 32. Fracture surface of undamaged specimen. 60

Figure 33. Fracture surface of specimens healed at (a)288°C/2068kPa(300psi)/30min, (b)245°C/2068kPa(300psi)/30min. 61

Figure 34. Fracture surface of specimens healed at (a)288°C/2068kPa(300psi)/30min, (b)245°C/690kPa(100psi)/60min. 62

Figure 35. Fracture surface of specimens healed at 343°C/2068kPa(300psi)/30min. 63

Figure 36. Coordinate system used in the heat transfer analysis of the matched metal mold consolidation assembly. 66

Figure 37. Simplified schematic of unidirectional prepreg and the coordinate system. [32] . . . 67

Figure 38. Cross-section of the 64-ply T300/P1700 unidirectional composite processing assembly and locations of the thermocouples. 73

Figure 39. Top-view of the 64-ply T300/P1700 unidirectional composite processing assembly and the locations of the thermocouples. 74

Figure 40. C-scan results of the 64-ply T300/P1700 unidirectional composite after the second process. 76

Figure 41. Finite element mesh and boundary conditions used in the consolidation simulation of the 64-ply T300/P1700 unidirectional composite. 78

Figure 42. Upper and lower boundary conditions of the 64-ply T300/P1700 unidirectional composite processing assembly. 79

Figure 43. Temperature versus time at five positions in a 64-ply T300/P1700 unidirectional composite. Comparisons between the data (symbols) and the results computed by the model (solid lines). (RUN #1) 82

Figure 44. Temperature versus time at five positions in a 64-ply T300 P1700 unidirectional composite. Comparisons between the data (symbols) and the results computed by the model (solid lines). (RUN #2) 83

Figure 45. Temperature versus time at three positions along the fiber direction in a 64-ply T300/P1700 unidirectional composite. (RUN #1) 84

Figure 46. Temperature versus time at three positions along the fiber direction in a 64-ply T300/P1700 unidirectional composite. (RUN #2) 85

Figure 47. Temperature versus time at the convective boundaries of a 64-ply T300/P1700 unidirectional composite. Comparisons between the data (symbols) and the results computed by the model (solid lines). 86

Figure 48. Model estimation of interply strength development for the RUN #1 test at five positions in the 64-ply T300/P1700 unidirectional composite. 87

Figure 49. Cross-section of the 192-ply AS4/P1700 unidirectional composite processing assembly. 90

Figure 50. Temperature versus time at two positions inside a 192-ply AS4/P1700 unidirectional composite. The processing temperature is 288°C. 91

Figure 51. Temperature distribution along the horizontal centerline (y-axis) of the 192-ply AS4/P1700 unidirectional composite. The processing temperature is 288°C. . . . 92

Figure 52. Temperature distribution along the vertical centerline (z-axis) of the 192-ply AS4/P1700 unidirectional composite. The processing temperature is 288°C. . . . 93

Figure 53. Model estimation of interply strength development at two positions in the 192-ply AS4/P1700 unidirectional composite. The processing temperature is 288°C. . . . 94

List of Tables

Table 1. Comparison of thermosetting and thermoplastic matrix composites.[1,2] 2

Table 2. Test matrix of DCB healing experiments. 49

Table 3. Material properties used in analyzing heat transfer in a unidirectional 64-ply T300/P1700 composite. 77

1. Introduction

Use of advanced composites has increased significantly in recent years. High specific strength and stiffness make composites ideal for many aerospace applications. Fiber-reinforced organic matrix composites which commonly use thermosetting resins, such as epoxies, have some inherent deficiencies. These include the need for multistep processing, limited shelf-life, low toughness , sensitivity to moisture, and inability to reprocess or reform the material [1].

In recent years considerable attention has been focused on the use of tough, high-temperature, solvent-resistant thermoplastic polymers as matrix materials for fiber-reinforced composites. The increased toughness of thermoplastic resins can subsequently improve the damage tolerance of composites. However, the mechanisms describing consolidation and interply bonding during processing of thermoplastic matrix composites are quite different than the mechanisms observed during cure of thermosetting matrix composites. Extreme tow height nonuniformity and lack of flow make thermoplastic prepregs more difficult to process than thermosetting prepregs. Unlike thermosetting resins, which rely on low viscosity and high flow of the resin to coalesce the ply interfaces, thermoplastic matrix prepregs must be physically deformed to cause intimate contact and coalescence of the ply interfaces. Table 1 shows a comparison between thermosetting and thermoplastic matrix composites.

Table 1. Comparison of thermosetting and thermoplastic matrix composites.[1,2]

	Thermosetting Resin Composites	Thermoplastic Resin Composites
Neat Resin	•minimum viscosity is low ($\simeq$10 poise) •flow of resin is high	•minimum viscosity is high ($\simeq 10^4$ poise) •flow of resin is very low
Prepregs (or raw materials)	•uniform •requires refrigerated storage	•nonuniform •ambient storage anywhere
Processing	•chemical reaction during cure (irreversible) •low processing temperature (250-350°F)	•no reaction during consolidation(reversible) •high processing temperature (600-700°F)
Laminates (or finished parts)	•cannot be reformed •absorbs moisture	•multiple reforming possible •virtually no moisture absorption

Techniques commonly used to manufacture composites from prepregs include compression molding and vacuum-bagged autoclave molding. The prepreg is cut to the dimensions of the structure and the fiber directions oriented to obtain the required mechanical properties of the finished product. The lay-up is then placed in a rigid mold (compression molding) or vacuum-bagged (autoclave molding) and processed at an elevated temperature and pressure for a known period of time, called the processing cycle. A typical processing cycle for a thermoplastic composite is shown in Figure 1.

The composite is heated at a constant rate from room temperature to an elevated temperature above the glass transition temperature (T_g) of the thermoplastic matrix resin. At some point during the processing cycle the consolidation pressure is applied. The composite is held for a specified period of time under elevated temperature and pressure to allow for intimate contact, coalescence, and complete autohesive bonding of the ply interfaces. At this point the consolidated composite is cooled under pressure to below the T_g of the matrix.

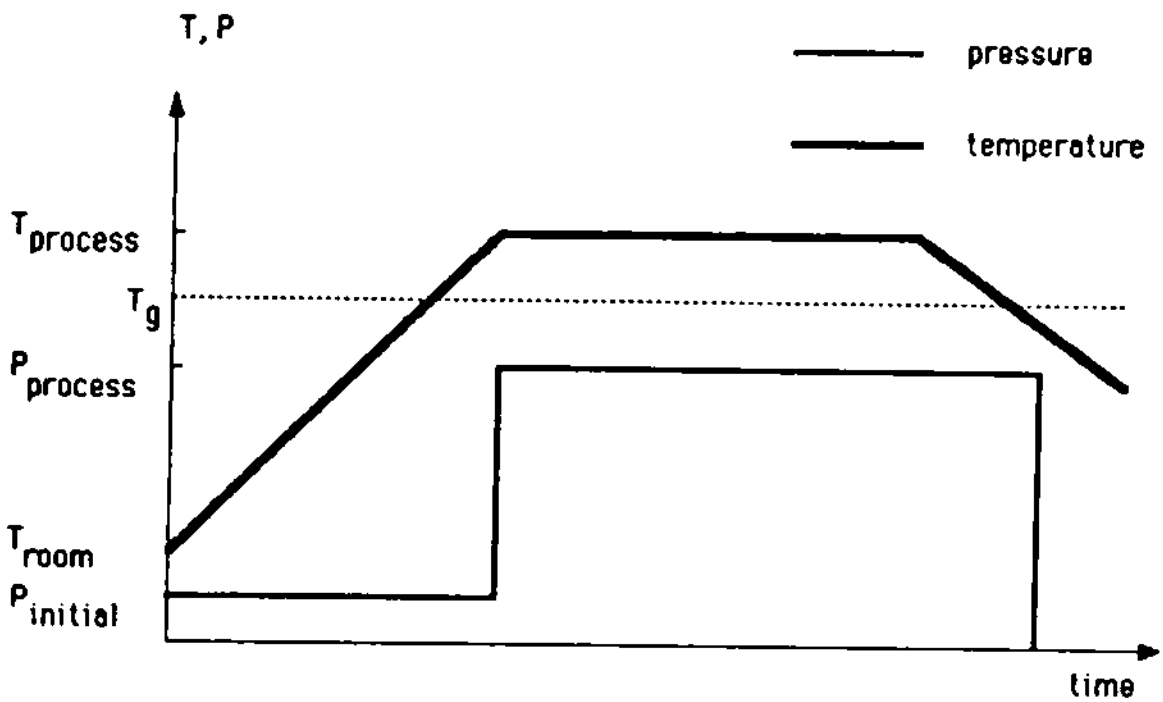

Figure 1. Typical processing cycle for a thermoplastic composite.

Processing cycles for thermoplastic composites are often derived empirically by trial and error. These methods do not necessarily lead to processing cycles that result in fully consolidated composite structures with strong interply bonds. In order to improve the processing theory for continuous fiber-reinforced thermoplastic matrix composites, the processing parameters, temperature, pressure, and time must be related to the overall state of consolidation in the composite.

In development of a processing model, the physical processes that occur during production of thermoplastic composites must be understood fully. The mechanism controlling interply bond formation (consolidation) during processing of a thermoplastic composite has been recognized as autohesion or self-diffusion [3]. Theories describing autohesion in thermoplastic resins have been developed. Test methods to measure autohesive bond development in neat resins as a function of processing temperature and time are well characterized. Thus, the first objective of this investigation was to develop a model for non-isothermal processing of thermoplastic composites by incorporating a transient heat transfer analysis into a model for isothermal autohesive bond development in amorphous thermoplastic resins. A second objective was to use the results of the model in conjunction with experimental tests to investigate autohesion in fiber-reinforced amorphous thermoplastic prepregs. In this study, a double cantilevered beam interlaminar fracture toughness test is used to characterize autohesion in fiber-reinforced amorphous thermoplastic prepregs.

2. Literature Review

In previous studies of thermoplastic composite processing, it has been established that individual prepreg plies consolidate by interply bonding [4]. The resulting bond strength is a function of the processing parameters, temperature, pressure, and time to which the interface is subjected. The mechanism governing the formation of interply bonds has been established as autohesion or self-diffusion [3]. The following is a brief summary of the results of previous investigations on autohesion in thermoplastic polymers and fiber-reinforced thermoplastic composites as reported in the literature.

2.1 Autohesion

Autohesive bonding is controlled by two mechanisms: (1) intimate contact between the interfacial surfaces, and (2) diffusion of the macromolecules across the interface [3]. Figure 2 shows the phenomenon of autohesion for an amorphous thermoplastic polymer. At time zero, the two surfaces are pressed together. Providing the temperature is high enough (normally above the glass transition

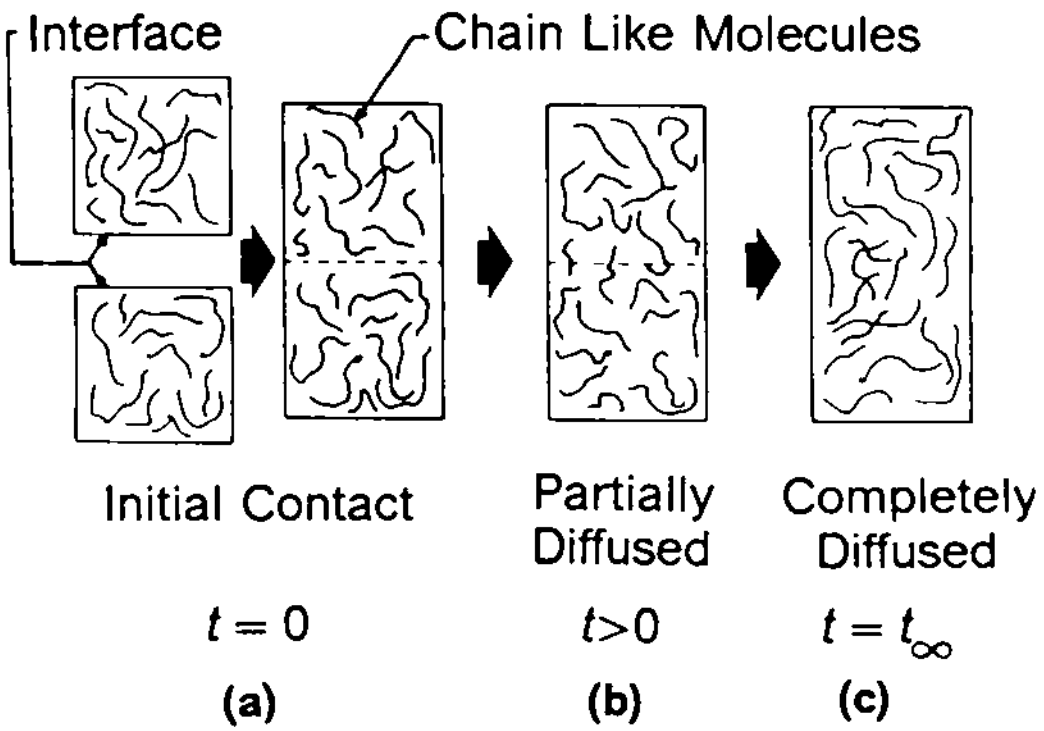

Figure 2. Schematic of autohesive bond strength development across an interface.

temperature, T_g), the surfaces will deform viscoelastically, come into contact, and wet (Fig. 2a). The polymer chains will begin to diffuse across the interface due to random thermal motions. After time has passed, the chains will have partially diffused across the interface and entangled with molecular chains on the other side of the interface, thus giving the interface strength (Fig. 2b). Following a long period of time, the polymer chains will have penetrated and entangled into the adjacent interface so that the interface is no longer distinguishable from the bulk polymer. At this point, the interface is considered completely healed (Fig. 2c).

Either wetting or diffusion can account for significant portions of the interfacial strength. Diffusion is conditional upon the surfaces being in intimate contact, as the molecules cannot move across open space [5]. Theories describing polymer diffusion are based on De Gennes' reptation theory of molecular motion [6]. Wool [5,7], Wool and O'Connor [8-10], Prager and Tirrell [11], and Jud et al. [12] have developed theories explaining strength development of a polymer-polymer interface and crack healing in thermoplastic polymers. These studies resulted in basic mathematical relationships between autohesive bond development, temperature , and contact time.

2.2 Autohesion Test Methods

Destructive mechanical tests commonly are used to characterize autohesion of high polymers. In the mechanical tests, two polymer surfaces normally are pressed together at a given temperature for a specified length of time. The fracture stress or fracture energy of the interface then is measured using the appropriate test.

Tack measurement were used by Skewis [13], Bauer [14], and Rhee and Andries [15] to measure interfacial tensile strength of two surfaces that have been pressed together under pressure for a

specified time. The tack tests were performed at room temperature, well above T_g of the elastomers studied.

Fracture toughness tests were performed by Wool and O'Connor [9,10], Jud et al. [12] and Howes and Loos [2]. Wool and O'Connor studied healing of elastomers using double cantilevered beam toughness tests, and healing of PMMA and polystyrene using Izod impact tests. The specimens were healed above the T_g of the polymer in question. Jud et al. used a compact tension fracture toughness test to measure autohesion in healed PMMA specimens. The specimens were healed in a hot press at temperatures above the T_g of PMMA (approximately 100 °C). Howes and Loos used a compact tension fracture toughness test to measure autohesion in healed polysulfone specimens. The specimens were healed in a force air convection oven at temperatures above the T_g of polysulfone.

Hamed [16] investigated tack formation in elastomers using a T-peel test. A T-peel test measures the energy required per unit area to separate the two surfaces. The polymer was dissolved in a solvent and spread on a flexible base. Two strips of the polymer/base material were pressed together for a measured time and then the strips were separated in a tension testing machine.

Interfacial tests were performed by Wool and O'Connor [10], Boenig et al. [17], Loos and Dara [4], Bothe and Rehage[18], and Howes and Loos [2]. Wool and O'Connor used notched tensile bars of hydroxy-terminated polybutadiene (HTPB) that were fractured and healed to evaluate fracture stress, fracture strain, and fracture energy as a function of healing time. Boenig et al. used the ASTM Test Methods for Rubber Properties in Tension (D412-51T), type C tension test to measure tack in urethran elastomers. Dara and Loos used a parallel plate plastometer fitted with a tensile/compressive load cell to measure autohesion in polysulfone resin. The specimens were bonded at elevated temperatures and tested mechanically at the bond temperature in a nitrogen-purged atmosphere. Bothe and Rehage used a through-the-thickness tension test at room temperature to test autohesion in polybutadiene (BR), crosslinked acrylonitrile-butadiene copolymer (NBR), ethylenepropylene copolymer (EPM), and polychlorobutadiene (CR). They studied the

effects of contact pressure, contact time, polymer structure, and strain rate. Howes and Loos attempted to use an interfacial tension test based on the ASTM Test for Tensile Properties of Adhesive Bonds (D/897-78) to measure autohesion in polysulfone resin. The data obtained had very high scatter which made it difficult to correlate autohesive strength with bonding temperature and contact time. The poor results were attributed to surface irregularities, misalignment of the grips and fixtures during mechanical testing, and thermal effects.

A close examination of the literature reveals that autohesive bonding of the ply interfaces during formation of a thermoplastic composite laminate has not been studied extensively. Howes and Loos [2] used a double cantilevered beam interlaminar fracture toughness test to study autohesive bond development in AS4 graphite fiber, Udel P1700 polysulfone composites. Fractured DCB specimens were healed at temperatures above the T_g of polysulfone. Critical strain energy release rates (G_{IC}) of the healed specimens were measured. The data did not show a strong time or temperature dependance as observed in the neat resin test. Clearly, further studies on interply autohesive bond formation during processing in amorphous thermoplastic composites are needed.

3. Non-isothermal Autohesion Model for Amorphous Thermoplastic Resin

As discussed in Section 2.2, the compact tension fracture toughness test is commonly used to measure autohesive bond in thermoplastic polymers [2,12]. Precracked CT specimens are pressed together above the saturation pressure to ensure complete interfacial contact and wetting of the fractured surfaces. The specimen is then heated to the desired temperature (above T_g) and healed for the specified period of time. Due to the thermal resistance and capacitance of the CT specimen and a finite surface heat transfer coefficient, the time required for the fracture surface to reach the desired bonding temperature can be a significant portion of the total bonding time. Furthermore, when the specimen reaches T_g, bonding begins. Hence, a significant portion of the bonding process occurs during transient heating of the specimen. If the temperature distribution of the fracture surface is nonuniform, then each point of the surface will bond at different rates.

In order to accurately model autohesion in thermoplastic resins and composites the temperature distribution of the surface being bonded must be known during processing. This information can then be combined with isothermal data to model autohesion bond development during non-isothermal processing.

A model describing non-isothermal autohesive bonding for the CT specimen is presented in this chapter. Results of the model are compared with test data obtained from polysulfone (Udel P1700) CT specimens.

3.1 Compact Tension Specimen Heat Transfer Analysis

Consider the compact tension specimen shown in Figure 3. A precracked polysulfone CT specimen is placed in a metallic fixture [2] and healed at elevated temperatures. In the analysis, it is assumed that the thermal capacitance and resistance of the metallic fixture can be neglected. The outer surfaces of the CT specimen are heated by forced convection heat transfer and heat is conducted into the specimen.

The temperature distribution in the CT specimen can be determined from the unsteady heat conduction equation which includes forced convection heat transfer at the outer boundaries. If the temperature variation in the z-direction is small, then a two-dimensional heat transfer analysis can be used to calculate the temperature distribution in the x-y plane. The two dimensional transient Fourier equation can be written as follows [19]:

$$\rho C_p \frac{\partial T}{\partial t} = \frac{\partial}{\partial x}\left(k \frac{\partial T}{\partial x}\right) + \frac{\partial}{\partial y}\left(k \frac{\partial T}{\partial y}\right) \tag{3.1}$$

where ρ is the density, C_p is the specific heat, k is the thermal conductivity, T is temperature and t is time.

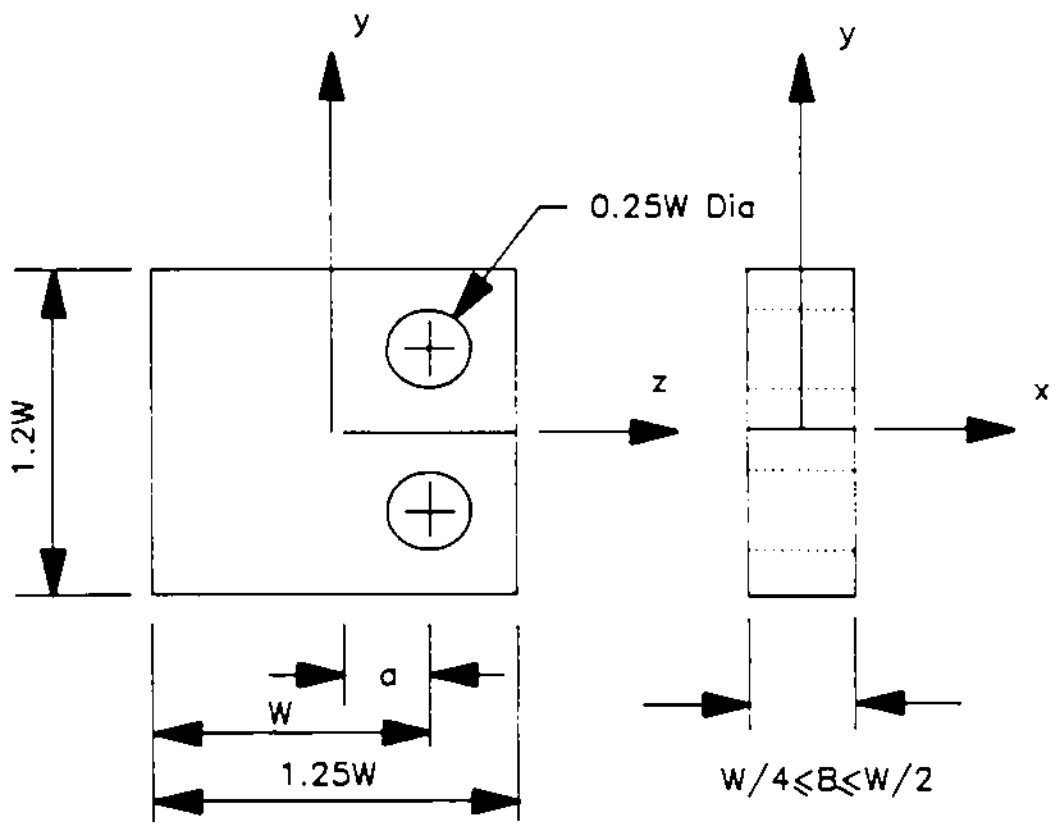

Figure 3. Dimensions of CT specimen based on the ASTM Standard Test Method for Plane-Strain Fracture Toughness of Metallic Materials (E 399-81).

Noting the thermal as well as geometric symmetry of the problem, we select the coordinate system shown in Figure 4 and analyze the shaded region.

The initial and boundary conditions may be written in the form

Initial condition:

$$T(x, y, 0) = T_i \tag{3.2}$$

Boundary conditions:

$$\frac{\partial T(0, y, t)}{\partial x} = 0 \quad ; \quad -k\frac{\partial T(b, y, t)}{\partial x} = h[T(b, y, t) - T_f] \tag{3.3}$$

$$\frac{\partial T(x, 0, t)}{\partial y} = 0 \quad ; \quad -k\frac{\partial T(x, l, t)}{\partial y} = h[T(x, l, t) - T_f] \tag{3.4}$$

where T_i is the initial temperature, h is the convective heat transfer coefficient, and T_f is the ambient temperature. Here, T_f is equivalent to the oven set point temperature.

Solution of Equation 3.1 for arbitrary time varying boundary conditions must be obtained by numerical methods. A two-dimensional finite element program FEM2D [20] was employed. The program uses a semidiscrete approximation to solve the transient heat conduction equation. A " θ " family of approximation was used to approximate the first-order time derivative. A value for θ of 0.5 was used corresponding to the Crank-Nicolson difference scheme [21].

The finite element heat transfer analysis was used to calculate the temperature distribution in a Udel P1700 polysulfone CT specimen during healing. The density, specific heat capacity, and thermal conductivity of polysulfone are 1.24×10^3 Kg/m^3, 1.13×10^3 $J/Kg^\circ C$, and 0.26 $W/m^\circ C$ respectively [2]. Dimensions of the CT specimen are shown in Figure 4 with l equal to 15.24 mm and b equal to 6.35 mm. A 14×14 mesh of four-node linear quadrilateral elements and the

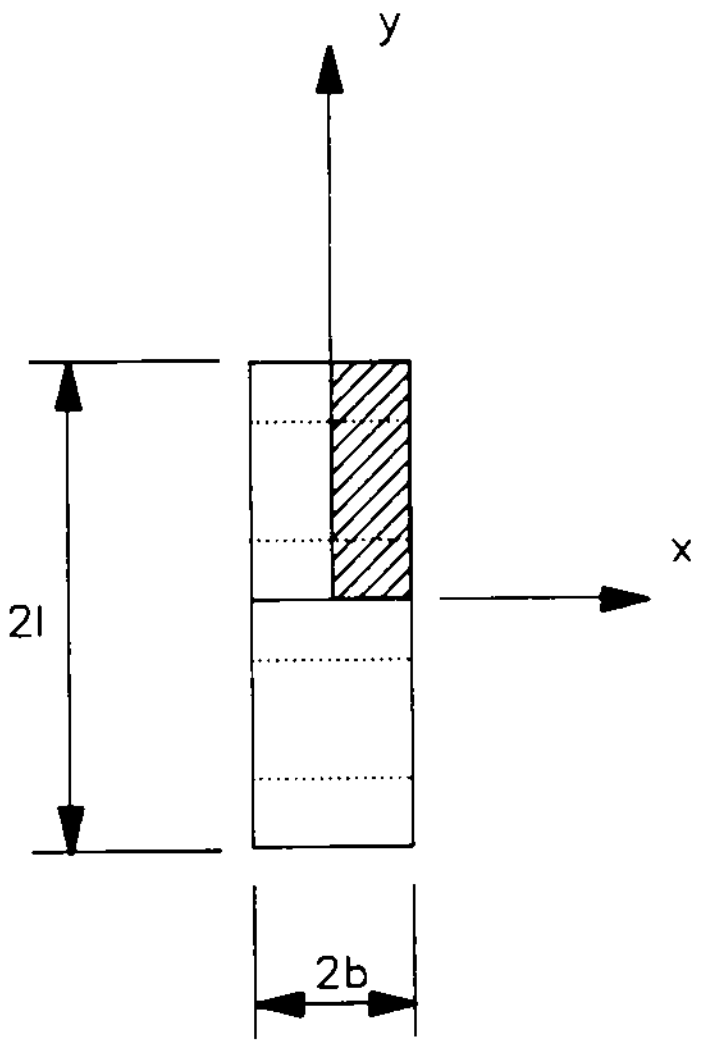

Figure 4. Coordinate system used in the heat transfer analysis of the CT specimen .

boundary conditions are shown in Figure 5. Time increments of 0.1 second were taken for the first 10 seconds of the analysis and 10 seconds thereafter.

Results of the analysis were compared with data reported by Howes and Loos [2]. Howes and Loos measured the temperature at the crack plane during healing of a polysulfone CT specimen in a forced-air convection oven. Figure 6 shows a comparison between the calculated and measured temperature at the center of the crack (position x = 0, y = 0, Figure 5) for oven set point temperatures of 200, 213.5 and 245 degrees Celsius. The heat transfer analysis gave very good correlation with the measured results. A heat transfer coefficient of 53.7 $W/m^2°C$ was used in the calculations. The heat transfer coefficient was obtained by using the FEM analysis to calculate temperature versus time for different values of the heat transfer coefficient until the calculated temperature matched data.

Results of the FEM heat transfer analysis show that during bonding the temperature distribution through the thickness of the specimen is nonuniform. The temperature distribution of the polysulfone CT specimen across the crack surface being bonded is shown in Figure 7. The processing temperature was 245°C. For these conditions, there is approximately a 20 seconds time difference between when the outer surface of the crack (x/b = 1) reaches T_g and begins to heal and the center of the crack (x/b = 0) reaches T_g. The temperature distribution along the vertical centerline (y-axis) of the polysulfone CT specimen is shown in Figure 8 for a bonding temperature of 245°C.

3.2 Isothermal Autohesion Model

Autohesive bond development in amorphous thermoplastic resins can be characterized by measuring the fracture toughness of precracked compact tension specimens that were healed at a given

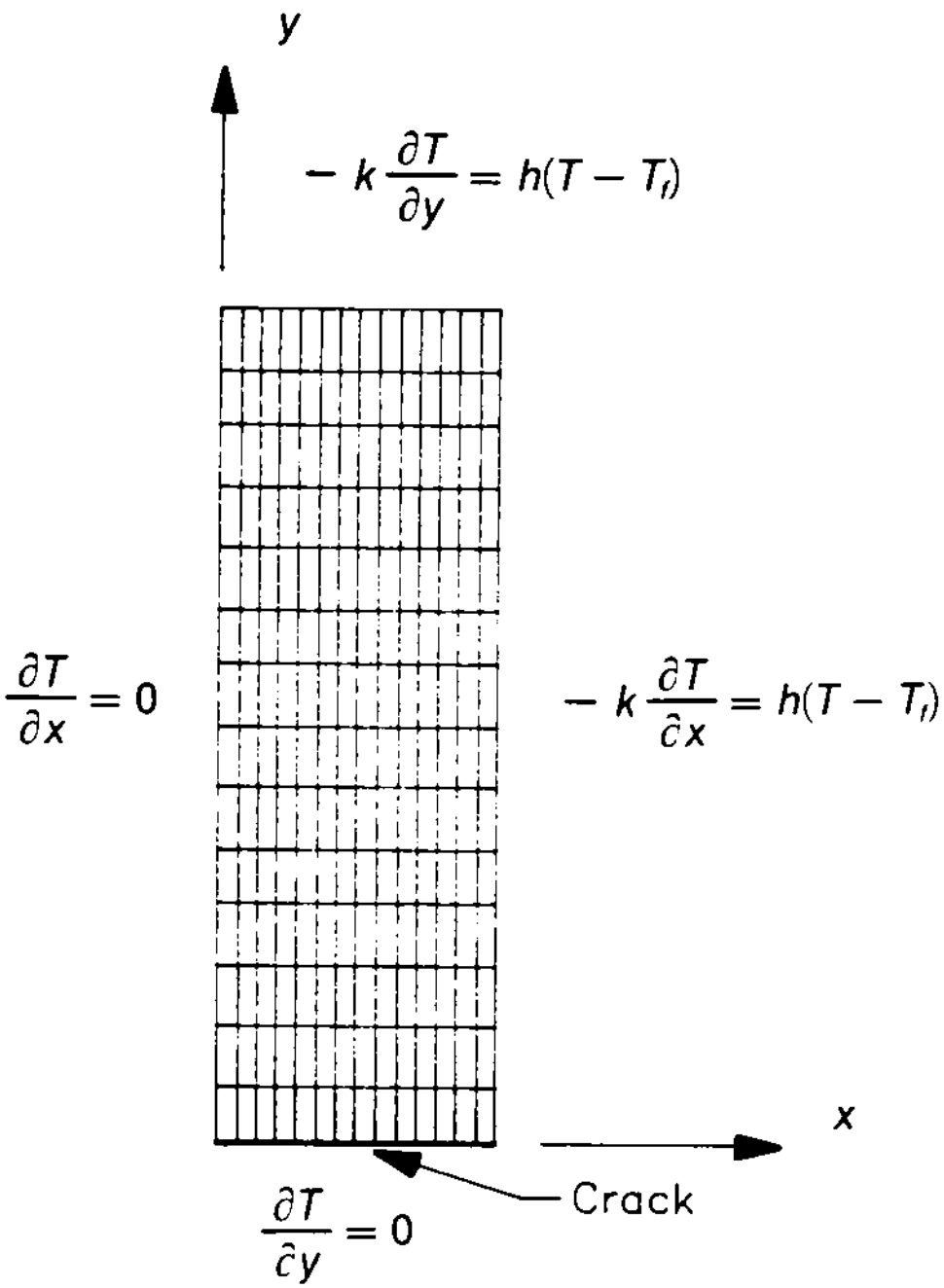

Figure 5. Finite element mesh and the boundary conditions used in the heat transfer analysis of the CT specimen.

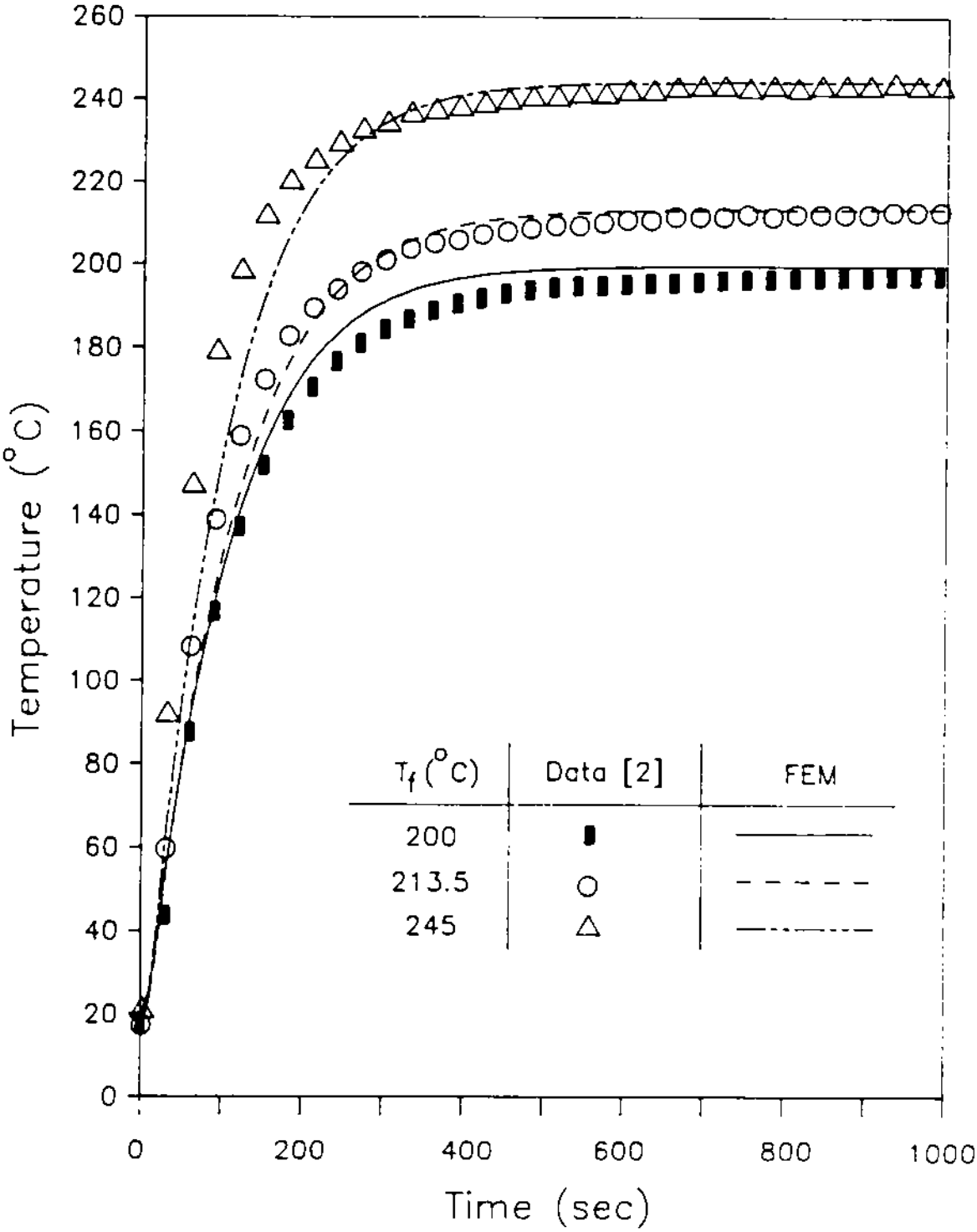

Figure 6. Comparison between the calculated and measured results of temperature variation at the center of the polysulfone CT specimen. Data reported by Howes and Loos [2].

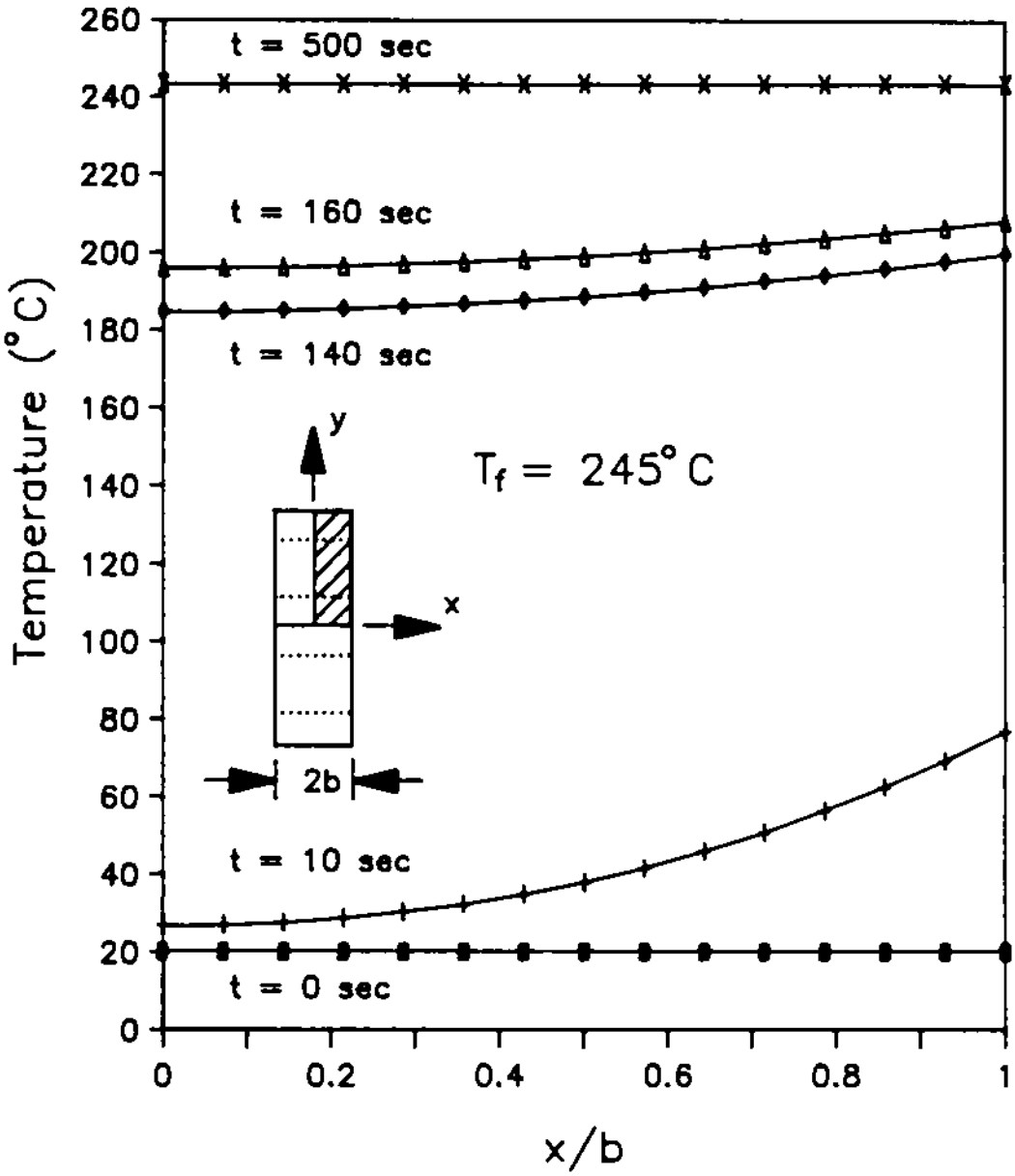

Figure 7. Temperature distribution of the polysulfone CT specimen across the crack surface being bonded. The bonding temperature is 245°C.

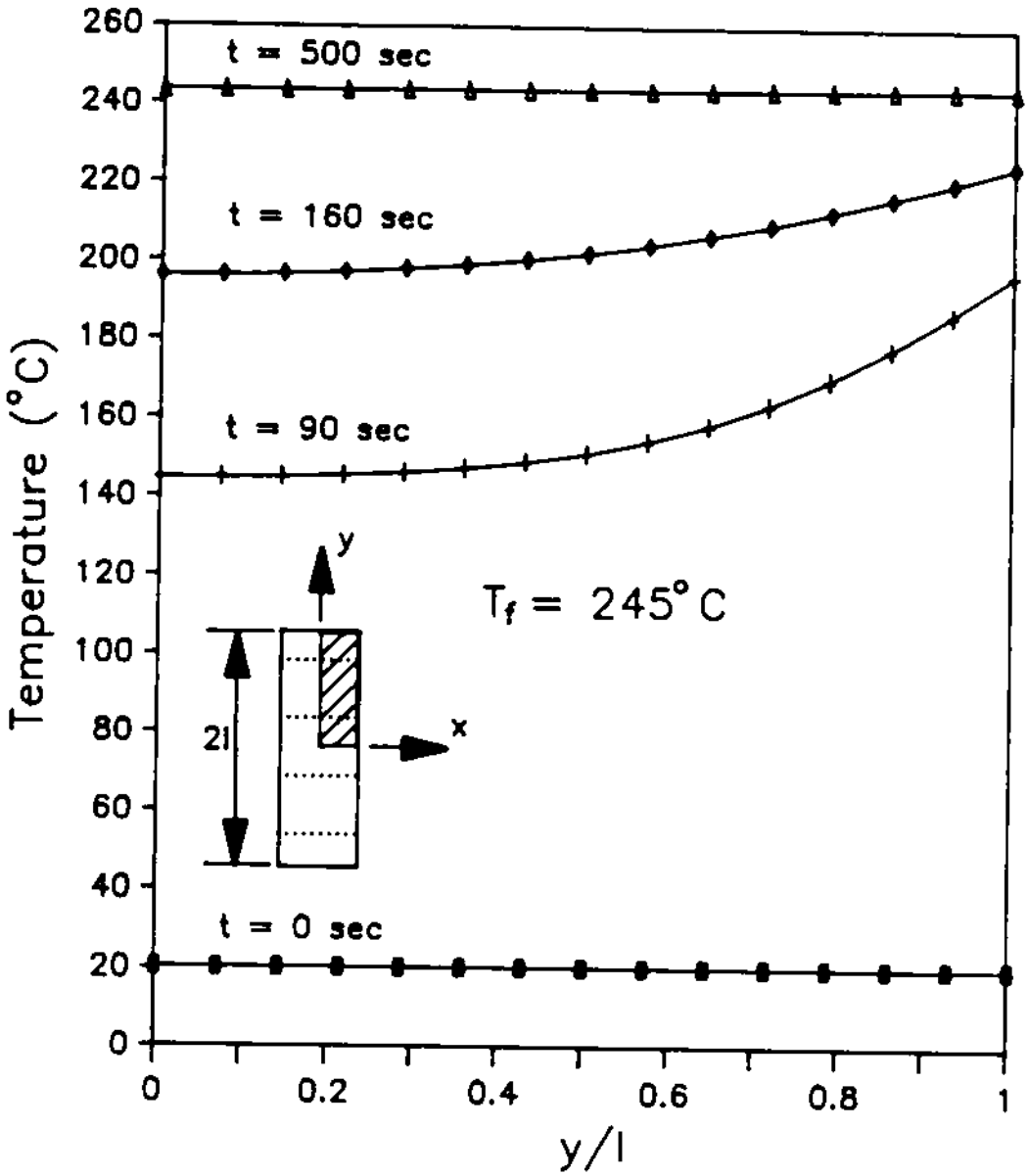

Figure 8. Temperature distribution of the polysulfone CT specimen along the vertical centerline (y-axis). The bonding temperature is 245°C.

temperature and contact time. Following this procedure, Howes and Loos [2] measured autohesive bond development in Udel P1700 polysulfone resin. If wetting is instantaneous and the instantaneous wetting load at initial time is negligible, a nondimensional healing function R can be defined as follows [5,9,10,12]

$$R = \frac{G_{IC}(t)}{G_{IC\infty}} = C(T)t^{1/2} \tag{3.5}$$

where $G_{IC}(t)$ is the critical strain energy release rate of a CT specimen healed for an amount of time t, $G_{IC\infty}$ is the critical strain energy release rate of a CT specimen healed for infinite time, $C(T)$ is a temperature dependent parameter proportional to the polymer self-diffusion coefficient, and t is healing time.

Wool and O'Connor [9] stated that the self-diffusion coefficient should follow a WLF temperature dependence providing that the mode of failure remains the same between samples healed at different temperatures between T_g and $T_g + 100°C$. Using a reference temperature of 196°C (469°K), the WLF relationship for Udel P1700 polysulfone can be written as follows [2]:

$$\log a_T = \frac{-1.604(T-469)}{11.26 + (T-469)} \tag{3.6a}$$

where

$$a_T = \frac{1.94\times10^{-5}T}{C(T)} \tag{3.6b}$$

Here, T is in absolute temperature. A comparison between the calculated and measured healing function for Udel P1700 polysulfone is shown in Figure 9. Symbols represent the experimental data

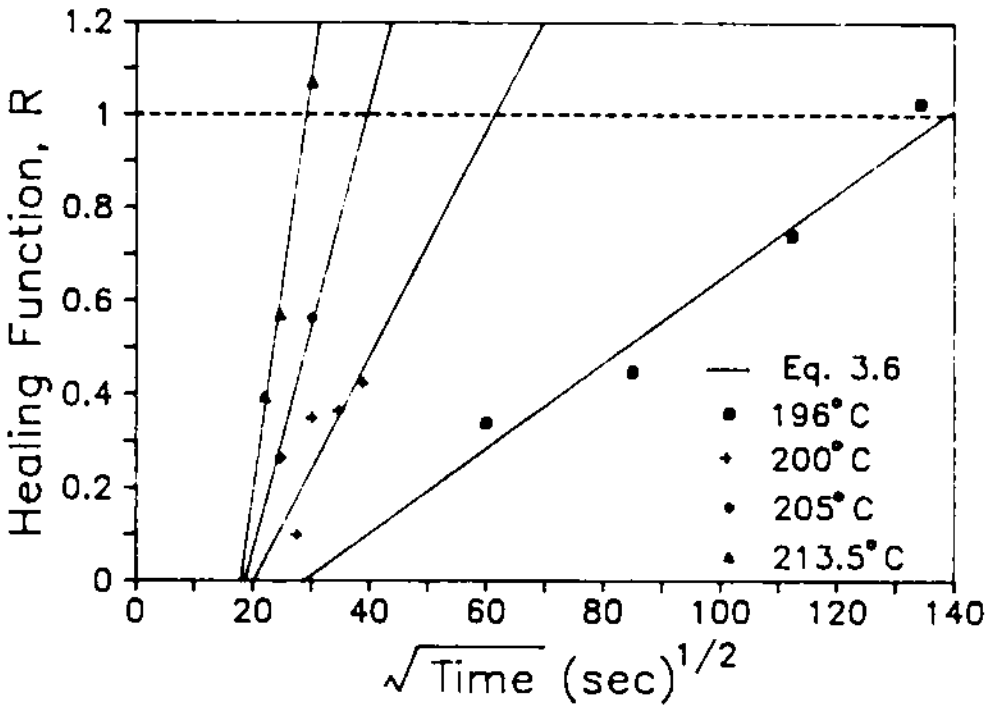

Figure 9. Healing function, R versus square root of time. Symbols represent data from reference 2. Solid lines represents the isothermal healing model solution.

measured by Howes and Loos [2]. Solid lines were calculated using Equation 3.6. As can be seen from the figure, there is good agreement between the calculated and measured healing function.

3.3 Non-isothermal Autohesion Model

A model for autohesive bond development during non-isothermal processing was developed by combining the results of the isothermal autohesion model (Equations 3.5 and 3.6) with the heat transfer analysis discussed in Section 3.1.

A numerical scheme (stepwise) was developed in which the equations for autohesive bonding (3.5 and 3.6) were solved incrementally for small time steps. A flowchart of the solution process is shown in Figure 10. At the beginning of bonding, the specimen is at initial temperature and the initial value of the healing function R at every point along the crack surface ($y = 0$, $0 \le x \le b$, Figure 5) is zero. Time is incremented by a small time step Δt and the new temperature distribution along the crack is calculated using the FEM analysis. After the temperature of the points on the crack surface reach T_g, autohesive bond development begins. At each point on the crack surface, the former and new temperature are averaged over the time step, and $C(T)$ is calculated using this temperature. The incremental healing, ΔR, corresponding to Δt at the averaged temperature is calculated and added to the previous value of R. Time is incremented and the calculations continue until the time reaches a set flag or the healing function reaches a value of unity ($R = 1$) at every point on the crack surface.

Figures 11 through 16 show a comparison between the results of the non-isothermal autohesion model calculated at the center of the CT specimen ($x = 0$, $y = 0$, Figure 5) and data. The model accurately predicts the onset of autohesive bond formation and the time required for complete autohesive bonding for temperatures close to the T_g (i.e. 196, 200, 205, and 213.5 °C) of the resin.

At elevated temperatures, the model did not match the data as well due to the fact that most of the bonding occurred non-isothermally and values for $C(T)$ were extrapolated from lower temperature data.

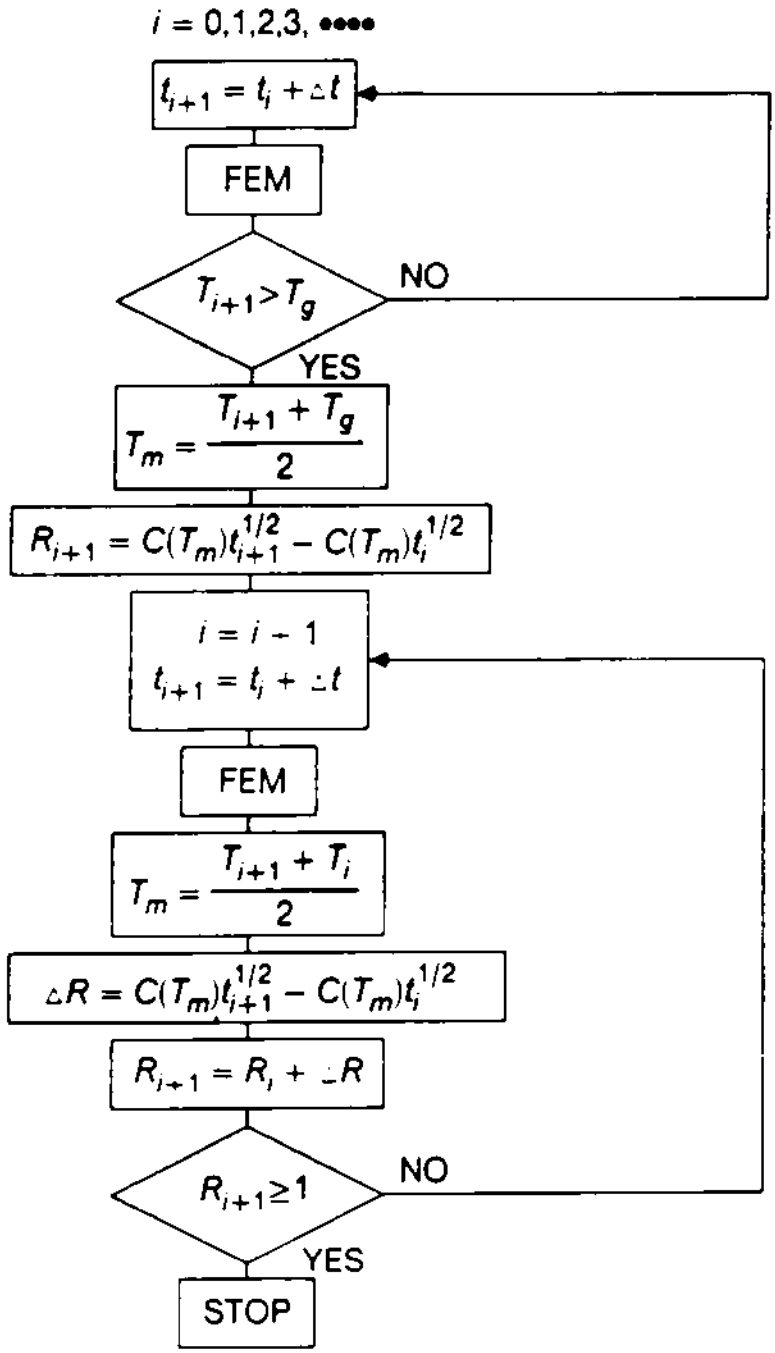

Figure 10. Flowchart of nonisothermal autohesion model.

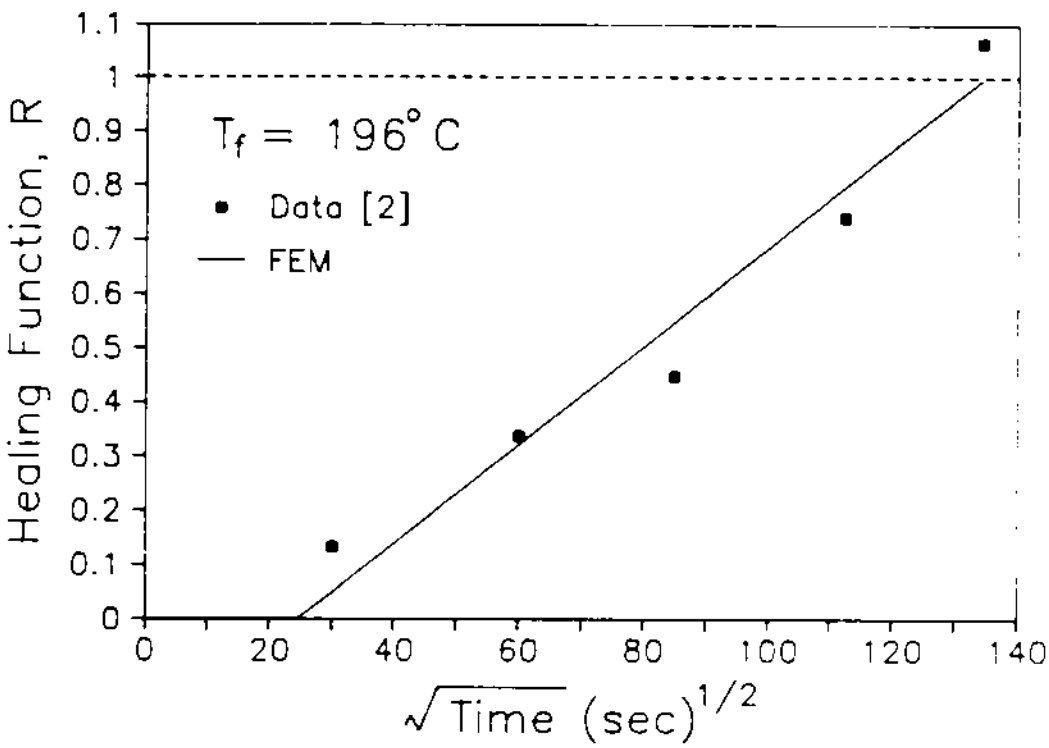

Figure 11. Healing function, R versus square root of time for polysulfone CT specimens bonded at 196°C. Comparison between data (symbols) and the nonisothermal autohesion model (solid line).

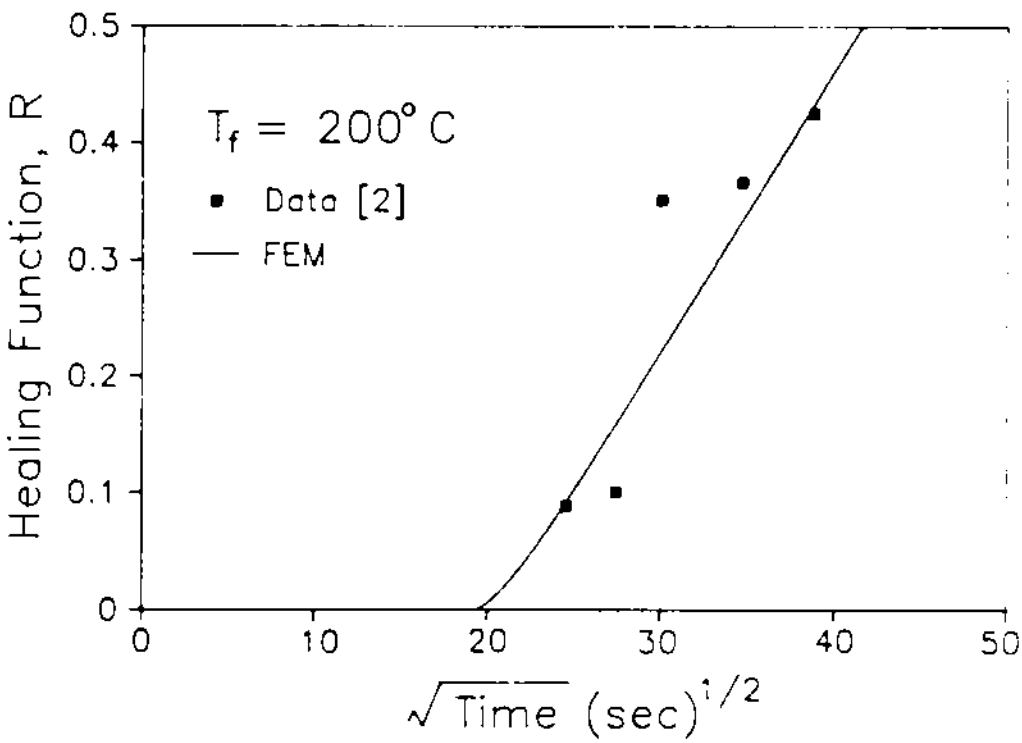

Figure 12. Healing function, R versus square root of time for polysulfone CT specimens bonded at 200°C. Comparison between data (symbols) and the nonisothermal autohesion model (solid line).

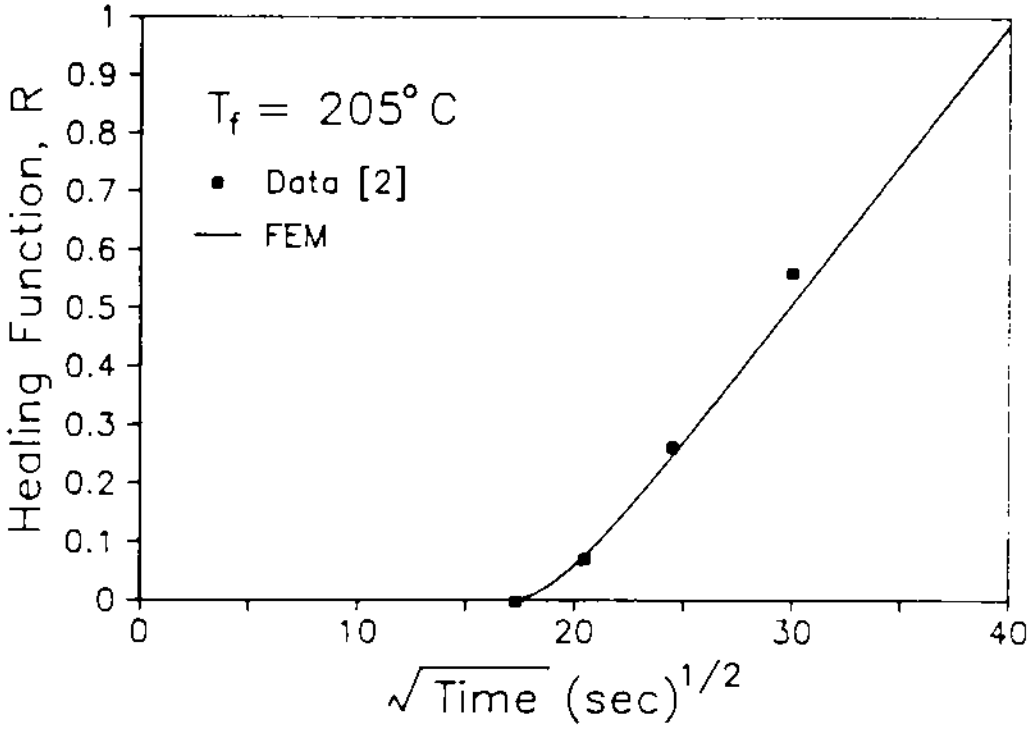

Figure 13. Healing function, R versus square root of time for polysulfone CT specimens bonded at 205°C. Comparison between data (symbols) and the nonisothermal autohesion model (solid line).

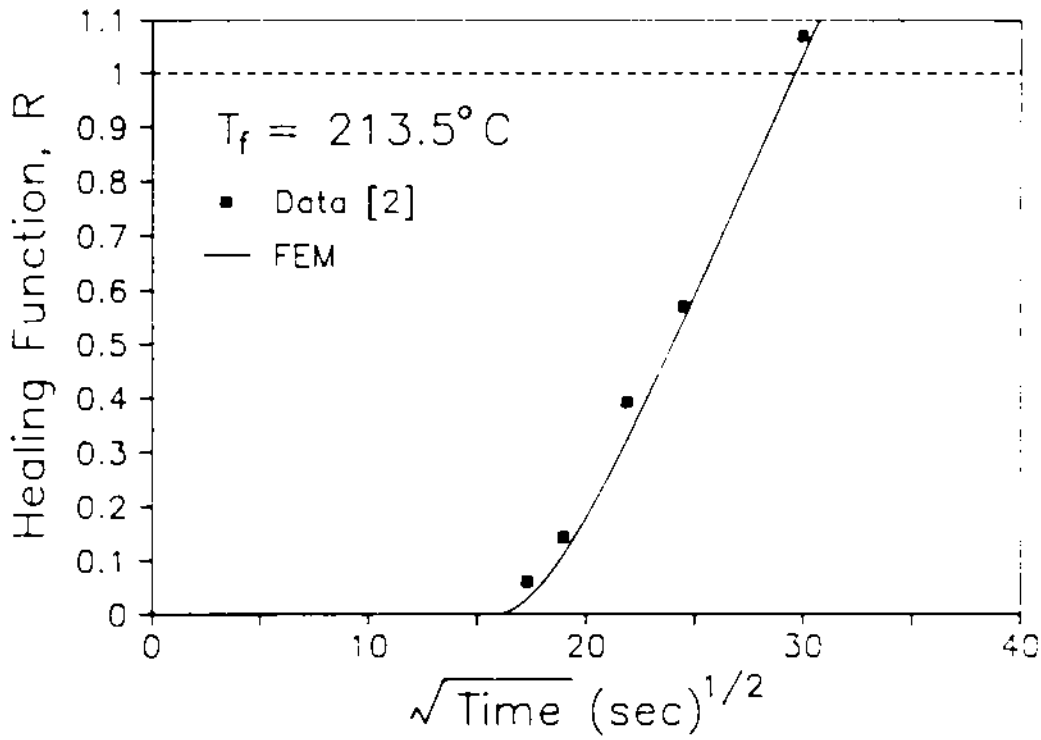

Figure 14. Healing function, R versus square root of time for polysulfone CT specimens bonded at 213.5°C. Comparison between data (symbols) and the nonisothermal autohesion model (solid line).

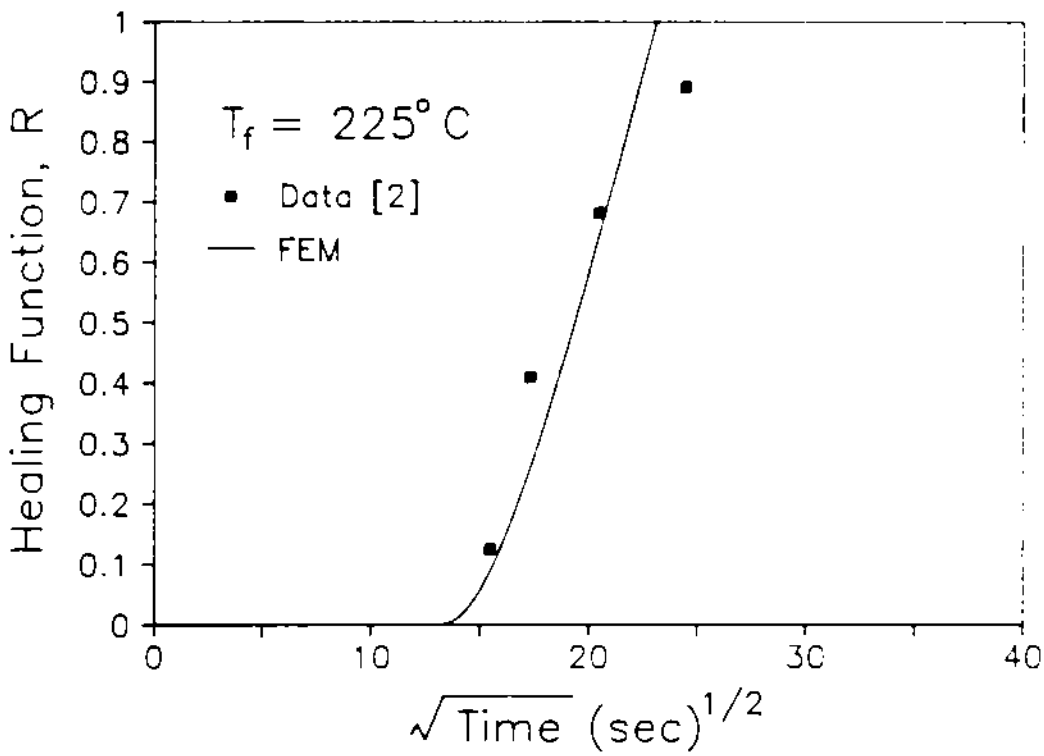

Figure 15. Healing function, R versus square root of time for polysulfone CT specimens bonded at 225°C. Comparison between data (symbols) and the nonisothermal autohesion model (solid line).

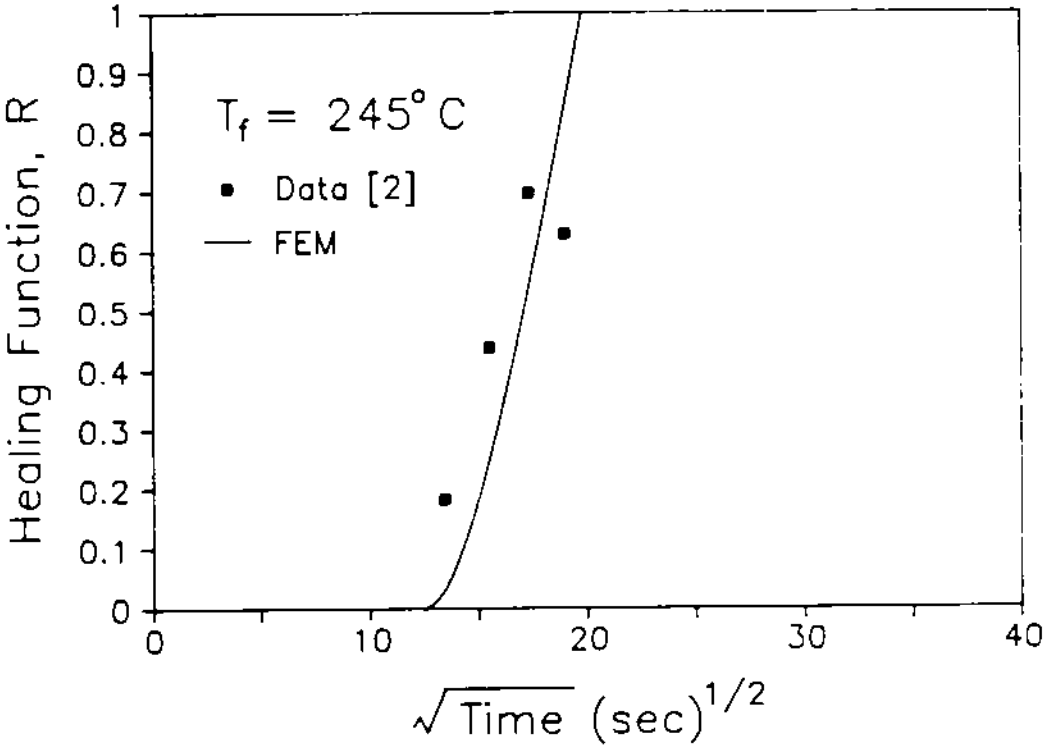

Figure 16. Healing function, R versus square root of time for polysulfone CT specimens bonded at 245°C. Comparison between data (symbols) and the nonisothermal autohesion model (solid line).

4. Double Cantilevered Beam Test and Autohesive Bonding of Thermoplastic Matrix Composites

The theories and destructive mechanical tests characterizing autohesive bond development across the interface of thermoplastic resins are well developed. However, few studies were focused on the interply strength development during formation of a fiber-reinforced thermoplastic laminate. Howes and Loos [2] used double cantilevered beam fracture test to characterize the interply strength development in AS4/P1700 composite. The data did not show a strong time and temperature dependence as observed in neat resins. The DCB fracture test has been widely applied to measure the interlaminar fracture toughness of fiber-reinforced composites. This chapter discusses the validity of the DCB test in characterizing the interply autohesive bond development in amorphous thermoplastic composites.

4.1 Literature Review

Fracture mechanics tests give an intrinsic property which can be used to characterize the material. The fracture mechanics parameters such as stress intensity factor (K), and strain energy release rate (G) are geometry independent. The double cantilevered beam (DCB) test has been extensively used to measure the interlaminar fracture toughness of composites [2,22-31].

The materials that have been investigated include both thermoset and thermoplastic matrix composites. Cross-head speeds ranging from 0.508 mm/min to 25.4 mm/min (0.20 in/min to 1 in/min) were used. Su [22] observed that the Mode I critical strain energy release rate (G_{IC}) was independent of cross-head speed. Several investigators [23,24] increased cross-head speed with increasing crack length to shorten the time needed to grow the crack at longer crack lengths. DCB specimens have been fabricated using various geometries and lay-ups. Su [22] concluded that the G_{IC} of unidirectional composites was independent of the laminate thickness.

Keary et al. [25] justified using data from multiple crack jumps on a single specimen, provided the accumulated permanent deflection was accounted for in the data reduction. They also compared the three data reduction approaches: (1) J-integral, (2) compliance calibration, and (3) an analytical equation based on linear beam bending. They found that fracture toughness measurements vary with the method of data reduction. Other investigators [24,26] observed good agreement between the three methods. The different results were believed to be due to different extents of material nonlinearity [25].

According to the observations of Keary et al. [25], the last two data reduction methods overestimate the fracture toughness. The J-integral approach is expected to be the most general and accurate of the three calculations because it does not assume any material and specimen behaviors. However, this approach is more cumbersome to use because the areas between two load versus deflection curves from consecutive crack jumps have to be measured. Fortunately, use of the last

two data reduction schemes is justified if the nonlinear behavior of the specimen is negligible, or if one approach is used throughout the whole investigation.

The contribution of fiber-bridging and fiber-breakage to the measured energy release rate were observed by several investigators [2, 23,26,27,28,29]. These two effects are due to nesting of fibers belonging to two adjacent plies. The nesting of fibers is maximized for a 0/0 interface and minimized for a 0/90 interface [23]. Also, whether fiber nesting will occur depends on the manufacturing processes [26]. If the composite is manufactured so that the fibers are generally confined to uniform layers, the fracture produces a relatively flat surface and fiber-nesting does not exist. Hence, fiber-bridging and fiber-breakage will not be observed and G_{IC}'s of different crack lengths are quite uniform throughout the specimen. On the other hand, if the fiber layers are not well-defined, fibers from various layers tends to intermingle and fiber nesting occurs. Thus it is necessary to pull fibers from one layer out of the adjacent layer in order to propagate the crack [26]. Crack propagation can occur in two ways [26]. First, the crack tip may bend around the fibers as it advances, thus losing its planarity. This complicates the crack-tip stress field and leads to an increase in the fracture surface area that is not accounted for in the calculations. Second, some of the fibers may extend at an angle across the crack opening behind the crack tip. As the crack surfaces separate, these fibers must be either pulled out of the fiber layers or broken resulting in fiber-bridging and fiber-breakage. Thus, the initial interlaminar crack will quickly become an intralaminar crack.

Fiber-bridging and fiber-breakage result in a rough fracture surface with higher values for the apparent interlaminar fracture toughness. Usually, the value of strain energy release rate increases as the crack advances from the crack initiator, due to build up of the fiber-bridging zone. The strain energy release rate reaches a steady-state value with crack growth throughout the remainder of the specimen after the fiber-bridging zone is fully developed [28]. The extra energy involved in the build up of the fiber-bridging zone is in addition to the energy absorbed in fracturing the polymer, which is assumed to be the dominant process. Therefore, the lower the matrix toughness, the greater the contributions of the fiber-bridging and fiber-breakage in increasing the apparent toughness.

It is interesting to note that among the investigators who observed fiber-bridging and fiber-breakage, Hunston et al. [26] reported the plateau values of the G_{IC}, Wilkins et al. [23] and Howes and Loos [2] reported the average values, and Hinkley et al. [28] and Martin [29] reported the values of G_{IC} measured at the first crack jump.

Martin [29] observed the existence of a resin pocket directly behind the crack initiator inserted at the mid-plane of the DCB specimens. Usually, the thicker the crack initiator the larger the resin pocket. He investigated the influence of the thickness of the crack initiator on the value of the critical strain energy release rate of the first crack jump and the delamination fatigue threshold. He found that the insert thicknesses up to 0.0762 mm (3 mil) were acceptable for the glass/epoxy composites. Inserts thicker than 0.0762 mm (3 mil) were not acceptable for determining G_{IC} and the Mode I threshold strain energy release rate, $G_{I\infty}$.

In the present investigation, the compliance method, that is an analytical equation based on linear beam bending [25], is used to determine the critical strain energy release rate from DCB tests. The assumption of linear elastic response results in the following equation for the Mode I strain energy release rate (G_I)

$$G_I = \frac{P^2}{2b}\frac{dC}{da} \tag{4.1}$$

where P is the load, b is the width of the specimen, a is the crack length and C is the compliance (i.e. $C = \Delta/P$).

For a linear elastic, isotropic cantilever beam, the load-deflection relation is

$$\delta = \frac{Pa^3}{3EI} \tag{4.2}$$

where a is the length of the beam, E is the Young's modulus and I is the moment of inertia of the beam, as shown in Figure 17. For a pair of identical cantilever beams joined at their fixed ends, the total deflection will be twice δ, that is

$$\Delta = 2\delta = \frac{2Pa^3}{3EI} \tag{4.3}$$

The compliance relation is

$$C = \frac{\Delta}{P} = \frac{2a^3}{3EI} = A_1 a^3 \tag{4.4}$$

where $A_1 = 2/3EI$ can be obtained from a curve of compliance versus a^3. Differentiating Equation 4.4 with respect to crack length (a), we obtain

$$\frac{dC}{da} = 3A_1 a^2 \tag{4.5}$$

Substituting Equation 4.5 into Equation 4.1 gives

$$G_I = \frac{3A_1 P^2 a^2}{2b} \tag{4.6}$$

Hence, the expression for critical Mode I strain energy release rate (G_{IC}) is

$$G_{IC} = \frac{3A_1 P_c^2 a^2}{2b} \tag{4.7}$$

where P_c is the critical load that causes the crack to grow corresponding to a certain crack length a.

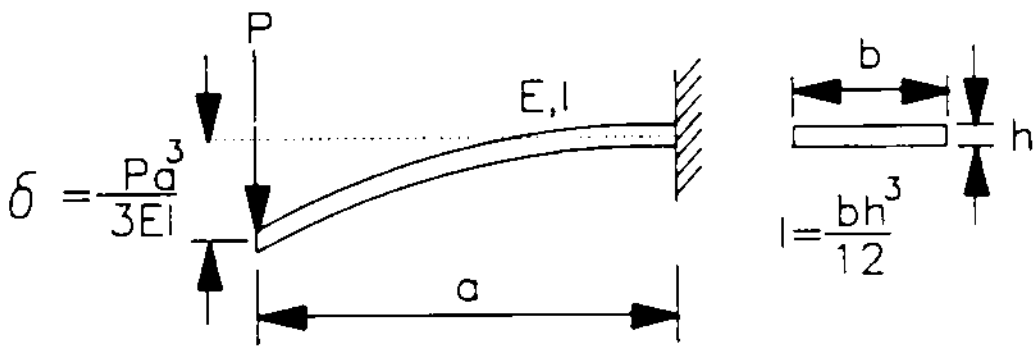

Figure 17. Load-deflection relation for an linear elastic, isotropic cantilevered beam.

4.2 Sample Preparation

Unidirectional composite laminates were fabricated from AS4/P1700 graphite-polysulfone prepreg. The prepreg was donated by NASA Langley Research Center. The laminates were 12-ply thick and were compression molded in a 152.4 mm (6 in) square steel mold. A 25.4 mm (1 in) wide by 0.0762 mm (0.003 in) thick Kapton sheet was placed at midplane along one edge of the laminate as a crack initiator. The composite fabrication procedures are outlined as follows:

4.2.1 Solvent Removal

1. Cut prepreg that had been warmed up to room temperature into 304.8 mm × 304.8 mm (12 in × 12 in) sheets.
2. Stack each sheet of prepreg between two pieces of porous teflon coated release cloth and two pieces of bleeder. The maximum number of prepregs per stack was ten.
3. Placed the stack on the tool plate of the autoclave, and sealed the stack beneath a plastic vacuum bag. The bagging assembly is shown in Figure 18.
4. Apply full vacuum and heat the assembly from room temperature to 199°*C* (390°*F*) at the rate of 0.56°*C*/ min (1°*F*/ min). After the temperature reaches 199°*C* , turned off heat source and cool down to below T_g of polysulfone (196°*C* or 381°*F*). Release vacuum and cool overnight in autoclave.
5. Remove and weigh each sheet of prepreg. Store prepreg in sealed polyethylene bags.

An average of 12.4% weight was lost from each piece of prepreg. The prepreg close to the end of the spool had a slightly higher solvent content.

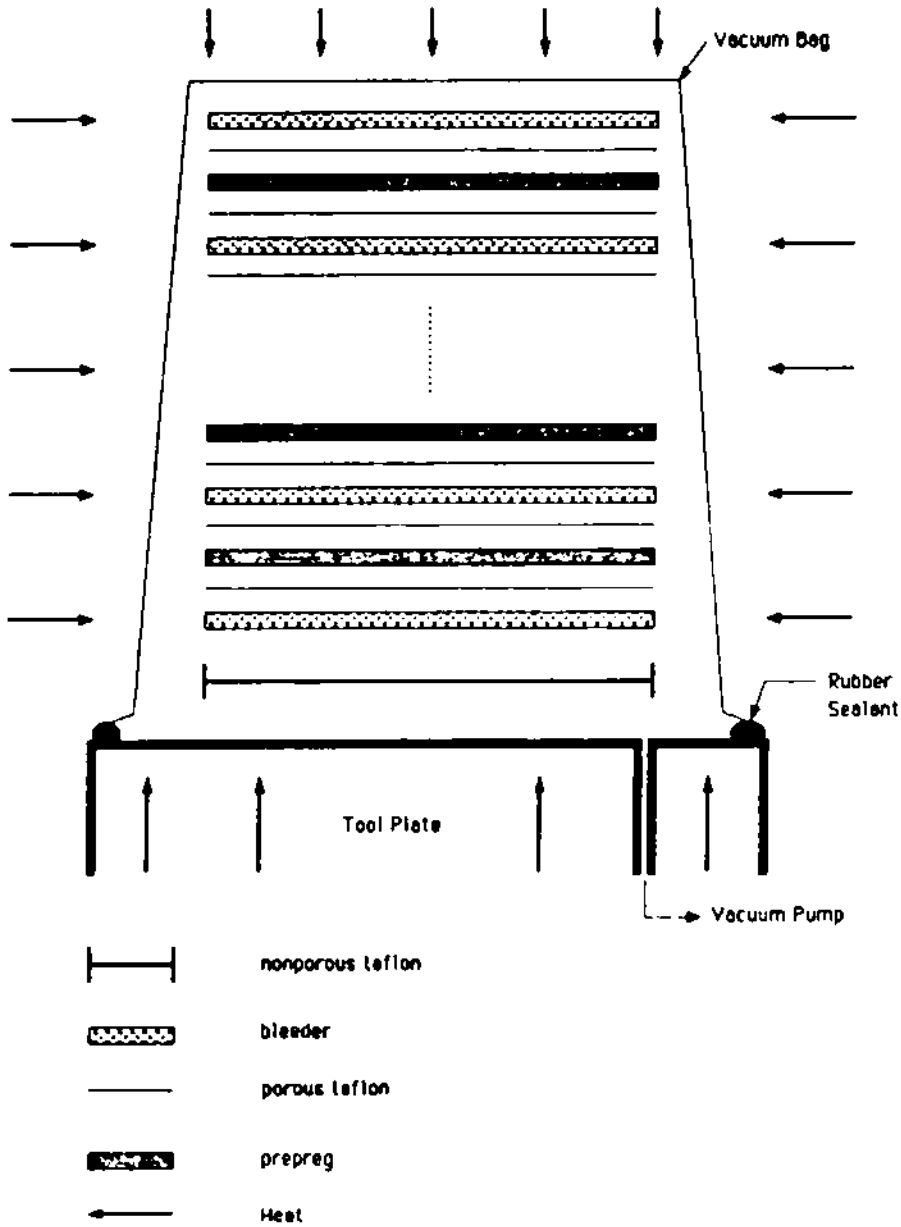

Figure 18. Solvent removal bagging assembly on the tool plate of the autoclave.

4.2.2 Laminate Consolidation

1. Cut the free solvent prepreg into 152.4 mm × 152.4 mm (6 in × 6 in) squares.
2. Stack 6 plies of prepreg in a steel mold that had been treated with Freekote 33 ® release agent. Placed a 25.4 mm × 152.4 mm (1 in × 6 in) piece of Kapton film along one end of the mold. Stack 6 more plies of prepreg over the Kapton.
3. Place a thermocouple along one edge of the prepreg plies for monitoring temperature.
4. Put the plunger on top of the prepreg carefully to prevent slippage. The assembly is shown in Figure 19.
5. Preheat the hot press to 288°*C* (550°*F*) . Place the mold in the platens of the press and apply a slight contact pressure of 48 kPa (7 psi).
6. When temperature reaches 288°*C* (550°*F*) in the mold, apply full consolidation pressure of 2068 kPa (300 psi) for 30 minutes.
7. Cool the mold below T_g of polysulfone and released pressure. The processing cycle is shown in Figure 1.

4.2.3 NDT Evaluation of the panels

The C-scan technique was used to nondestructively evaluate the integrity of the laminates. If there were any observed "intolerable" defects, the panel was reprocessed. Eighty percent of the panels were acceptable after being processed once. A typical C-scan result of a good panel is shown in Figure 20. Panels which were unacceptable after processing the first time were acceptable after being processed a second time. Figure 21 is a typical C-scan result of one of the "bad" panels before being reprocessed. Figure 22 is the C-scan result of a originally "bad" panel (Fig. 21) after being reprocessed.

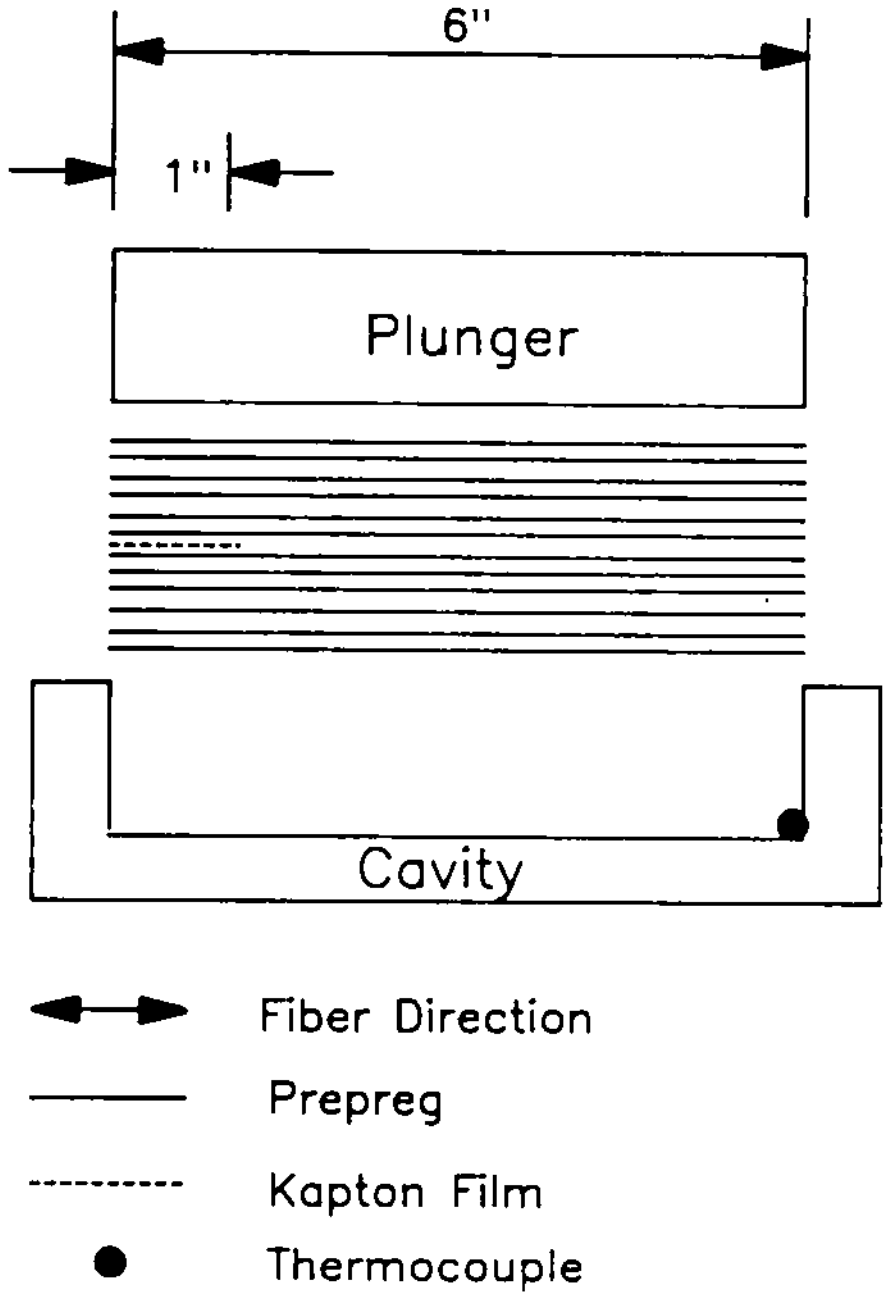

Figure 19. Matched mold laminate consolidation assembly.

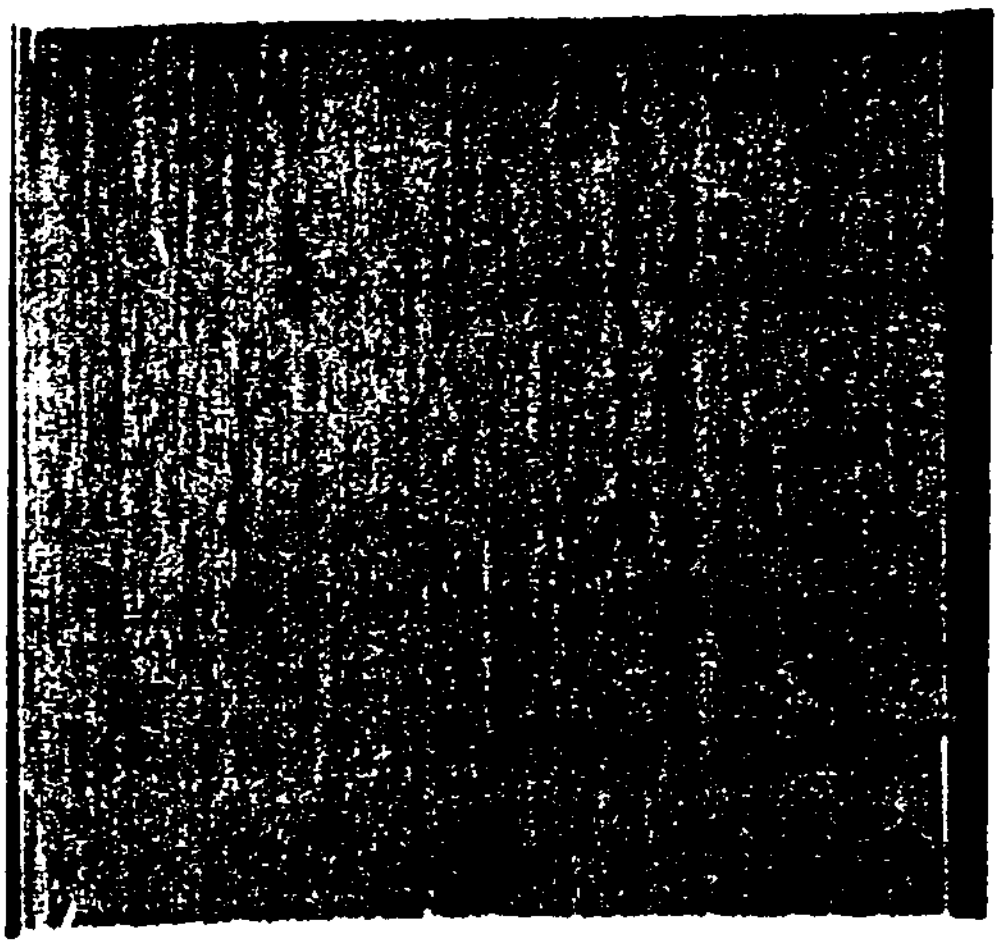

Figure 20. C-scan result of a good 152.4 mm X 152.4 mm panel.

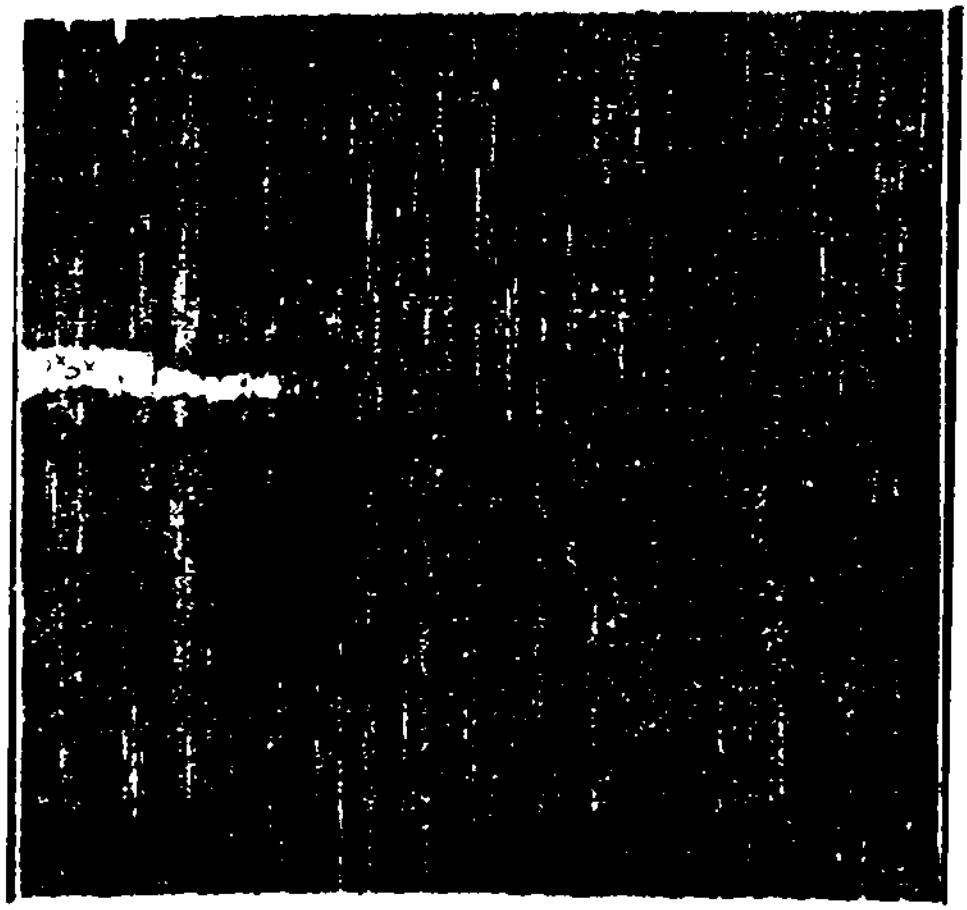

Figure 21. C-scan result of a "bad" 152.4 mm X 152.4 mm panel.

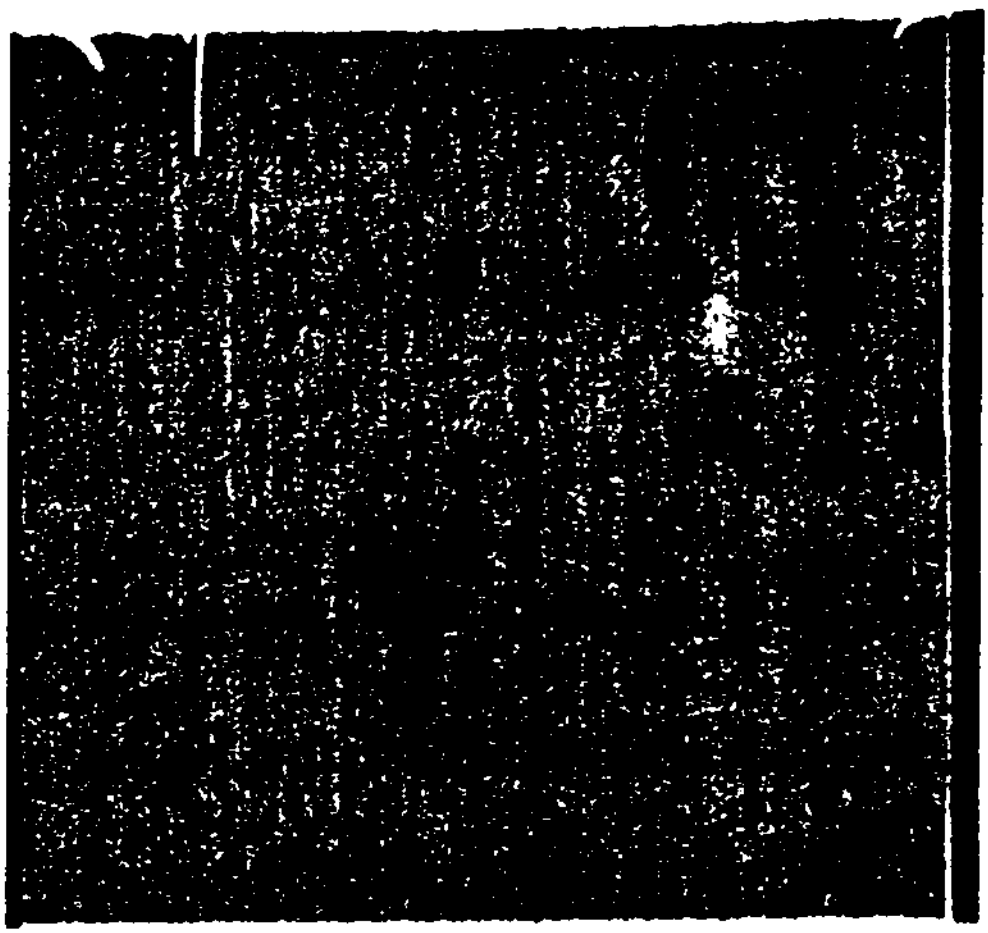

Figure 22. C-scan result of the panel shown in Figure 21 after reprocessing.

4.2.4 DCB Specimens

Six DCB specimens were cut from each panel using a water cooled diamond edged saw. The average width of the specimens was 24.2 mm (0.953 in). Aluminum tabs were bonded to the top and bottom surfaces at the edge of the specimen using an adhesive. The tabs were to used for load introduction. The tabs were aligned by balancing the beam vertically on a flat surface. A schematic diagram of the test specimen is shown in Figure 23. The sides of the DCB specimens were painted with a water based white correction fluid to help visually measure the crack length.

4.3 Testing Procedures

The characterization of Mode-I fracture toughness was carried out in an INSTRON screw driven mechanical testing machine. The DCB specimens were fractured at a crosshead speed of 2.54 mm/min (0.1 in/min). A curve of load versus crosshead displacement was recorded for each crack jump. A crack was allowed to propagate 6 mm to 9 mm before the displacement was halted. Then, one minute was allowed for the crack to self-arrest. Both audible and visual clues made crack advancement apparent. The new crack tip was marked on both edges of the specimen and the machine was returned to zero load before reloading. This procedure was repeated for 4 to 6 times for each specimen until the specimen no longer behaved geometrically linear. At this point, the crack was allowed to propagate to within approximately 25.4 mm (1 in) from the end of the specimen at the same crosshead speed. However, no additional data was taken. A typical output from the chart recorder is shown in Figure 24.

In order to avoid nonlinear (large) deflections, the crosshead displacement was controlled by the inequality as shown below:

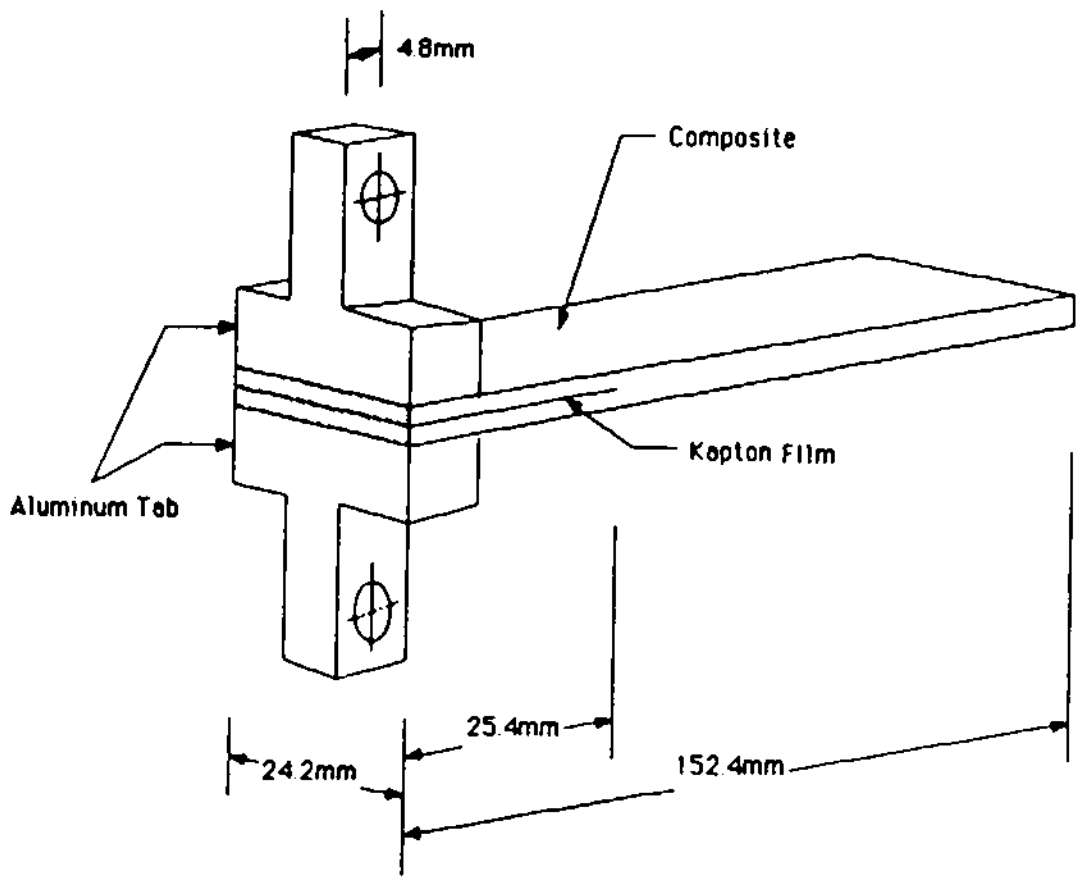

Figure 23. Schematic diagram of the DCB specimen.

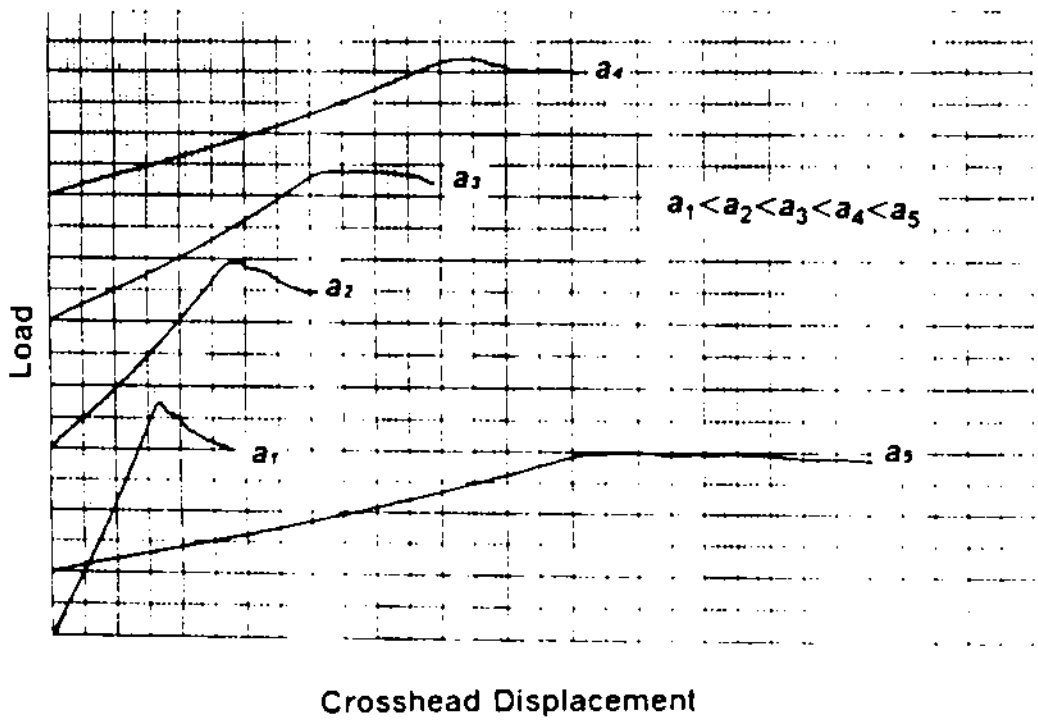

Figure 24. Typical chart recorder output from DCB test for one specimen.

$$\Delta < 0.4a \tag{4.8}$$

This condition falls within the linear (small) deflection beam bending range predicted by analysis [30]. Keary et al. [25] and Hinkley et al. [28] also used this inequality in their work. Therefore, calculation of G_{IC} were justified from the viewpoint of a linear specimen test analysis. Any non-linear P versus Δ response was expected to involve other factors (e.g. nonlinear material).

4.4 Healing Procedures

The fractured DCB specimens were placed in a special alignment fixture and healed for a predetermined time at an elevated temperature and pressure in a Tetrahedron hot press. The healing assembly is shown in Figure 25. In order to apply pressure evenly on the specimen, the fixture was carefully placed at the center of the platens. An initial contact pressure of 137 kPa (20 psi) was used and the heating cycle was the same as shown in Figure 1. After processing the specimens were cooled at a rate of 1.4°C (or 2.5°F) per minute. The test matrix is shown in Table 2.

All the healed specimens were C-scanned before being subjected to DCB tests. The DCB tests and Mode I critical strain energy release rate calculations were performed using the procedures described in Section 4.3.

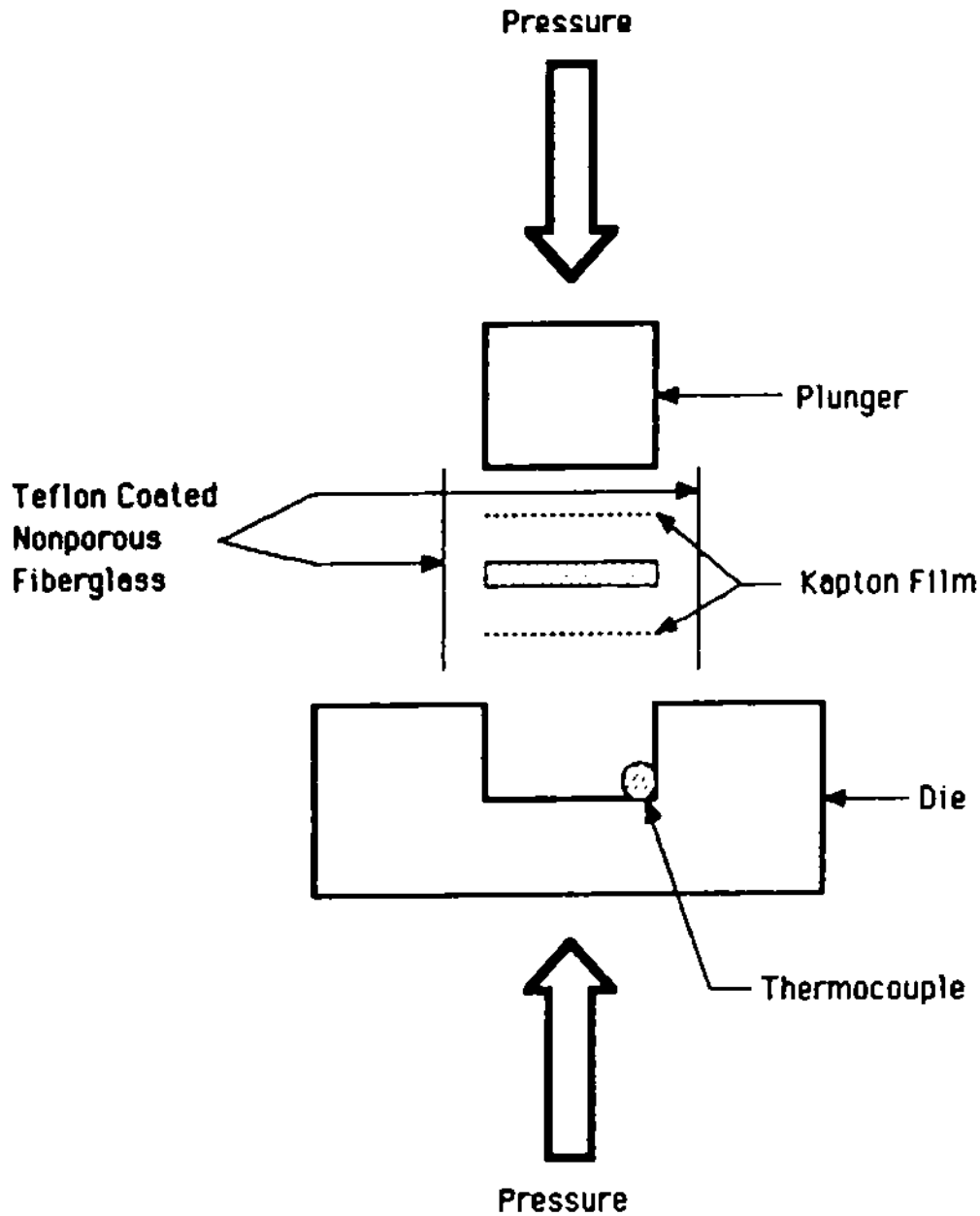

Figure 25. Healing assembly of the DCB specimen.

Table 2. Test matrix of DCB healing experiments.

Data Set	Temperature (°C)	Pressure kPa/psi	Time (min)
1	245	690/100	30
2	245	1379/200	30
3	245	2068/300	30
4	245	690/100	60
5	245	6895/1000	60
6	288	2068/300	30
7	343	2068/300	30

4.5 Results

4.5.1 Double Cantilevered Beam Test

Fiber-bridging and breakage were observed in both the virgin and the healed DCB specimens. The plateau G_{IC} was 30% to 170% higher than the G_{IC} of the first load application for the virgin specimens and 2% to 80% higher than the G_{IC} of the first load application for the healed specimens. It is not surprising that the contributions of fiber-bridging and breakage to G_{IC} is much smaller for the healed specimens. The thickness of the Kapton insert was below the 0.0762 mm (3 mil) limit suggested by Martin [29]. The more conservative G_{IC} measurement of the first crack jump was reported because it most likely represents the G_{IC} value of fracturing the matrix.

The average G_{IC} value of the first crack jump was 567.36 J/m^2 for the undamaged specimens. The standard deviation from the mean was 49.61 J/m^2. This G_{IC} is similar to the G_{IC} measurements reported by Howes and Loos [2] for 12-ply graphite/polysulfone composites using a smaller 12.7 mm × 76.2 mm (0.5 in × 3 in) specimen. The measured G_{IC} was higher than pure epoxy matrix

composites but was lower than many thermoplastic and some toughened epoxy matrix composites [22,24,25,26,28,29,31]. Attention should be given to the method used (average, initial, or plateau) in reporting G_{IC} measurements in the literature.

Following the same non-dimensional scheme used for the CT specimens, the healing function is defined as

$$R = \frac{G_{IC}}{G_{IC\infty}} \tag{4.9}$$

where G_{IC_∞} is the initial critical strain energy release rate for the undamaged specimens. Two specimens were tested in data set 5 and three specimens were tested for the each of the remaining data sets (see Table 2). Average values for R and the standard deviation from the mean were calculated. The results of the DCB tests on the healed composite specimens are shown in Figures 26-28. The symbols represents the mean of 3 measurements at each condition, and the error bars represent ± 1 standard deviation from the mean. The effects of pressure on the healing process is shown in Figure 26. In Figure 26(a), the healing function increases from 0.71 at 690 kPa (100 psi) to a plateau of about 0.9 at 2068 kPa (300 psi). Although only two data points were obtained at 6895 kPa (1000 psi) in Figure 26(b), we can still see the trend of increasing R with increasing healing pressure. A 10 fold pressure increase resulted in only 12.5% increase in the healing function.

Figure 27 shows that the healing process is time dependent. It is not surprising since autohesive bond development is a time dependent process.

For the last healing parameter in Table 2, the viscosity of polysulfone at such a high temperature was very low (approximately two orders of magnitude lower than the value at 245°C [4]). Tremendous amounts of fiber and resin were squeezed out at the free edge where the Kapton sheet

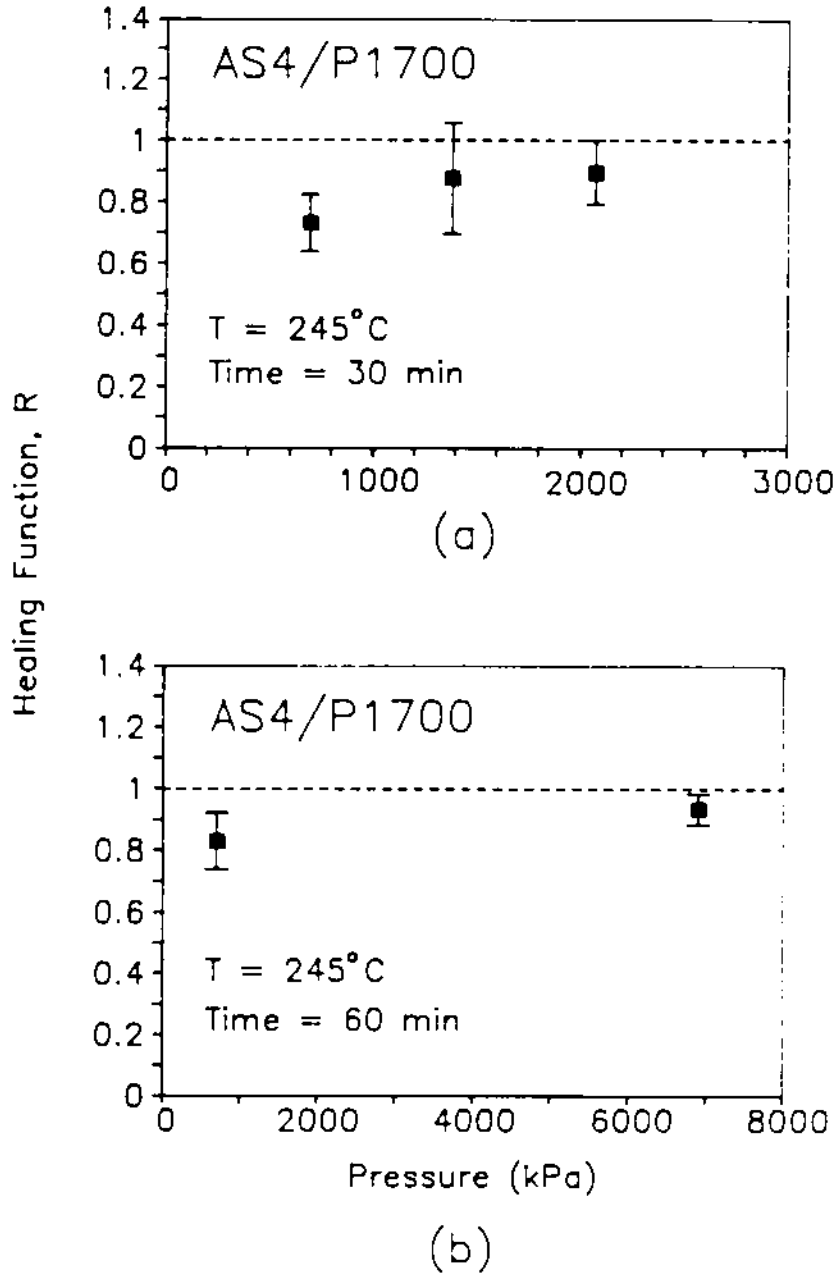

Figure 26. Healing function versus pressure for AS4/P1700 unidirectional composites bonded at 245°C for (a)30 minutes and (b)60 minutes.

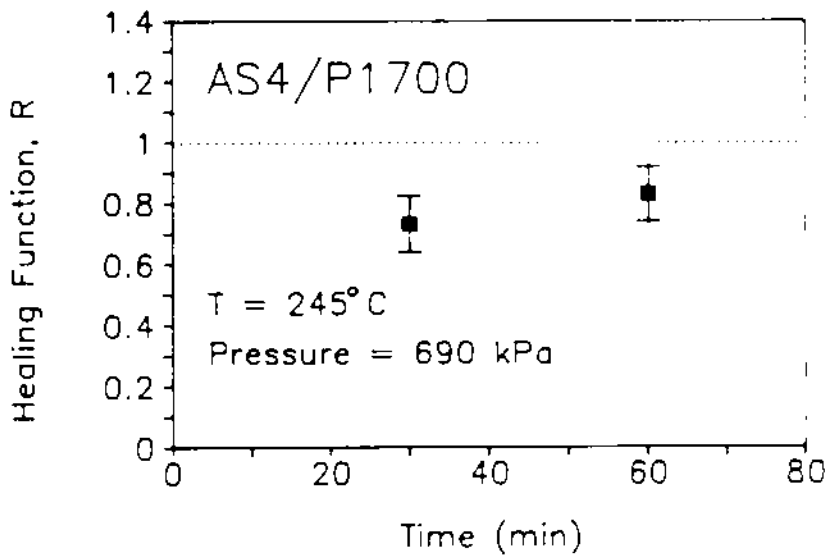

Figure 27. Healing function versus time for AS4/P1700 unidirectional composites bonded at 245°C and 690 kPa (100 psi).

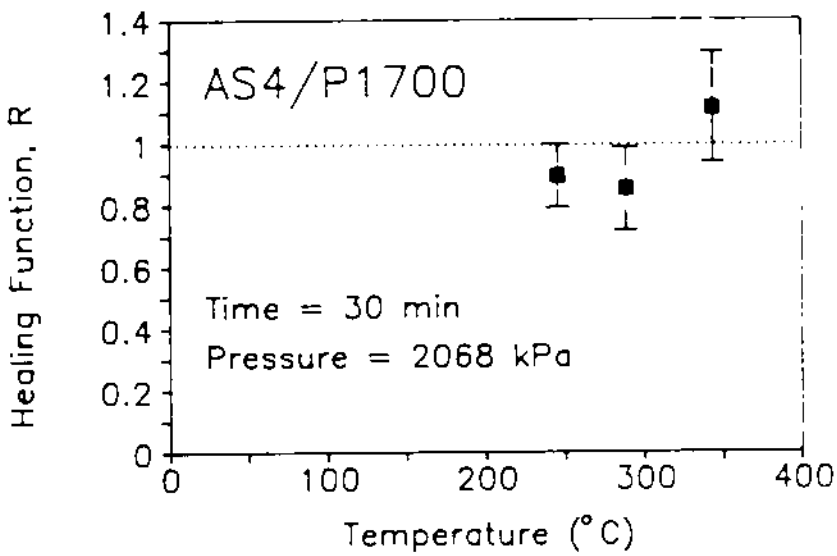

Figure 28. Healing function versus temperature for AS4/P1700 unidirectional composites bonded at 2068 kPa (300 psi) and 30 minutes.

was inserted. The healed specimens were tested, but the measured G_{IC} was much greater than the G_{IC} of the undamaged specimen.

The large amount of fiber/resin that was squeezed out during healing made the data point at 343°C in Figure 28 unreliable. The healing function R at 245°C has obtained 90% of original fracture energy. Judging from the fact that the healing function at 288°C is less than that at 245°C, it is believed that R has already reached a plateau.

4.5.2 Ultrasonic C-Scan

The healed specimens were C-scanned before being subjected to the DCB test. The C-scan technique qualitatively evaluated the degree to which the fractured surface had healed. It was found that the results of DCB tests correlated with the C-scan measurements. Figure 29 shows the C-scan results of typical specimens for the seven sets of healing parameters. The white areas correspond to poor-qualitative bonding. Figures (a)-(c) and Figures (d)-(e) show that higher pressures improve the degree of intimate contact and the amount of interply bonding. Figures (a) and (d) clearly show the role of time in the healing process. Figures (e)-(g) show that full intimate contact of the fractured surfaces has been obtained resulting in complete autohesive bonding of the surfaces.

4.5.3 Microscopy of the Cross-Sections of the Undamaged and Healed Specimens

The cross-sections of one undamaged specimen and selected healed specimens were polished and examined under an optical microscope. Figure 30(a) shows the cross-section of an undamaged specimen. We can see that fiber layers are not well defined and fiber nesting is obvious. Thus, it is not surprising to find that both intralaminar and interlaminar cracks exist at the cross-sections

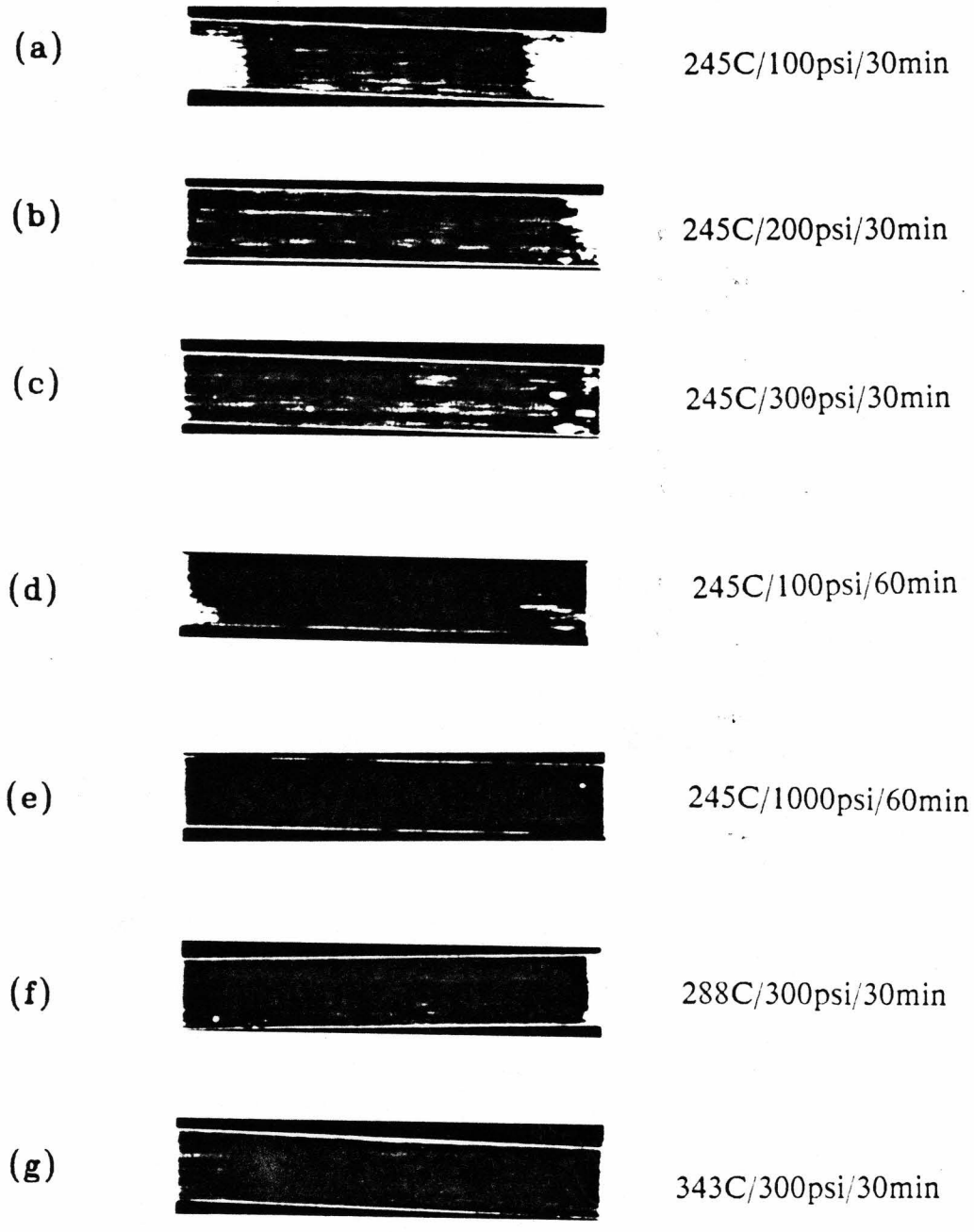

Figure 29. Ultrasonic C-scan results of typical AS4/P1700 unidirectional DCB specimens bonded at different set of parameters. Kapton inserts are at the left ends of the specimens.

of the healed specimens examined, i.e. Figure 30(b). The nonuniform tow height of prepreg is also quite obvious from Figures 30(a) and (b).

In examining the cross-sections of the healed specimens, we found that the fracture surfaces are not flat and there was excess resin flow occurring at the fracture surface during healing, as shown in Figure 30(b). Due to fiber-breakage, the broken fibers sometimes did not realign along the original fiber direction. Thus, some oval shaped fiber cross-sections were observed at the healed interface, as seen in Figure 31(a) and (b). An interesting phenomenon was observed when examining the cross-section of the specimen healed at 245°C, 6895kPa(1000psi), 60min (Figure 31(a)). There are several fibers in the central region of the picture that have been debonded from the matrix. The fiber/matrix interfaces to the right and the left of the debonded fibers are either good or just about to debond. It is probably because that the crack front is zigzagged and not a smooth curve. Some fractured fibers are also observed in Figure 31(a). Due to the existence of oval shaped fibers and excess resin flow, there is another debonded interface next to the main fracture interface, as shown in Figure 31(b). This is believed to be due to the large cross-head displacement at larger crack lengths.

4.5.4 Scanning Electron Microscopy

The fracture surface of a undamaged specimen and the healed specimens were examined under the scanning electron microscope. Figure 32 shows the fracture surface of an undamaged specimen. A resin pocket right behind the Kapton insert was observed. This was the only resin rich area along the fracture surface observed by SEM. Extensive resin deformation was observed at the resin pocket. Scattered fiber-breakage was also observed. A closer look at the fracture surface away from the Kapton insert shows interfacial failure and extensive matrix deformation where cohesive failure occurred (Figure 32(b)). It is believed that the mixed failure mode was the cause of the high value of the standard deviation of the G_{IC} measurement of the undamaged specimens.

(a)

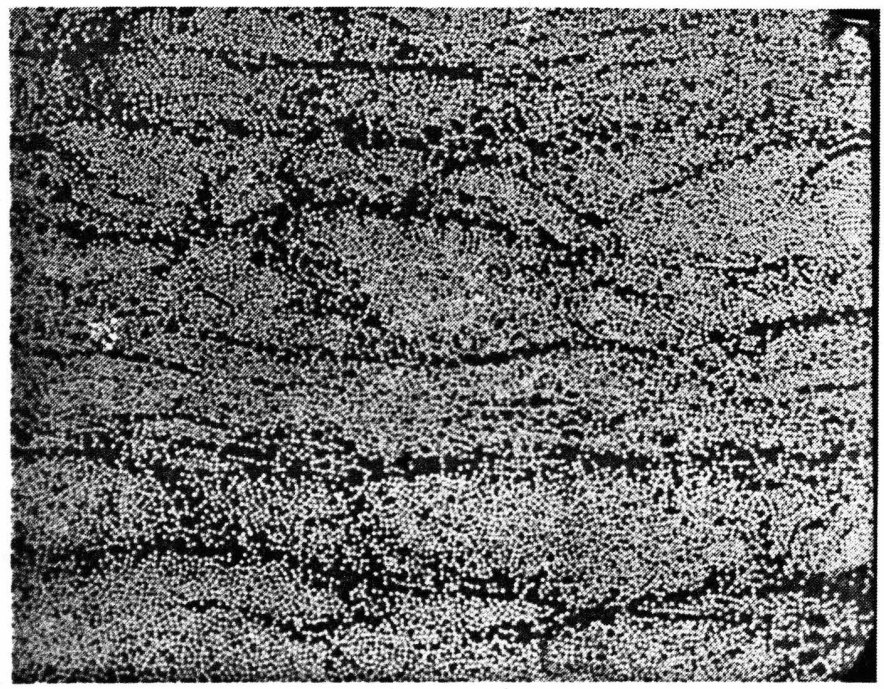

(b)

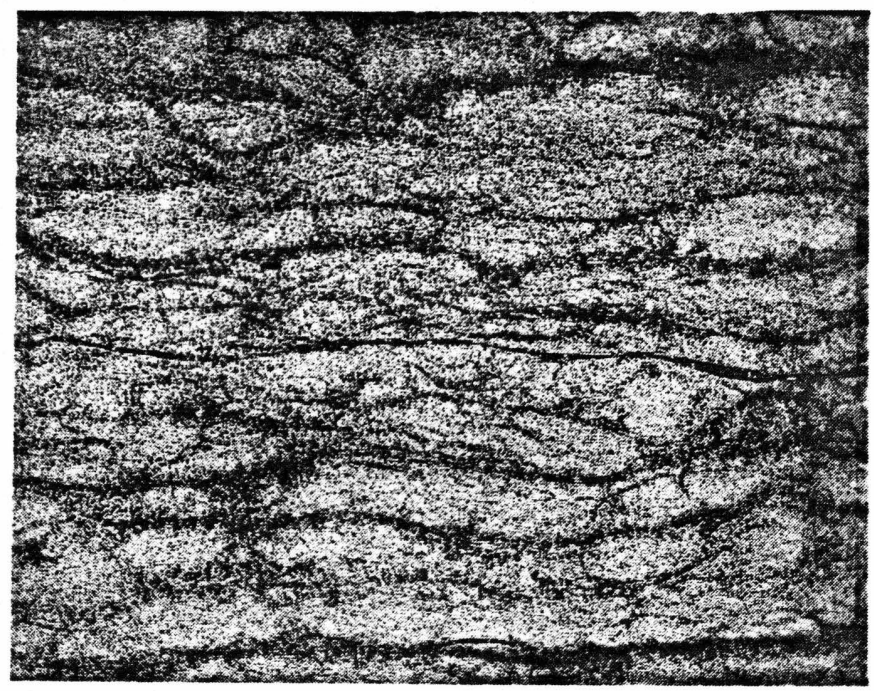

Figure 30. Cross-sections of (a)undamaged specimen at 100X, (b)specimen healed at 245°C/690kPa(100psi)/60min at 50X.

(a)

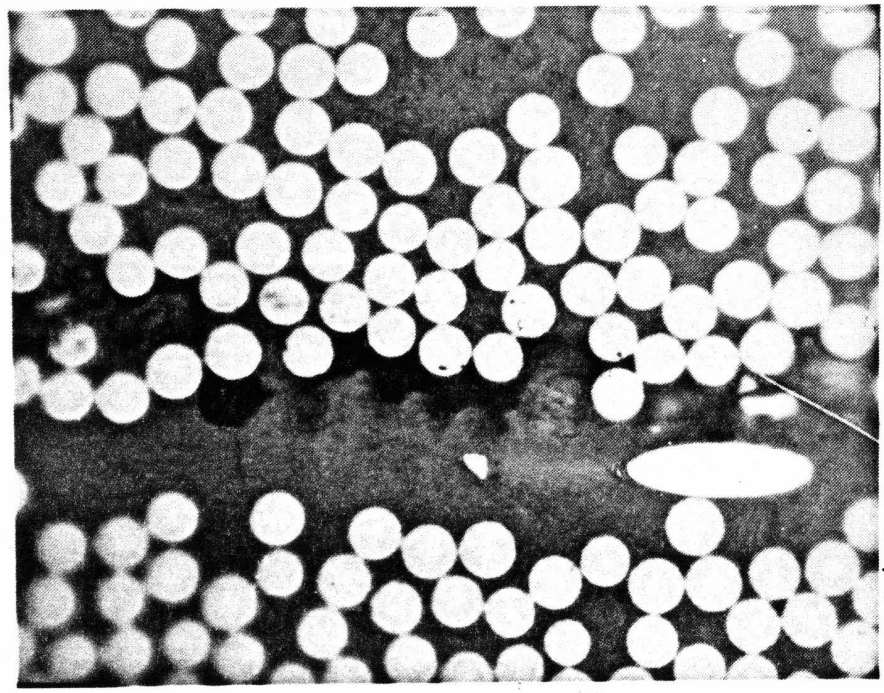

(b)

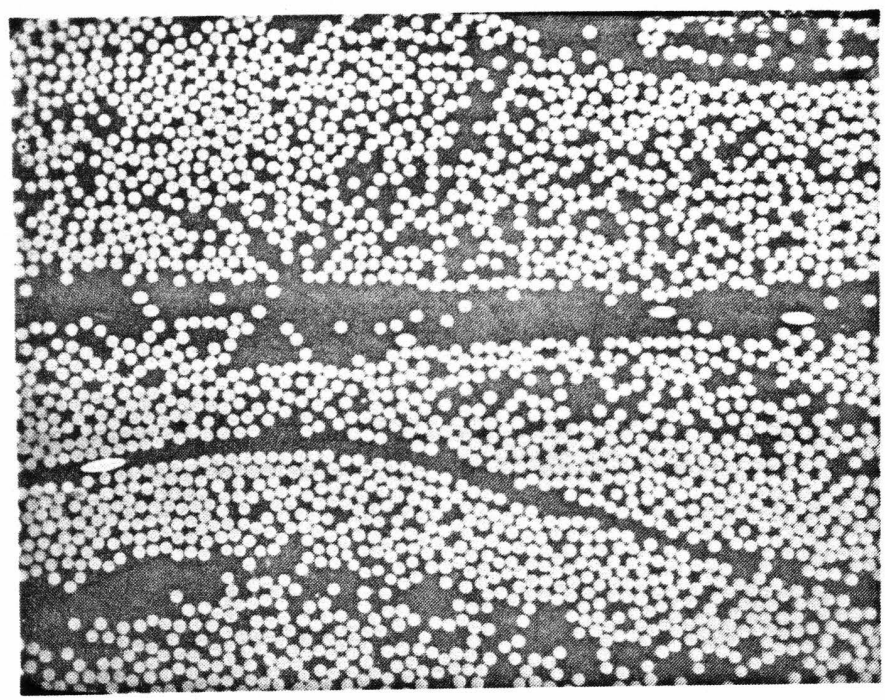

Figure 31. Cross-sections of specimens healed at (a)245°C/6895kPa(1000psi)/60min at 1000X, (b)288°C/2068kPa(300psi)/30min at 250X.

Some interesting phenomena were observed when examining the fracture surfaces of the healed specimens. Thicker resin rich areas due to excess resin flow existed across the entire fracture surface. This phenomenon was also supported by the optical microscopic results. Figures 33(a) and (b) are the fracture surfaces of specimens healed at 288°C/2068kPa(300psi)/30min and 245°C/2068kPa(300psi)/30min, respectively. In Figure 33(b) the Kapton insert is at the right edge of the figure. It is likely that the "missing" resin-rich area behind the Kapton insert was on the opposite fracture surface, similar to Figure 33(a). Extensive matrix deformation was observed in the specimen shown in Figure 34(a). But the fiber surfaces are very clean similar to what was observed in the undamaged specimen. Figures 34(b) and 35 show that loose strings of polymer have peeled off across the fracture surface with extensive matrix deformations. Polymer tendrils were observed quite often on the fracture surface of the healed specimens.

Microscopic examination of the cross-sections and fracture surfaces show that the fracture mechanisms are quite complex for the healed DCB specimens. This is probably why there was considerable scatter in the healing data. The poor fiber-matrix interfacial strength causes the low G_{IC} values of the undamaged and healed specimens.

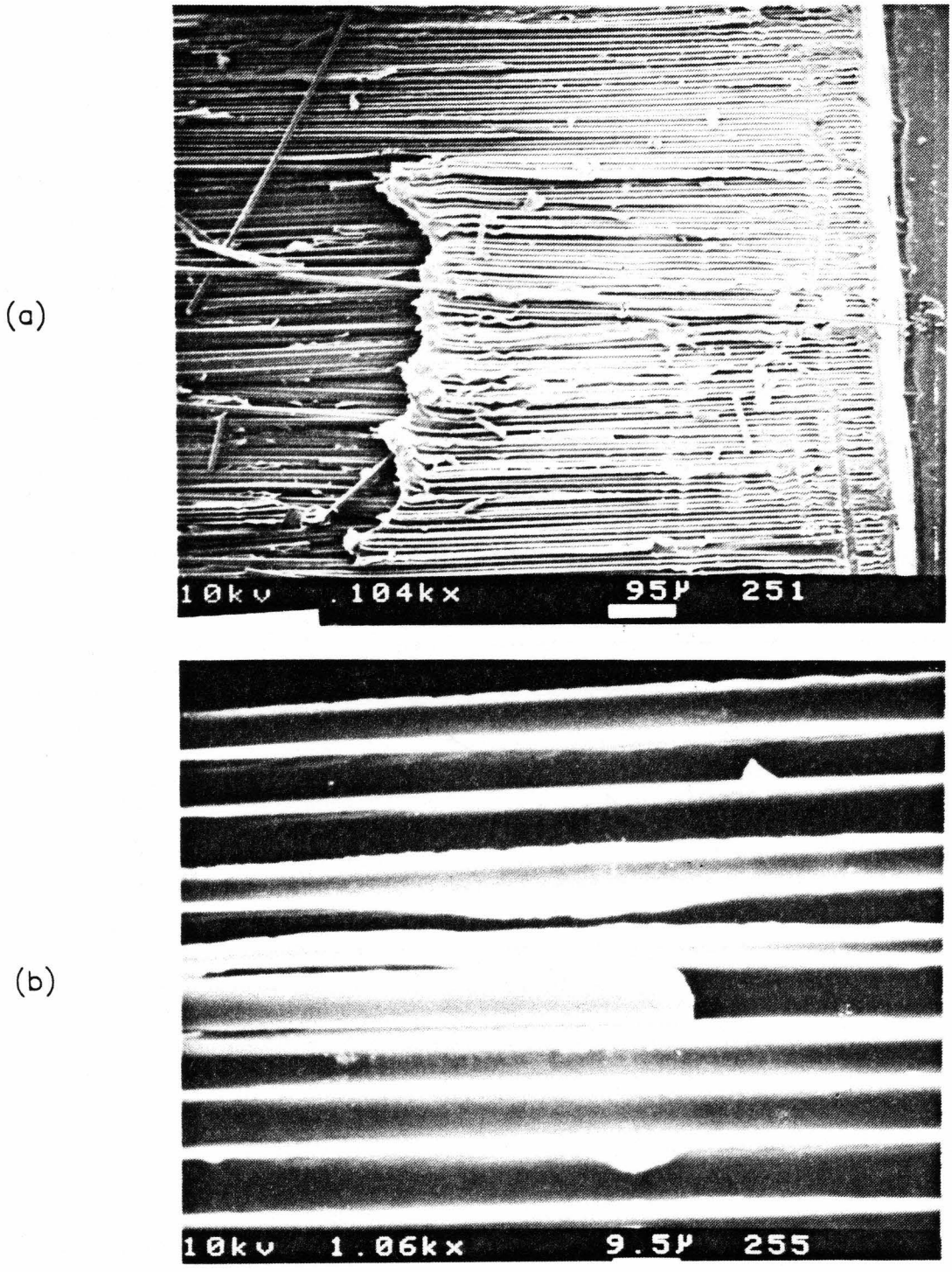

Figure 32. Fracture surface of undamaged specimen.

(a)

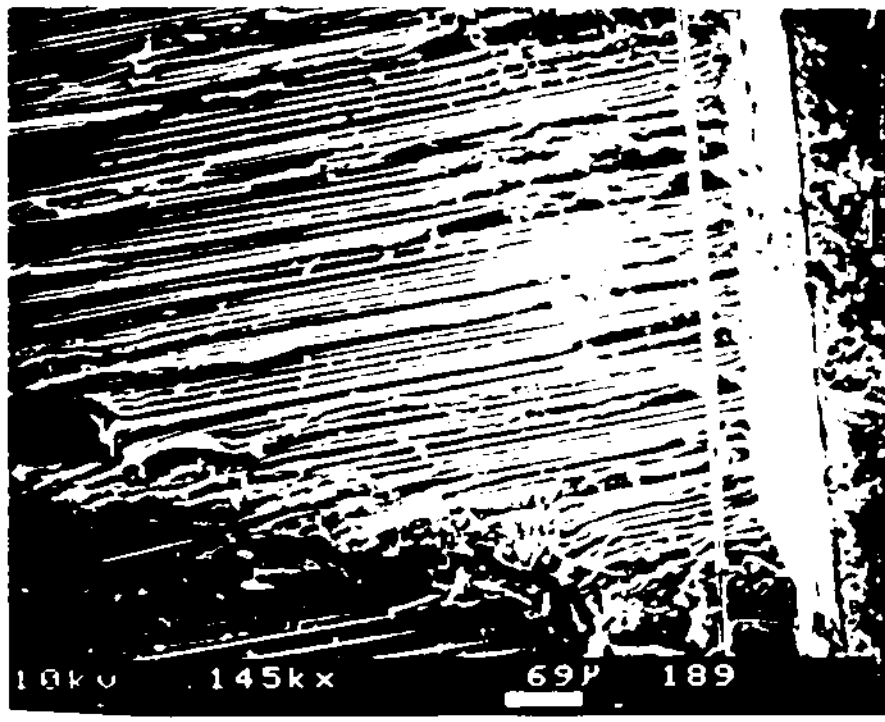

(b)

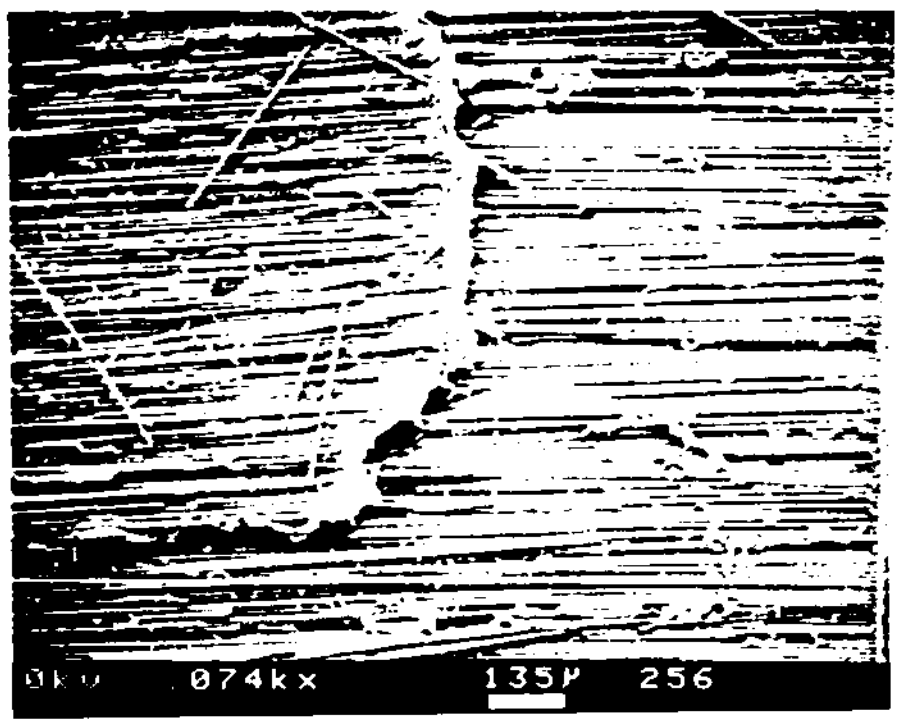

Figure 33. Fracture surface of specimens healed at (a)288°C/2068kPa(300psi)/30min, (b)245°C/2068kPa(300psi)/30min.

(a)

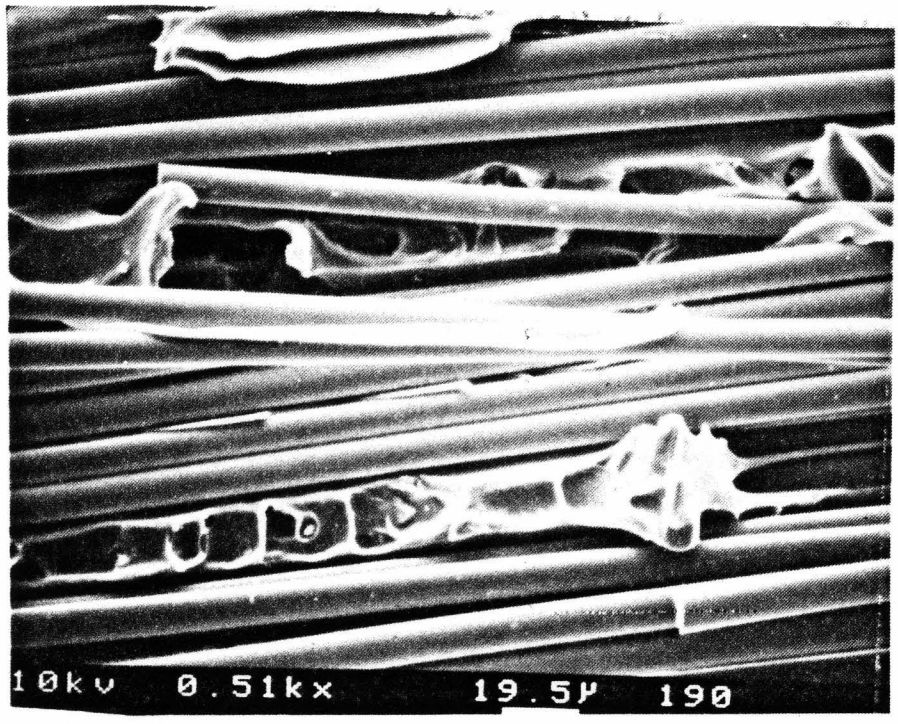

(b)

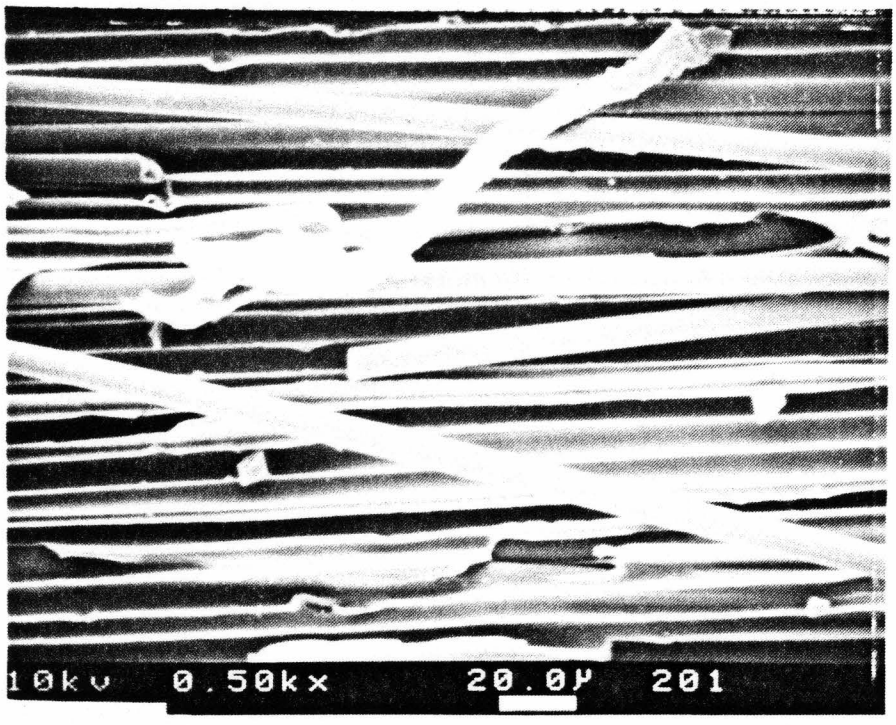

Figure 34. Fracture surface of specimens healed at (a)288°C/2068kPa(300psi)/30min, (b)245°C/690kPa(100psi)/60min.

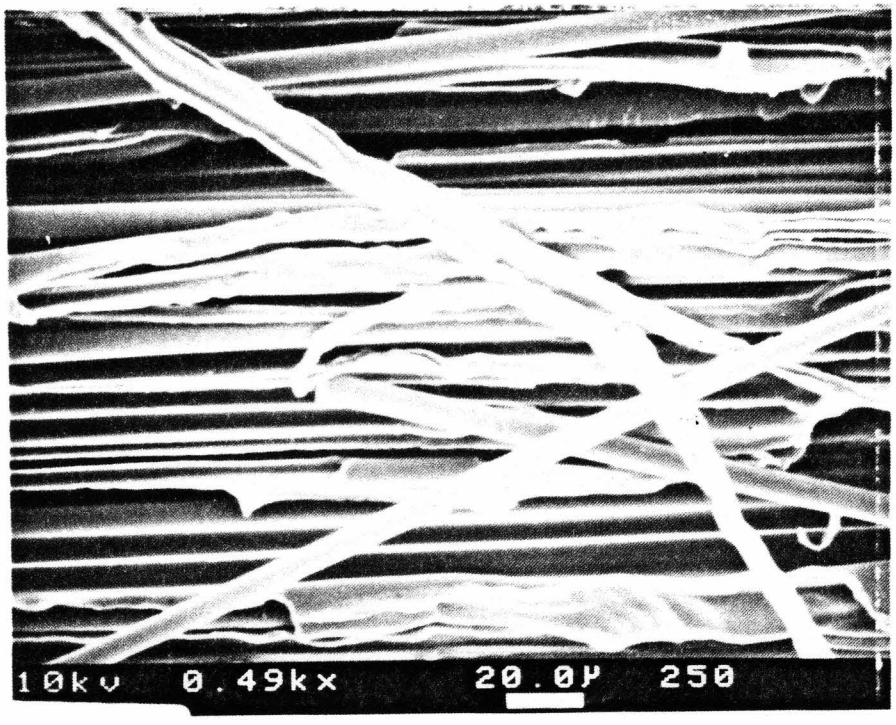

Figure 35. Fracture surface of specimens healed at 343°C/2068kPa(300psi)/30min.

5. Non-Isothermal Autohesion Model for Amorphous Thermoplastic Composites

In processing of thermoplastic matrix composites, it has been observed that individual prepreg plies consolidate into a laminate by bonding themselves to one another at the interfaces. The interply bond strength for thermoplastic matrix composites has been shown to be dependent upon the processing parameters, pressure, temperature, and contact time. If, during processing, the temperature distribution in the composite is nonuniform, the ply interfaces will bond (or heal) at different rates. Thus, for a specified processing cycle, it is important to know precisely the temperature and degree of autohesive bonding at every point in the composite laminate in order to estimate the required process time.

In this chapter, a model for non-isothermal processing of amorphous thermoplastic composites is presented. The model is an extension of the non-isothermal autohesion model developed for an amorphous thermoplastic resin in Chapter 3. Results of the model are compared with temperature data obtained from a 64-ply unidirectional composite.

5.1 Heat Transfer Analysis of Thermoplastic Composite Material

Consider a thermoplastic composite laminate consolidated from unidirectional prepreg. The composite is fabricated by cutting the prepreg to the desired dimensions and then stacking the prepreg sheets in the cavity (bottom portion) of a metal mold (similar to what is shown in Figure 19). The plunger (top portion) of the mold is placed on top of the prepreg and the entire assembly is placed between the platens of the hot press. When the platens are heated, heat is conducted through the mold and into the composite. The vertical surfaces around the mold are exposed to the ambient. Heat is lost from these surfaces by free convection. A typical processing cycle was shown in Figure 1.

As discussed in Chapter 1, at some point during processing, a consolidation pressure is applied to allow for coalescence and intimate contact of the ply interfaces. In this initial analysis, it is assumed that the ply interfaces achieve complete intimate contact instantaneously. Hence, the effects of consolidation pressure are neglected.

The problem to be analyzed is the composite and mold assembly shown in Figure 36. The temperature distribution in the composite laminate during processing can be determined from the unsteady heat conduction equation. For a unidirectional composite the transient heat conduction equation can be written as follows:

$$\rho_c C_{pc} \frac{\partial T}{\partial t} = \frac{\partial}{\partial x}\left(k_x \frac{\partial T}{\partial x}\right) + \frac{\partial}{\partial y}\left(k_y \frac{\partial T}{\partial y}\right) + \frac{\partial}{\partial z}\left(k_z \frac{\partial T}{\partial z}\right) \tag{5.1}$$

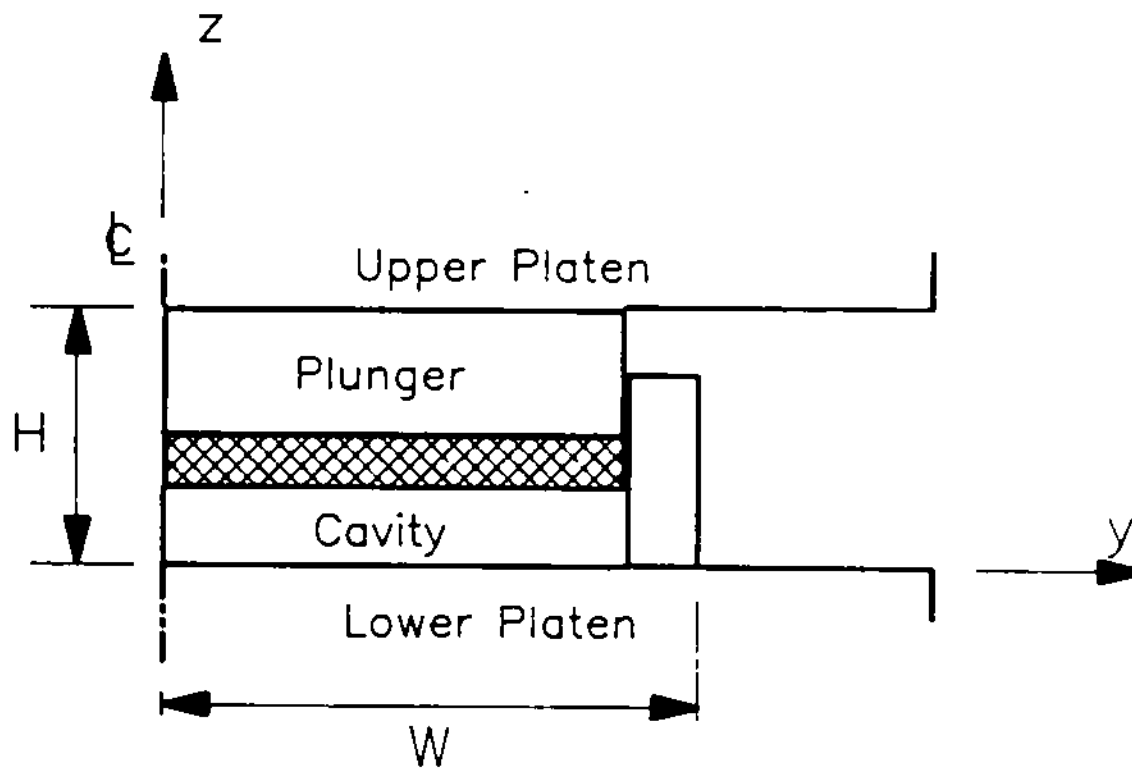

Figure 36. Coordinate system used in the heat transfer analysis of the matched metal mold consolidation assembly.

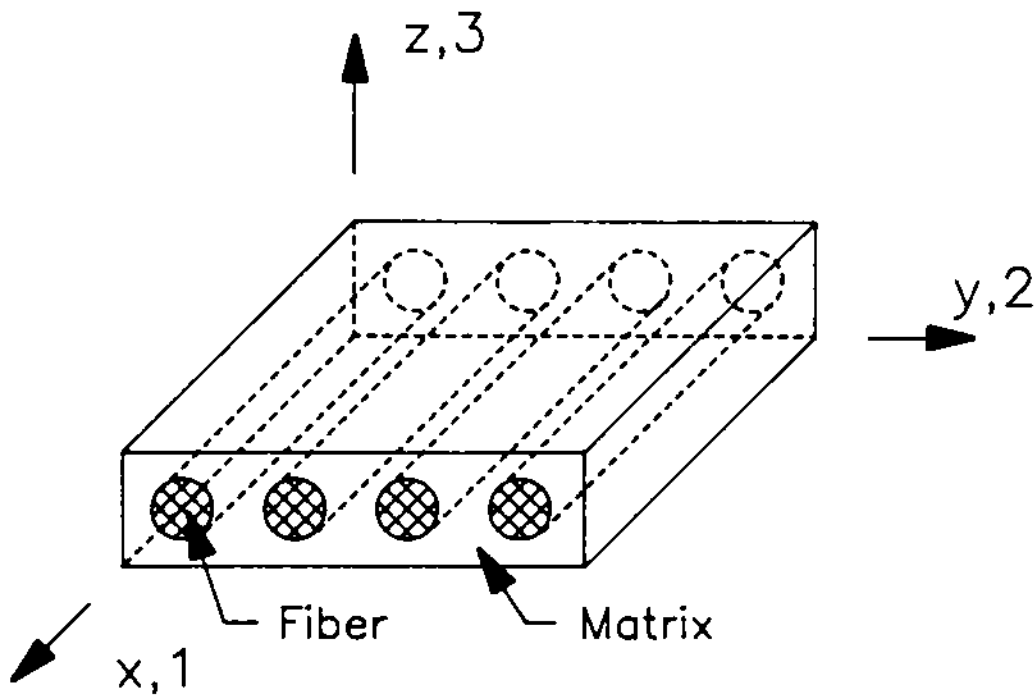

Figure 37. Simplified schematic of unidirectional prepreg and the coordinate system. [32]

where k_x, k_y, and k_z are the thermal conductivities in the three cartesian coordinate directions as shown in Figure 37, and the subscript c denotes the properties of the composite. If the prepreg is assumed to be transversely isotropic in the y-z plane, then k_y will be equal to k_z .

For a unidirectional composite, the thermal conductivity in the fiber direction, k_x, is much greater than the thermal conductivities normal to the fiber (i.e. k_y, k_z). Hence, the temperature distribution along the fiber direction (x-direction) is very uniform and the problem can be simplified to determining the temperature distribution in the y-z cross-section shown in Figure 37. Equation 5.1 can be simplified and becomes:

$$\rho_c C_{pc} \frac{\partial T}{\partial t} = \frac{\partial}{\partial y}\left(k_y \frac{\partial T}{\partial y}\right) + \frac{\partial}{\partial z}\left(k_z \frac{\partial T}{\partial z}\right) \tag{5.2}$$

For the mold, the material is assumed to be isotropic and the two dimensional transient heat conduction equation can be written as

$$\rho_m C_{pm} \frac{\partial T}{\partial t} = \frac{\partial}{\partial y}\left(k_m \frac{\partial T}{\partial y}\right) + \frac{\partial}{\partial z}\left(k_m \frac{\partial T}{\partial z}\right) \tag{5.3}$$

where ρ_m, C_{pm}, and k_m are the density, the specific heat, and the thermal conductivity of the mold respectively.

Due to the thermal as well as geometric symmetry of the problem, we analyze only one half of the composite-mold assembly (Figure 36). The initial and boundary conditions may be written in the form

Initial condition:

$$T(y, z, 0) = T_i \tag{5.4}$$

Boundary conditions:

$$\frac{\partial T(0, z, t)}{\partial y} = 0 \tag{5.5}$$

$$-k_m \frac{\partial T(W, z, t)}{\partial y} = h[T(W, z, t) - T_f] \tag{5.6}$$

$$T(y, 0, t) = T_{L.P.}(t) \tag{5.7}$$

$$T(y, H, t) = T_{U.P.}(t) \tag{5.8}$$

where T_i is the initial temperature, h is the convective heat transfer coefficient, W is the half-width of the composite-mold assembly, H is the height of the composite-mold assembly, and $T_{L.P.}$ and $T_{U.P.}$ are the temperatures of the lower and upper platens, respectively. $T_{L.P.}$ and $T_{U.P.}$ are functions of time. The fluid temperature (T_f) is equal to ambient temperature.

Solution of Equations 5.2 and 5.3 with the initial and boundary conditions given in Equations 5.4-5.8 was solved by the finite element technique using the two-dimensional finite element program FEM2D [23]. The program use a semidiscrete approximation to solve the transient heat conduction equation. A "θ" family of approximation was used to approximate the first-order time derivative.

5.1 Micromechanics Equations for Thermal Properties of Composites

Fiber-reinforced composite materials are anisotropic and heterogeneous. The properties of the composites are influenced by, but not the same as, those of the constituents [32]. Springer and Tsai [33] and Chamis [32] related the properties of the constituents (fiber/matrix) to those of the composite. A micromechanics point of view was used. Unidirectional composites were investigated because they are fundamental to the analysis and design of fiber-reinforced composite structures. The assumptions behind the micromechanics equations are [33,34]:

1. The composites are macroscopically homogeneous, linearly elastic, macroscopically orthotropic and initially stress-free.
2. Both the matrix and the fibers are homogeneous and linearly elastic. The matrix is mechanically and thermally isotropic. The fiber is mechanically isotropic but thermally anisotropic.
3. The filaments are regularly spaced and perfectly aligned.
4. The thermal contact resistance between the filament and the matrix is negligible.
5. The bonds between the fibers and matrix are perfect.

The equations suggested by Chamis [32] were used due to the completeness and the ease of use. Those which are relevant to the heat transfer analysis are listed below based on the coordinate system shown in Figure 37.

$$\rho_c = v_f \rho_f + v_m \rho_m \tag{5.9}$$

$$C_{pc} = \frac{1}{\rho c} (v_f \rho_f C_{pf} + v_m \rho_m C_{pm}) \tag{5.10}$$

$$k_x = k_1 = v_f k_{f1} + v_m k_m \tag{5.11}$$

$$k_y = k_z = k_2 = k_3 = (1 - v_f^{1/2})k_m + \frac{k_m v_f^{1/2}}{1 - v_f^{1/2}(1 - \frac{k_m}{k_{f2}})} \tag{5.12}$$

where the variables are defined as follows

- v : volume fraction of constituents.
- k : heat conductivity of constituents or composite.
- ρ : density of constituents or composite.
- C_p : specific heat of constituents or composite.

subscripts

- f : denote fiber.
- m : denote matrix.
- c : denote composite.
- x : denote x direction in the cartesian coordinates in Figure 37.
- y : denote y direction in the cartesian coordinates in Figure 37.
- z : denote z direction in the cartesian coordinates in Figure 37.
- 1 : denote 1 direction in the cartesian coordinates in Figure 37.
- 2 : denote 2 direction in the cartesian coordinates in Figure 37.
- 3 : denote 3 direction in the cartesian coordinates in Figure 37.

5.3 Experimental Procedures

Experiments was performed to verify the results of the heat transfer analysis described in Section 5.1. Preparation and consolidation of the composite laminate were similar to the procedures discussed in Section 4.2.2.

A 64-ply composite laminate was constructed from 305 mm (12 in) wide, 0.163 mm (0.0064 in) thick unidirectional graphite fiber (Thornel T300), polysulfone matrix (Udel P1700) prepreg tape. The prepreg was manufactured by Amoco Performance Products and had a fiber volume fraction of 60%. Prepreg was manufactured using a solventless technique. The prepreg was cut into 152 mm (6 in) square sheets and the sheets were stacked on top of each other to form a 64-ply unidirectional lay-up. The lay-up was placed into the cavity of the mold assembly and plunger was installed over the top of the lay-up. The surfaces of the mold assembly in contact with the prepreg were treated with Freekote 33 mold release agent.

In order to measure the temperature distribution in the composite-mold assembly during processing, seven thermocouples were embedded inside the laminate and six thermocouples were placed around the mold. Figure 38 and 39 show the dimensions of the processing assembly and the locations of the thermocouples. The composite was processed in a Tetrahedron Pneumapress hot press. The press was preheated to 300°*C* (572°*F*) and the composite-mold assembly was placed into the press and the platens closed. During heat-up, an initial contact pressure of 24 kPa (3.5 psi) was applied. When the temperature of the composite reached 288 °*C* (550°*F*), a consolidation pressure of 2068 kPa (300 psi) was applied for 30 minutes. During processing, the outputs of the thirteen thermocouples were continuously recorded by a HP 3479A Data Acquisition/Control Unit. After consolidation for 30 minutes, the platen heaters were turned off and the composite was allowed to cool under pressure. When the temperature of the composite dropped below the T_g of polysulfone, the pressure was released and the assembly was removed from the press.

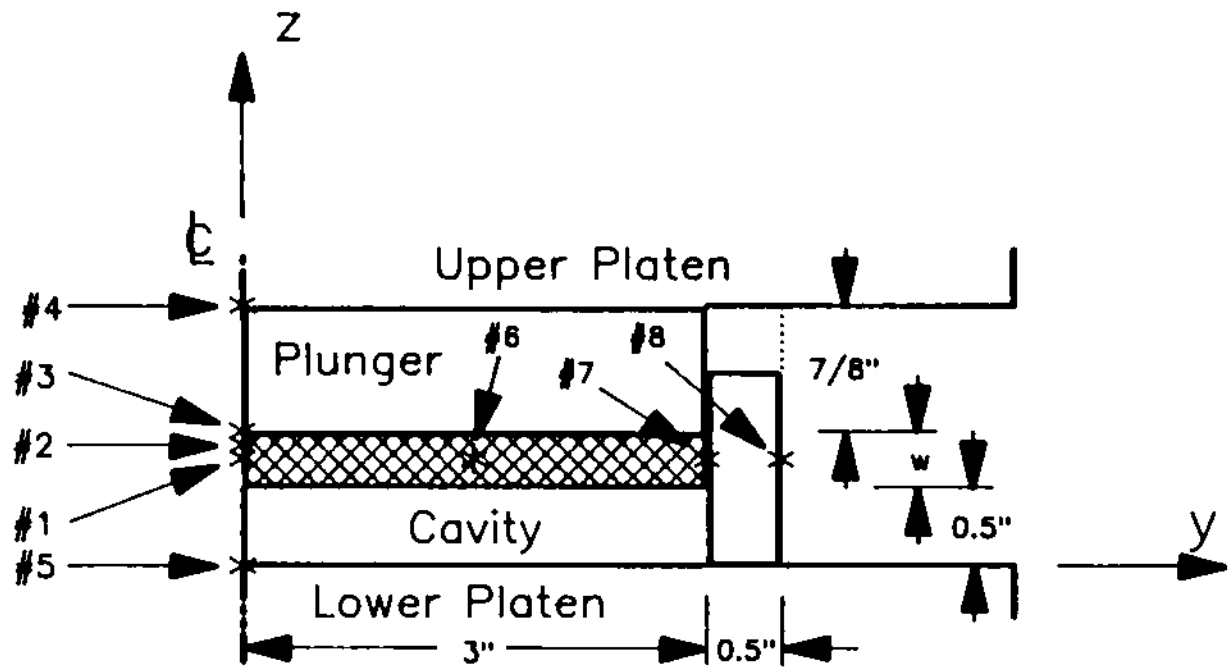

Figure 38. Cross-section of the 64-ply T300/P1700 unidirectional composite processing assembly and locations of the thermocouples.

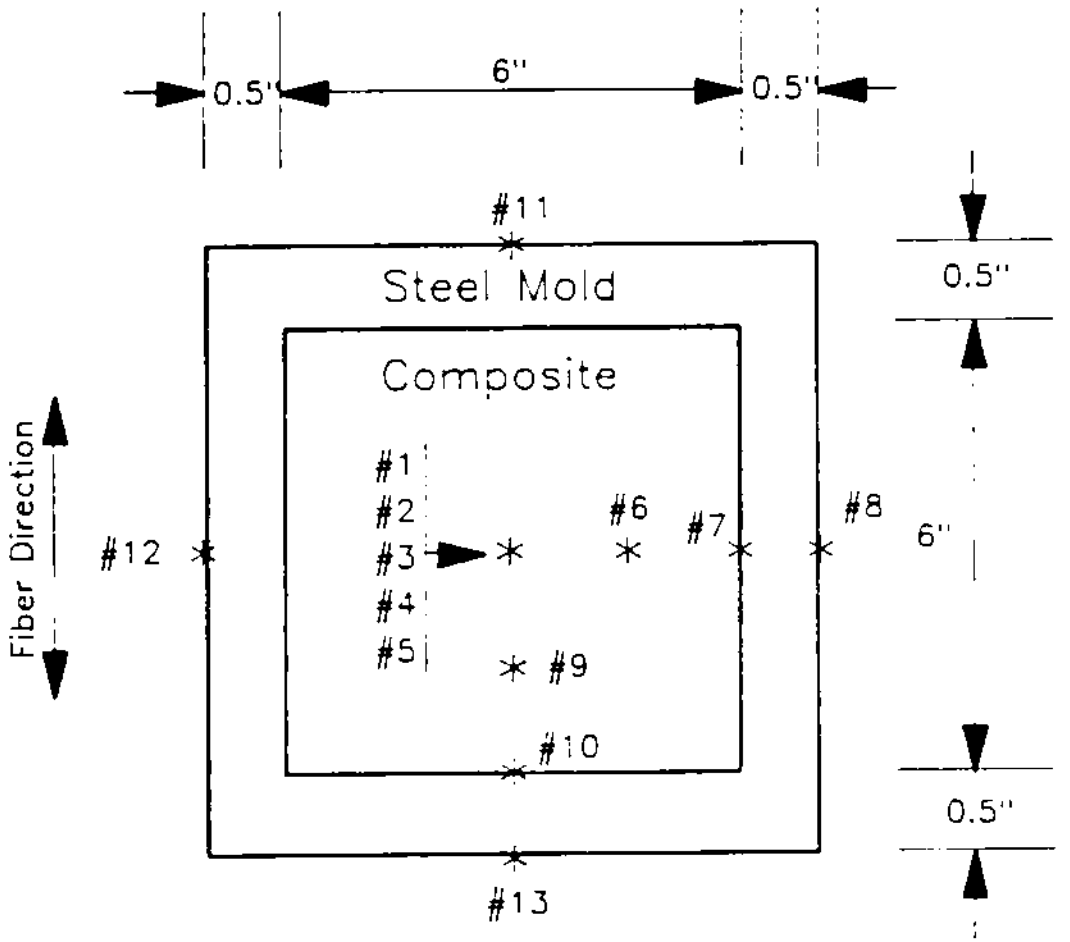

Figure 39. Top-view of the 64-ply T300/P1700 unidirectional composite processing assembly and the locations of the thermocouples.

The composite was reprocessed a second time using the above processing cycle. The laminate quality was good after the second processing. There was a small amount of fiber and resin squeezed out after processing. The C-scan result is shown in Figure 40. The average thickness of the laminate was 8.66 mm (0.341 in).

The main difference between the two processing runs was that spatial gaps existed between each layer of prepreg in RUN #1. Intimate contact was not achieved completely during RUN #1. The intimate contact assumption is valid for Run #2. Therefore, some differences between the calculated and the measured temperatures in RUN #1 are expected.

5.4 Comparison Between Heat Transfer Analysis and Experimental Data

In this section the results of the FEM heat transfer analysis are presented and compared with the temperature distribution measured during processing of a 64-ply graphite/polysulfone composite.

The thermophysical properties of the composite were calculated using the micromechanics expressions presented in Section 5.3. The constituent and composite properties are tabulated in Table 3.

As shown in Table 3, k_y and k_z are much smaller than k_x. This justifies the assumption of uniform temperature along the fiber direction.

Dimensions of the composite-mold assembly cross-section analyzed are shown in Figure 38. The thickness of the composite (w) was taken to be 10.44 mm (0.411 in) for RUN #1 and 8.66 mm

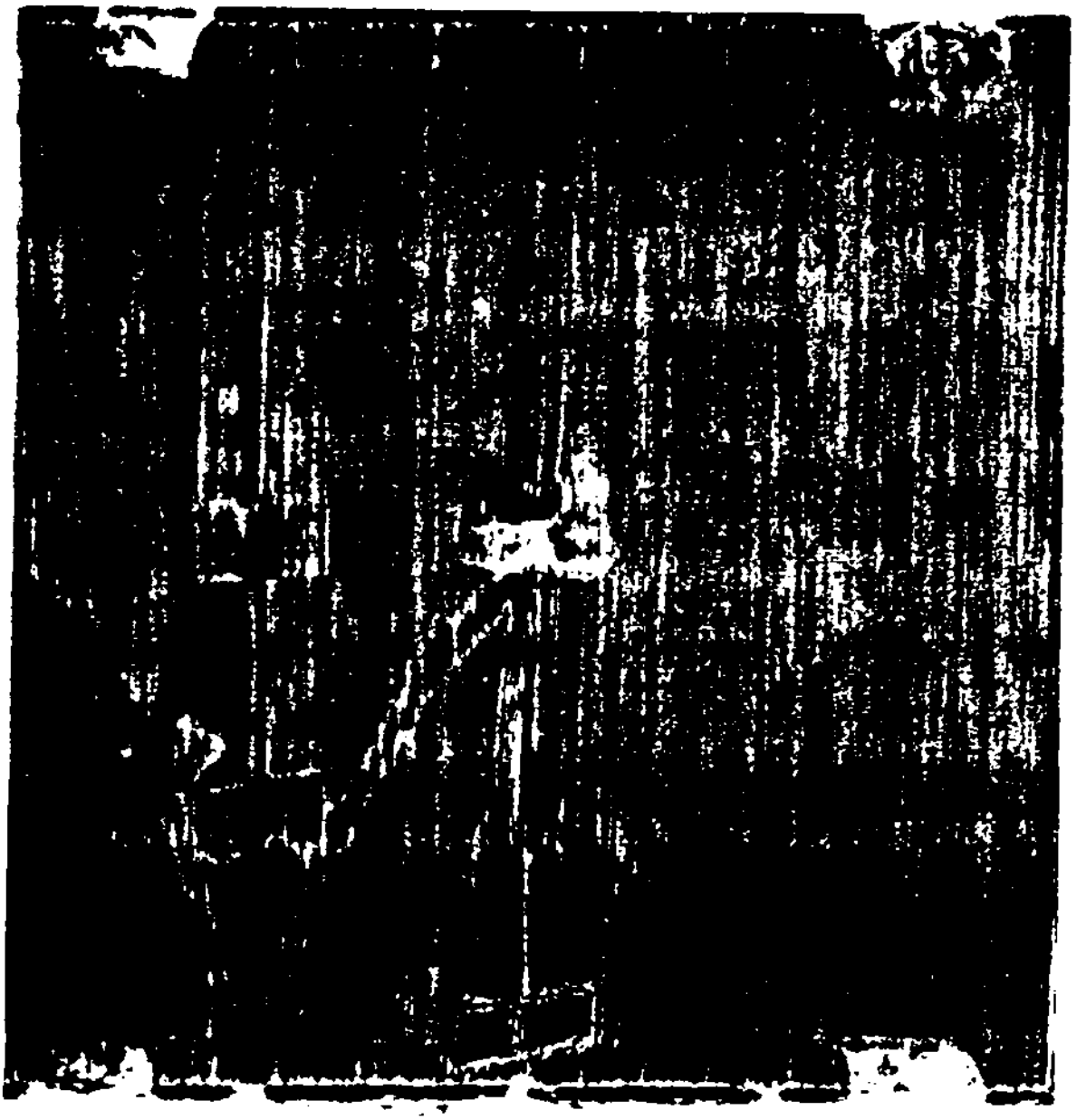

Figure 40. C-scan results of the 64-ply T300/P1700 unidirectional composite after the second process.

Table 3. Material properties used in analyzing heat transfer in a unidirectional 64-ply T300/P1700 composite.

	T300 Graphite Fiber (Amoco)	Polysulfone (Amoco)	Steel [36]	Composite
$\rho(Kg/m^3)$	1,772	1,240	7,801	1,559
$C_p(KJ/Kg°C)$	1.13(at 175°C)	1.13	0.473	1.13
$k_x(W/m°C)$	8.65	0.26	2.22	5.29
$k_y(W/m°C)$	4	0.26	2.22	0.79
$k_z(W/m°C)$	4	0.26	2.22	0.79
$v_f(\%)$	X	X	X	60

(0.341 in) for Run #2. The finite element mesh and boundary conditions are shown in Figure 41. Four-node, isoparametric, rectangular elements were used in the analysis.

The upper temperature boundary conditions ($T_{U,P}(t)$) and lower temperature boundary conditions ($T_{L,P}(t)$) for the two tests were measured during processing and are shown in Figure 42.

In the computations, the boundary temperatures were changed every 10 seconds for the first 20 minutes and every minute afterwards. Linear interpolation was used to determined the boundary temperatures between successive data points.

In the finite element program, the time parameter θ was taken to be 0.878 [35]. Time increments of 2.5 seconds for the first 20 minutes and 20 seconds afterwards were used.

A subroutine was developed to calculate the heat transfer coefficient (h) at each time step. The subroutine is based on the experimental equations suggested by Churchill and Chu [36] for the case of free convection past a vertical surface. The equations are listed as follows:

$$N_L = 0.68 + 0.67Ra_L^{1/4}[1 + (\frac{0.492}{Pr})^{9/16}]^{-4/9} \qquad 0<Ra_L<10^9 \qquad (5.13)$$

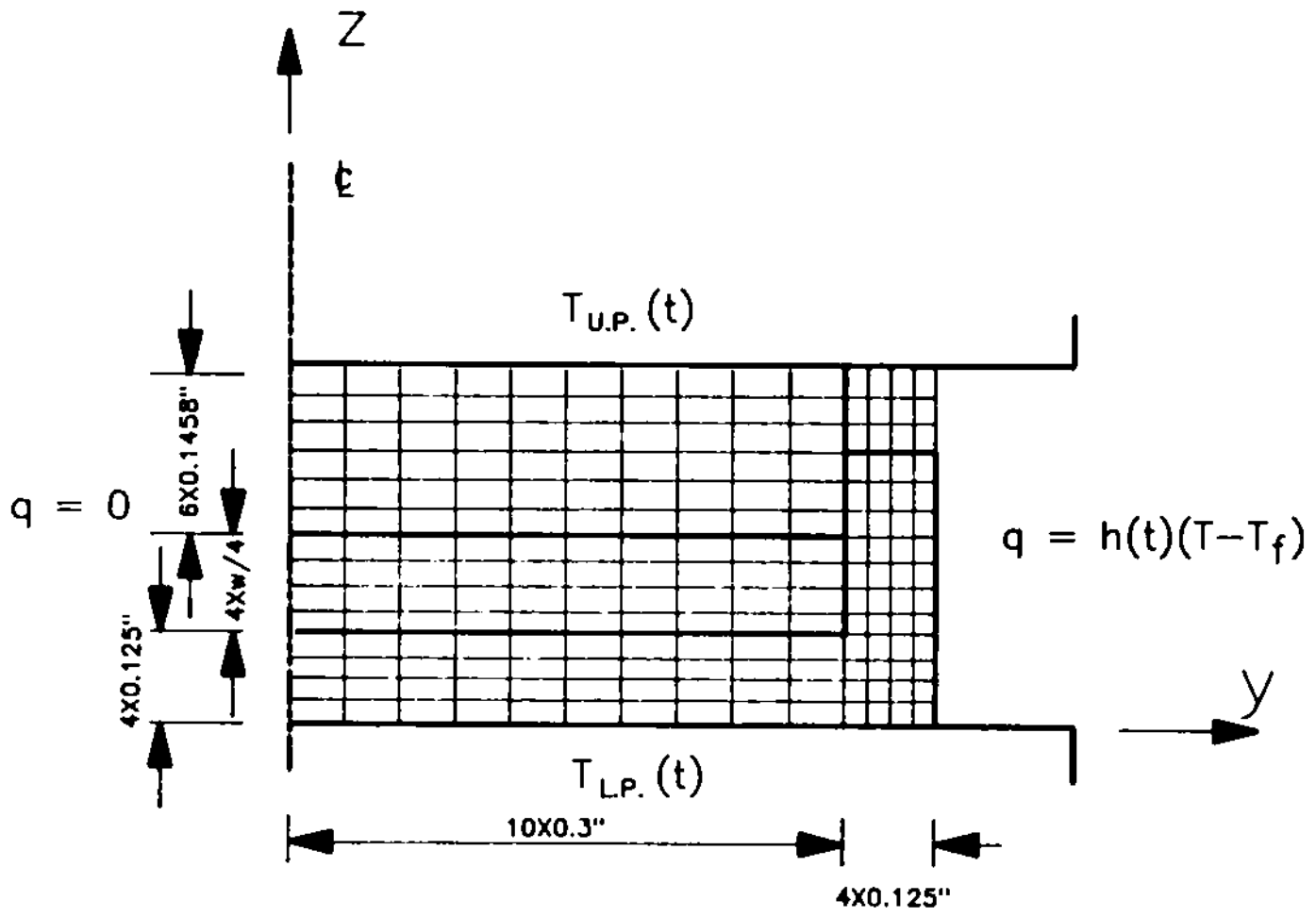

Figure 41. Finite element mesh and boundary conditions used in the consolidation simulation of the 64-ply T300/P1700 unidirectional composite.

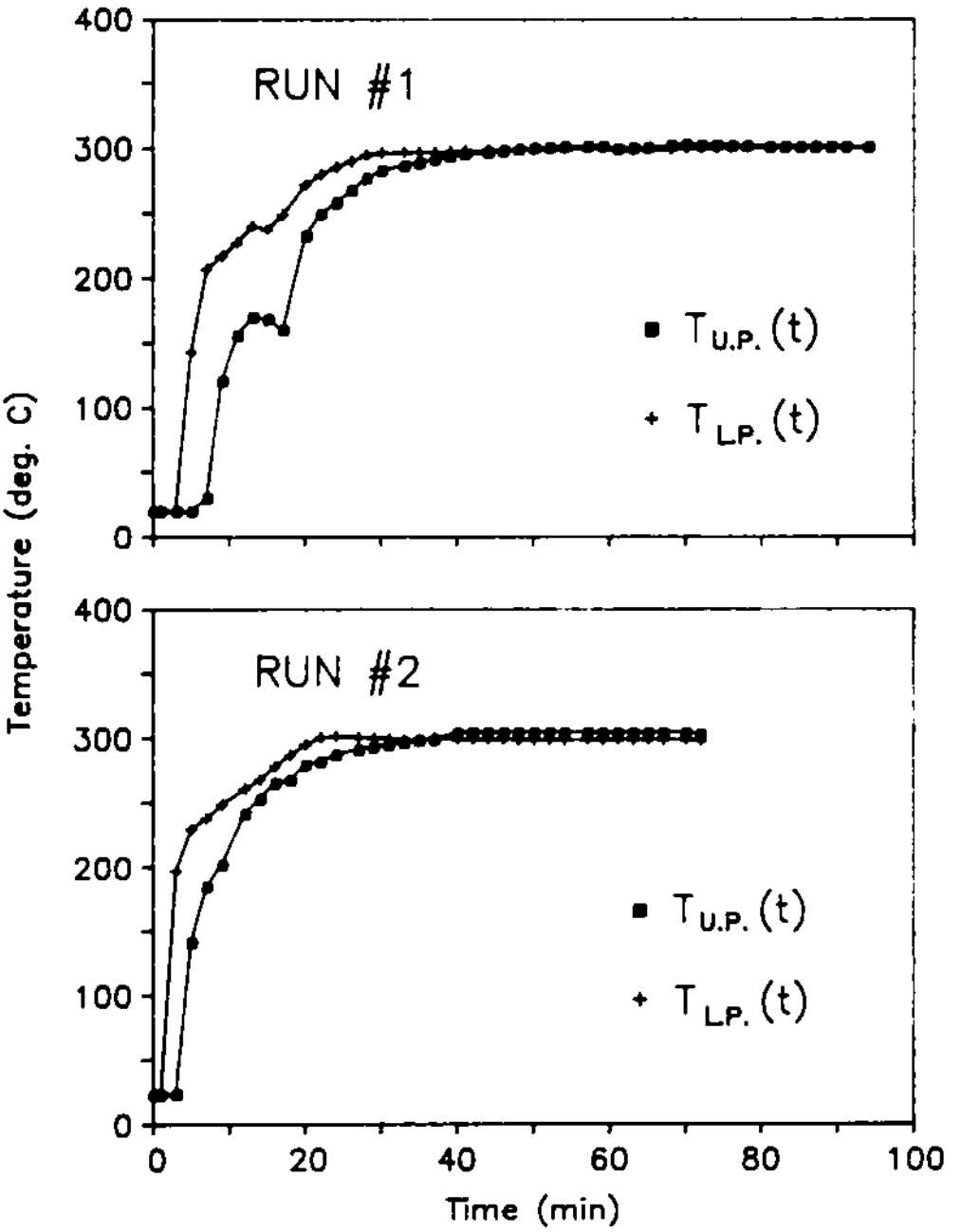

Figure 42. Upper and lower boundary conditions of the 64-ply T300/P1700 unidirectional composite processing assembly.

$$N_L = \{0.825 + 0.387 Ra_L^{1/6}[1 + (\frac{0.492}{Pr})^{9/16}]^{-8/27}\}^2 \qquad 10^9 < Ra_L \qquad (5.14)$$

- Ra_L : Rayleigh number based on the vertical plane length L .
- Pr : Prandtl number ($\frac{\mu C_p}{k}$) of the surrounding fluid. Where μ is the coefficient of dynamic viscosity, C_p is the specific heat, and k is the conductivity.
- N_L : Nusselt number ($\frac{hL}{k}$). Where h is the heat transfer coefficient, L is the length of the convection surface.

The Rayleigh number Ra_L in the above equations is defined as follows:

$$Ra_L = \frac{L^3 g\beta \Delta T Pr}{\nu^2} \qquad (5.15)$$

- g : acceleration of gravity ($9.81 m/\sec^2$).
- β : coefficient of thermal expansion ($\frac{1}{T°K}$ for ideal gases).
- ΔT : difference between fluid temperature and the averaged surface temperature.
- ν : coefficient of kinetic viscosity of surrounding fluid.

All the properties, except β, are evaluated at the mean between the temperature of the surrounding fluid and the average surface temperature. β is evaluated at the room temperature.

In the subroutine, the Rayleigh number (Equation 5.15) was calculated first from the temperature difference (ΔT) between the ambient (room temperature) and the average surface temperature. Then, either Equations 5.13 or 5.14 was used to calculate the Nusselt number based on the magnitude of the Rayleigh number. The heat transfer coefficient (h) is calculated from the Nusselt number. The new value of h will be used in the next time step.

Comparisons between the measured temperature distribution and the temperature distribution calculated using the FEM heat transfer analysis for the 64-ply graphite/polysulfone composite are

shown in Figures 43 and 44. From Run #1 (Figure 43) the measured temperature is lower than the calculated temperatures during the first 50 minutes of processing. This difference is probably due to low initial press pressure at the beginning of the processing cycle. The low contact pressure was not sufficient to achieve complete intimate contact of the ply interfaces and the thermocouples did not have good thermal contact with the surface of the plies. When full consolidation pressure was applied, the measured and calculated temperatures agreed well.

When the composite was reprocessed in RUN #2 (Figure 44), the laminate was fully consolidated during the entire processing cycle. The agreement between the measured and calculated temperatures was excellent during the early part of the processing.

Shown in Figures 45 and 46 are fiber direction (x-direction) temperature distributions measured during processing. As assumed in the analysis, the high thermal conductivity in the fiber direction results in a uniform composite temperature distribution in this direction.

The convective heat loss from the edge of the mold was determined using the heat transfer coefficients calculated from Equations 5.13 and 5.14. The validity of this analysis was checked by comparing the measured and the calculated temperature at the boundary of the mold. As can be seen from Figure 47, there is reasonably good agreement between the results of the FEM model and the data.

The non-isothermal autohesion model described in Section 3.3 was used to calculate interply bond strength development during processing of the 64-ply graphite/polysulfone composite. The finite element model presented in Sections 5.1 and 5.2 was used to calculate the composite temperature distribution. Results of the analysis are shown in Figure 48. Assuming intimate and complete contact of the ply interfaces, interply bond formation begins after about 20 minutes into the processing cycle. The model predicts that all ply interfaces will be completely bonded ($R = 1$) in about 31 minutes.

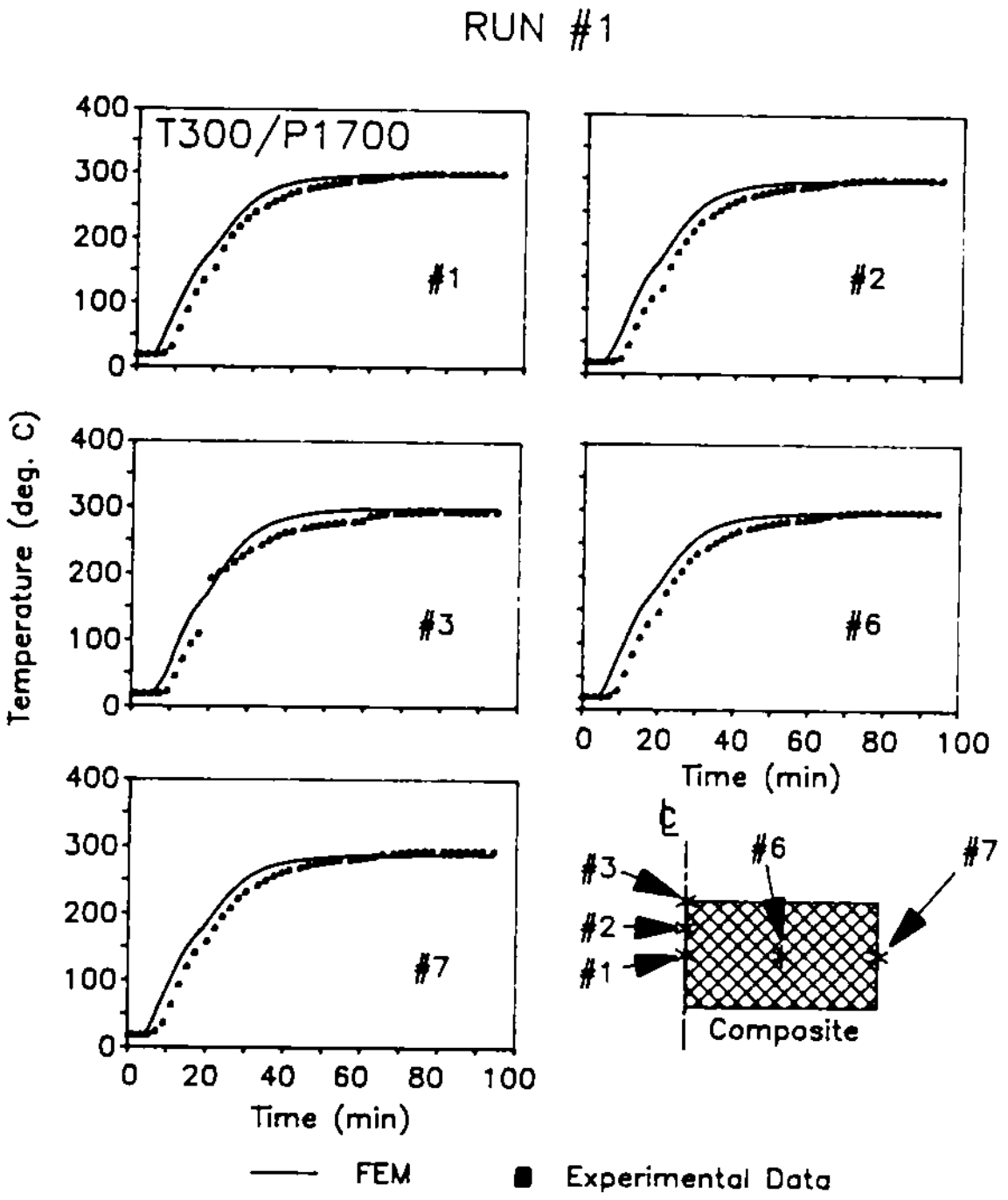

Figure 43. Temperature versus time at five positions in a 64-ply T300/P1700 unidirectional composite. Comparisons between the data (symbols) and the results computed by the model (solid lines). (RUN #1)

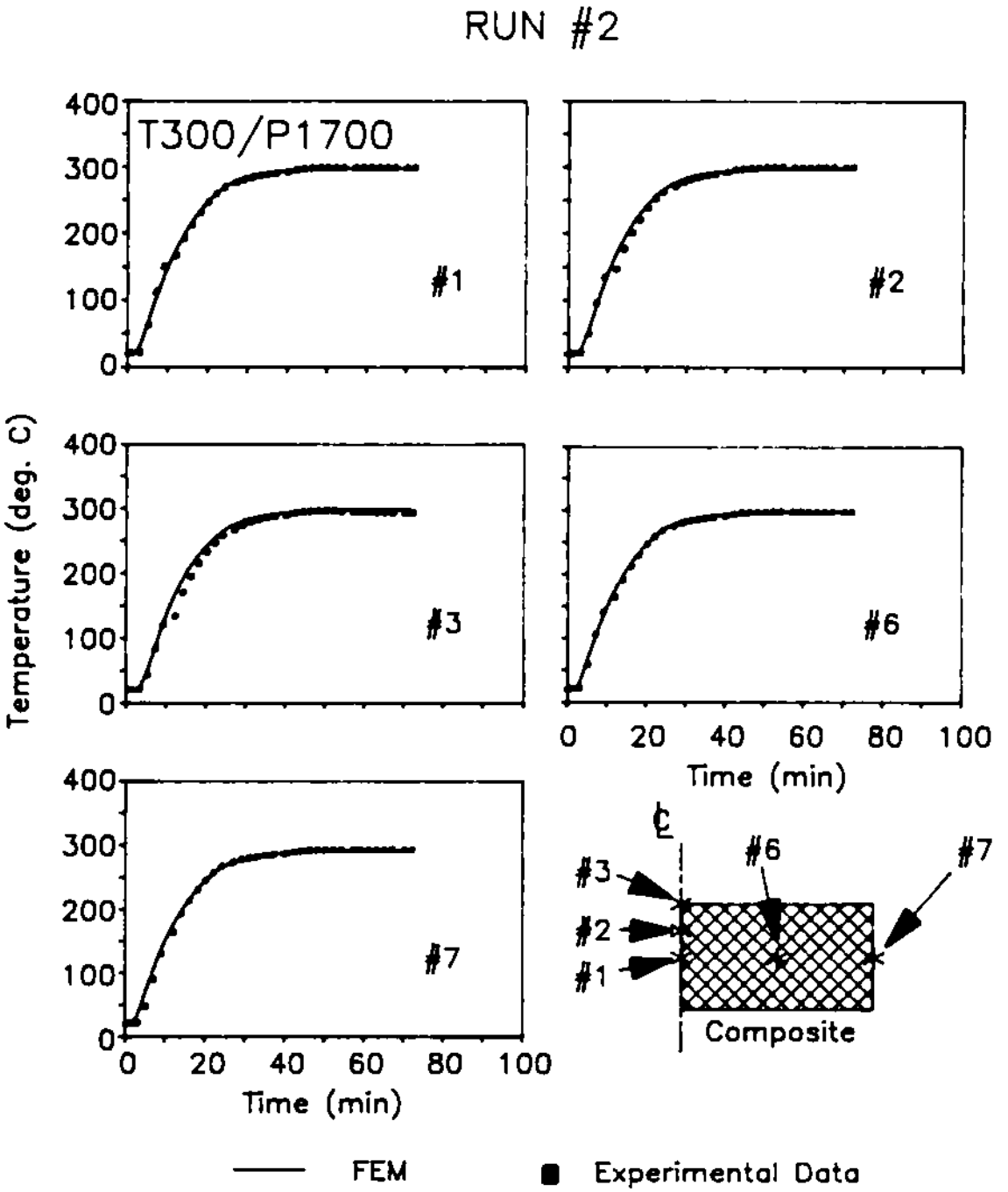

Figure 44. Temperature versus time at five positions in a 64-ply T300/P1700 unidirectional composite. Comparisons between the data (symbols) and the results computed by the model (solid lines). (RUN #2)

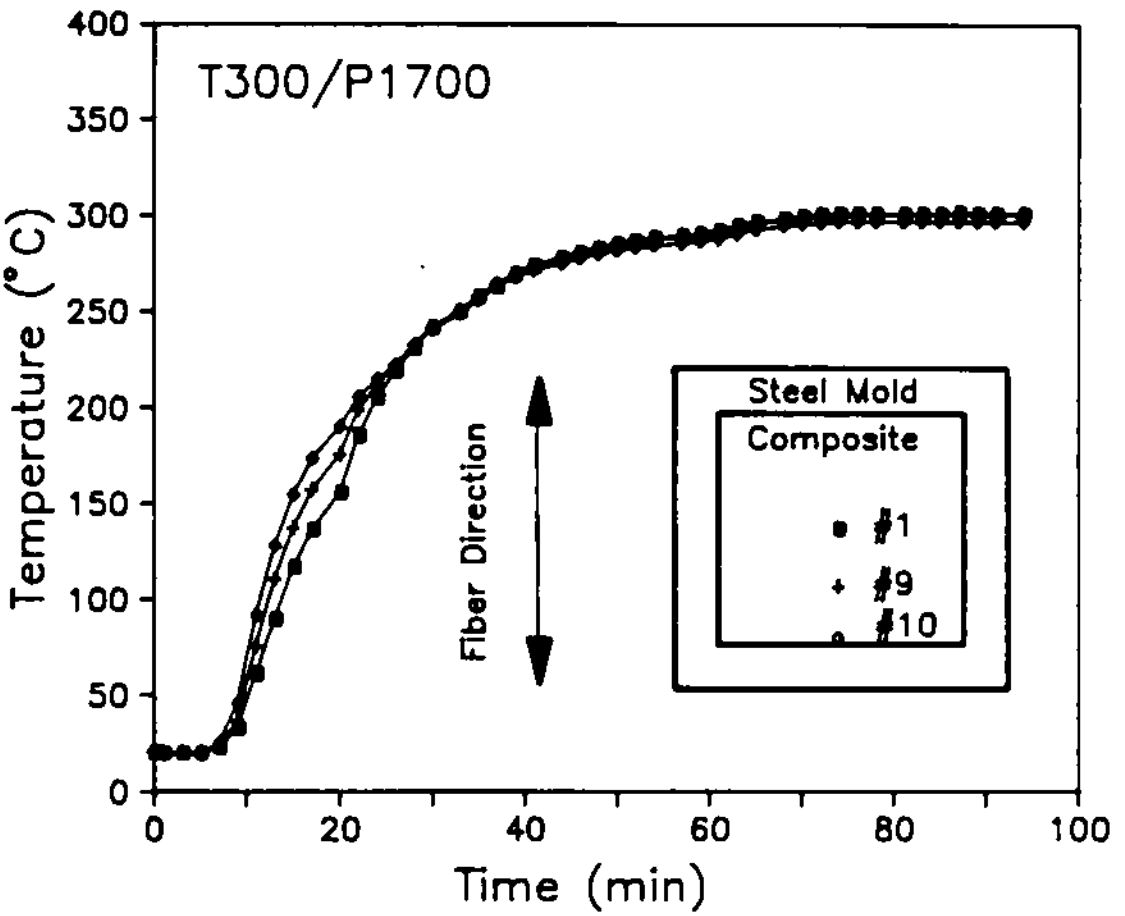

Figure 45. Temperature versus time at three positions along the fiber direction in a 64-ply T300/P1700 unidirectional composite. (RUN #1)

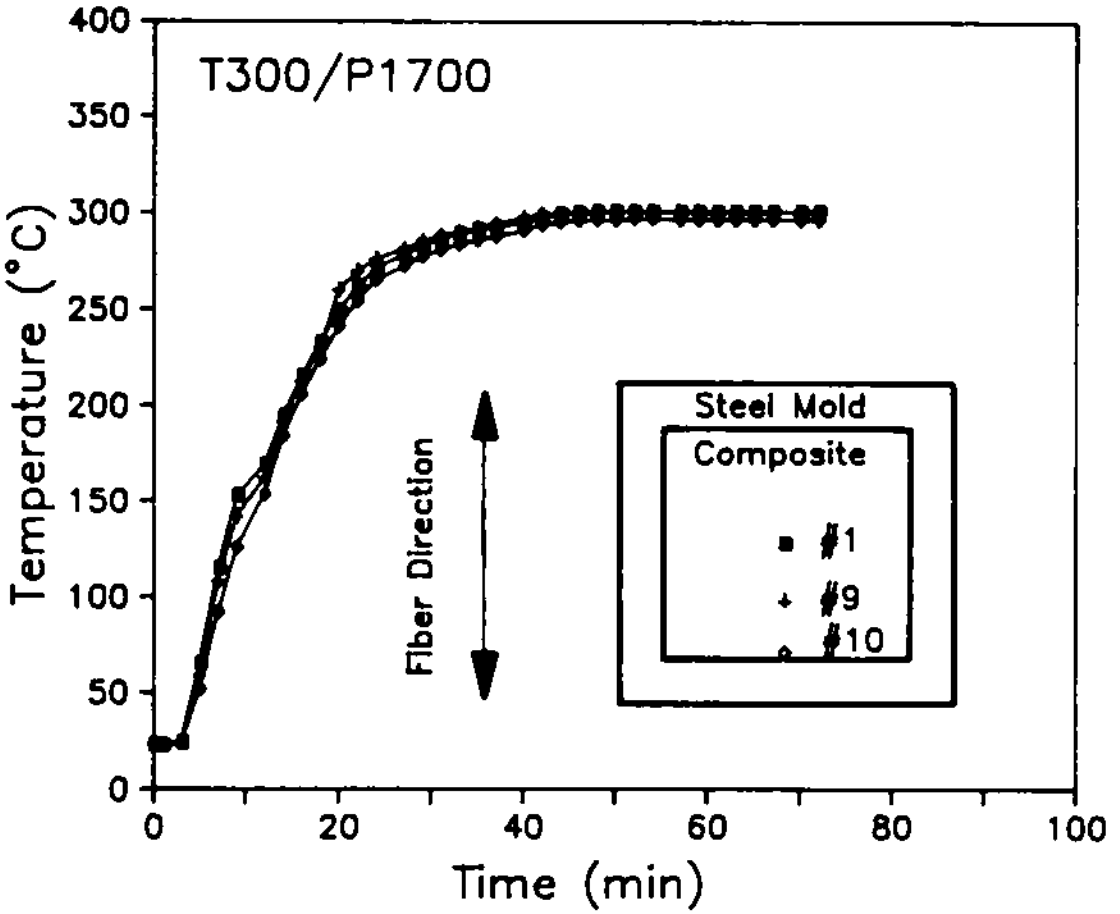

Figure 46. Temperature versus time at three positions along the fiber direction in a 64-ply T300/P1700 unidirectional composite. (RUN #2)

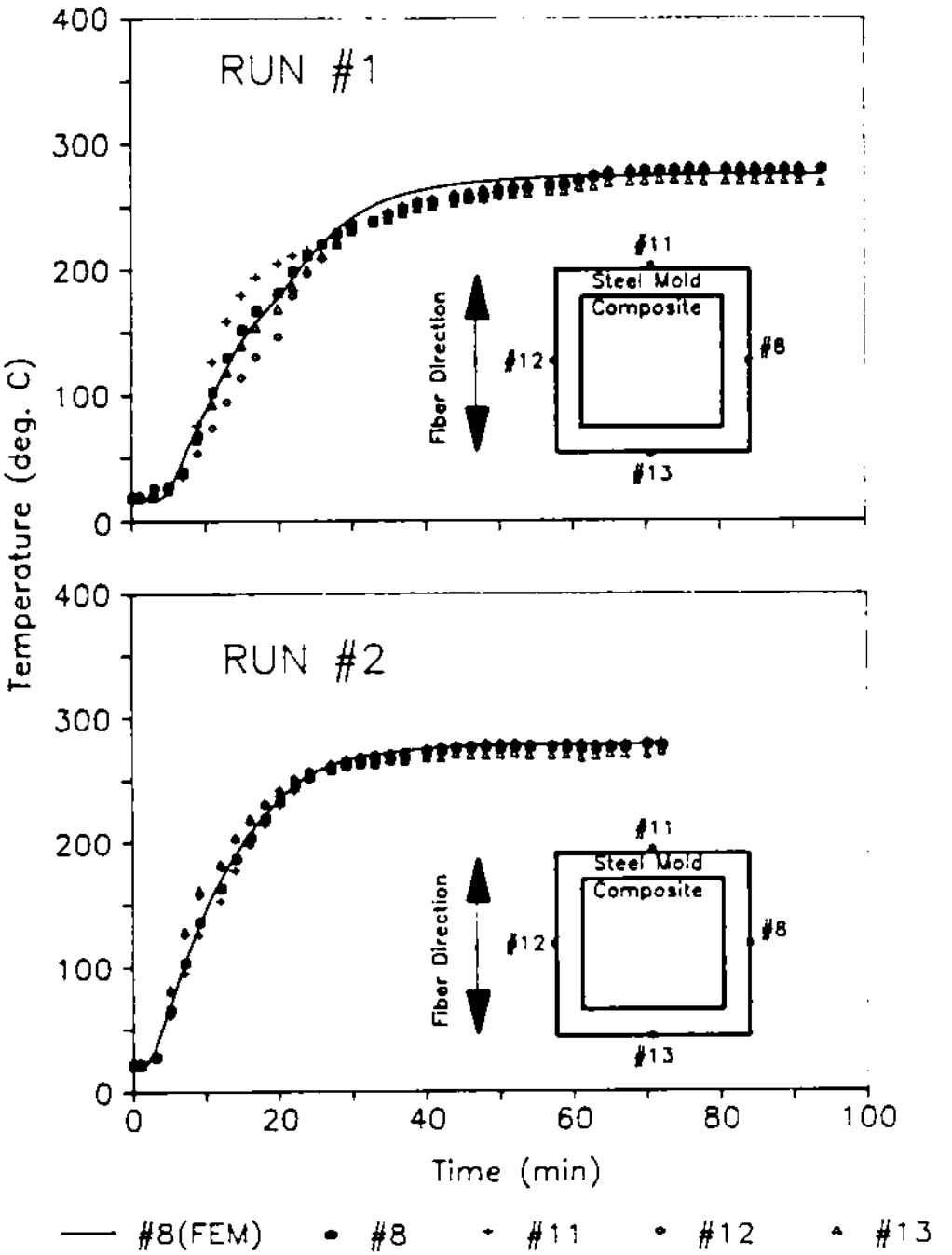

Figure 47. Temperature versus time at the convective boundaries of a 64-ply T300/P1700 unidirectional composite. Comparisons between the data (symbols) and the results computed by the model (solid lines).

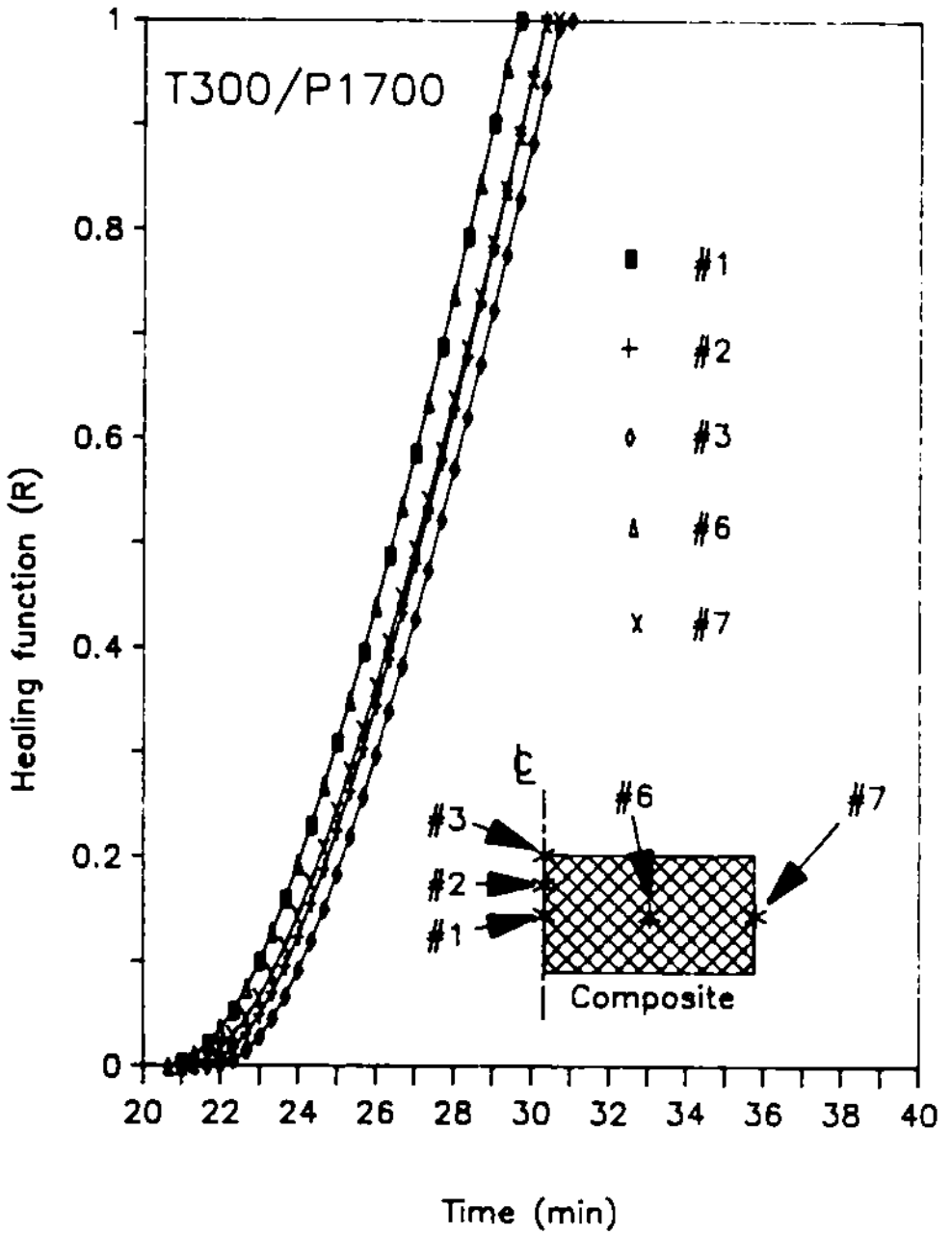

Figure 48. Model estimation of interply strength development for the RUN #1 test at five positions in the 64-ply T300/P1700 unidirectional composite.

In Figure 28 of Chapter 4, the healing function from the DCB test was measured to be $R = 0.86$ after processing at 288°C and 2068 kPa (300 psi) for 30 minutes. However, the non-isothermal autohesion model predicted that a 64-ply composite will be fully consolidated (R = 1) in about 11 minutes. This difference is probably due to the complex interfacial conditions that are not included in the model formulation at the present time, at the fracture interfaces of the DCB specimens in the healing test. The extra resin flow cost extra time to achieve intimate contact for the DCB specimens. Without considering the pressure effects in the non-isothermal autohesion model, the interply bond development was achieved in a shorter time. Furthermore, the strength of the healed interface which had been fractured would be theoretically lower than that of an undamaged interface no matter what the healing parameters the fractured interface was exposed to.

The non-isothermal autohesion model was also used to predict the time required to completely bond the ply interfaces of a 192-ply unidirectional graphite/polysulfone composite in the processing assembly shown in Figure 49. Again, it was assumed all interfaces were in intimate contact when bonding first begins. Therefore, the effects of consolidation pressure were not considered. Temperatures of the upper and lower platens (T_p, Figure 49) were assumed to be constants. T_p was taken to be 288°C.

The results of the model prediction of the interply bond development in a 192-ply unidirectional graphite/polysulfone composite are shown in Figures 50 to 53. Figure 50 shows the temperature variations at the center of the composite (y = 0, z = 0, Figure 49) and at the composite-mold boundary (y = 15.24 cm, z = 0, Figure 49). Because the platen temperature (T_p) was assumed to be constant, the temperatures in the composite are expected to rise very fast to the steady state. Figures 51 and 52 show the temperature distributions at six different times along the y and z axes. The temperature distribution in the y axis are uniform except in the region close to the composite-mold boundary. Figure 53 shows the predictions of interply bond development at the center of the composite (y = 0, z = 0, Figure 49) and at the composite-mold boundary (y = 15.24 cm, z = 0, Figure 49). Due to the nonuniform temperature distribution, autohesive bonding occurs at different rates throughout the laminate. For example, in the midplane of the composite, the plies

will be completely bonded at the composite-mold boundary in about 2 minutes while complete bonding of the plies takes about 6 minutes at the center.

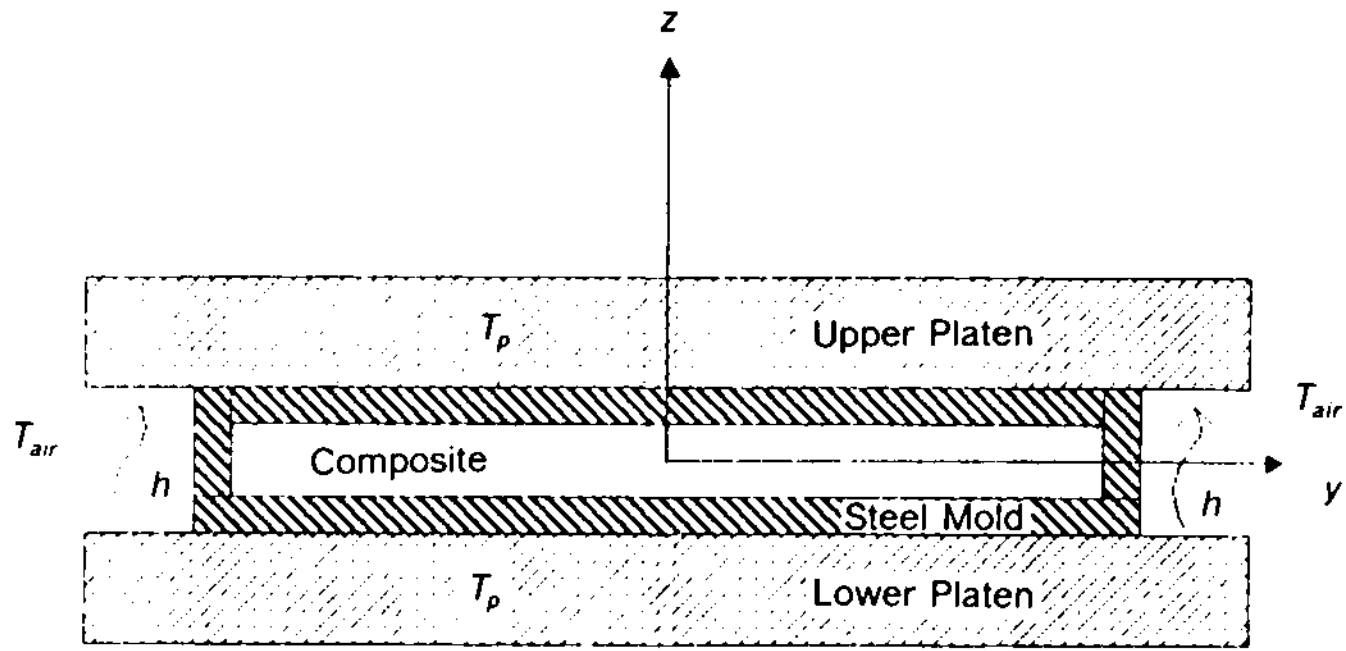

Figure 49. Cross-section of the 192-ply AS4/PI700 unidirectional composite processing assembly.

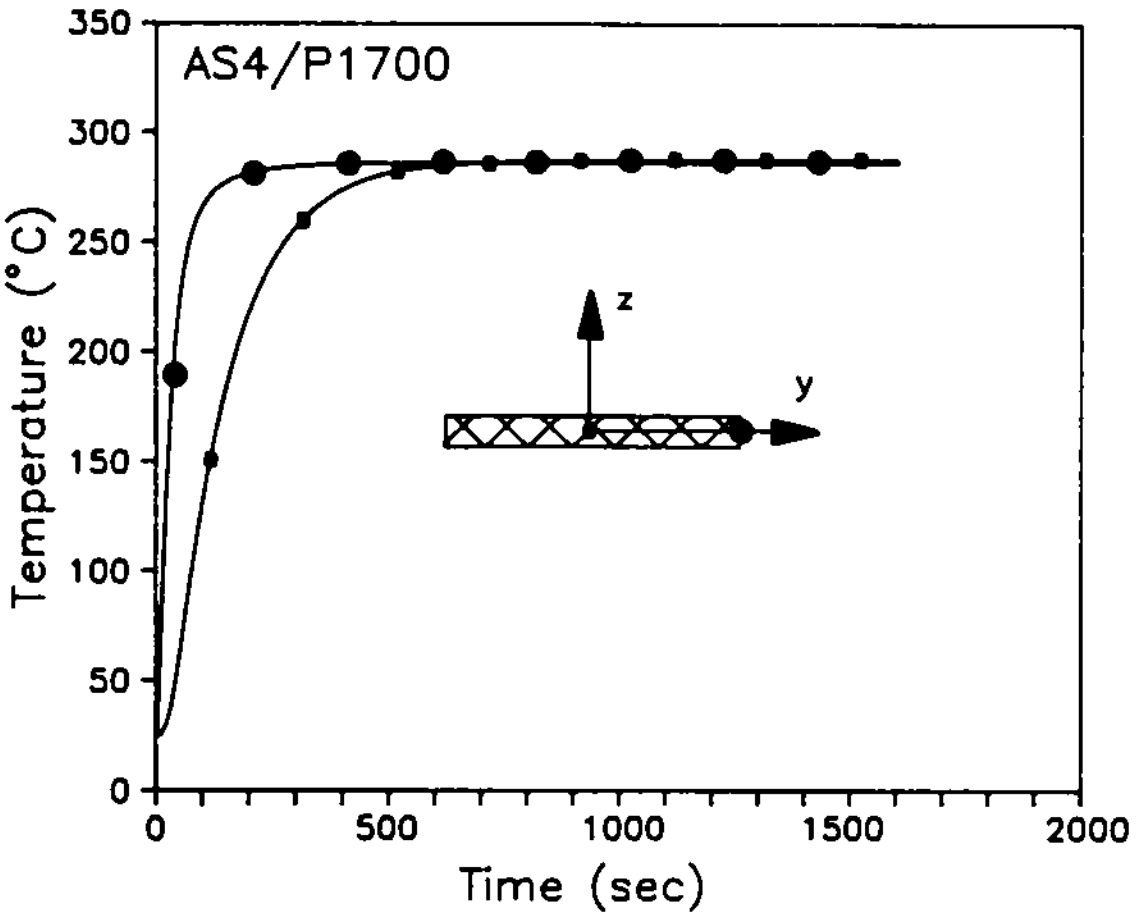

Figure 50. Temperature versus time at two positions inside a 192-ply AS4/P1700 unidirectional composite. The processing temperature is 288°C.

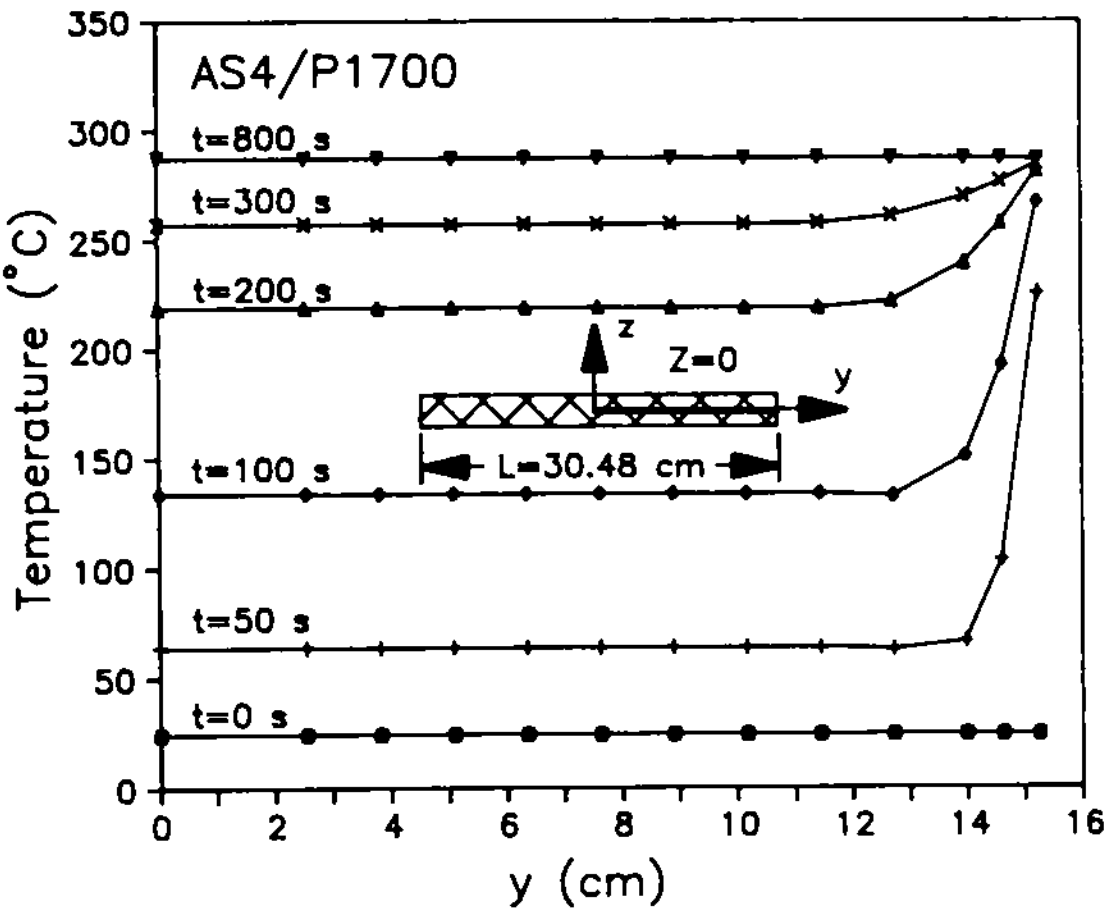

Figure 51. Temperature distribution along the horizontal centerline (y-axis) of the 192-ply AS4/P1700 unidirectional composite. The processing temperature is 288°C.

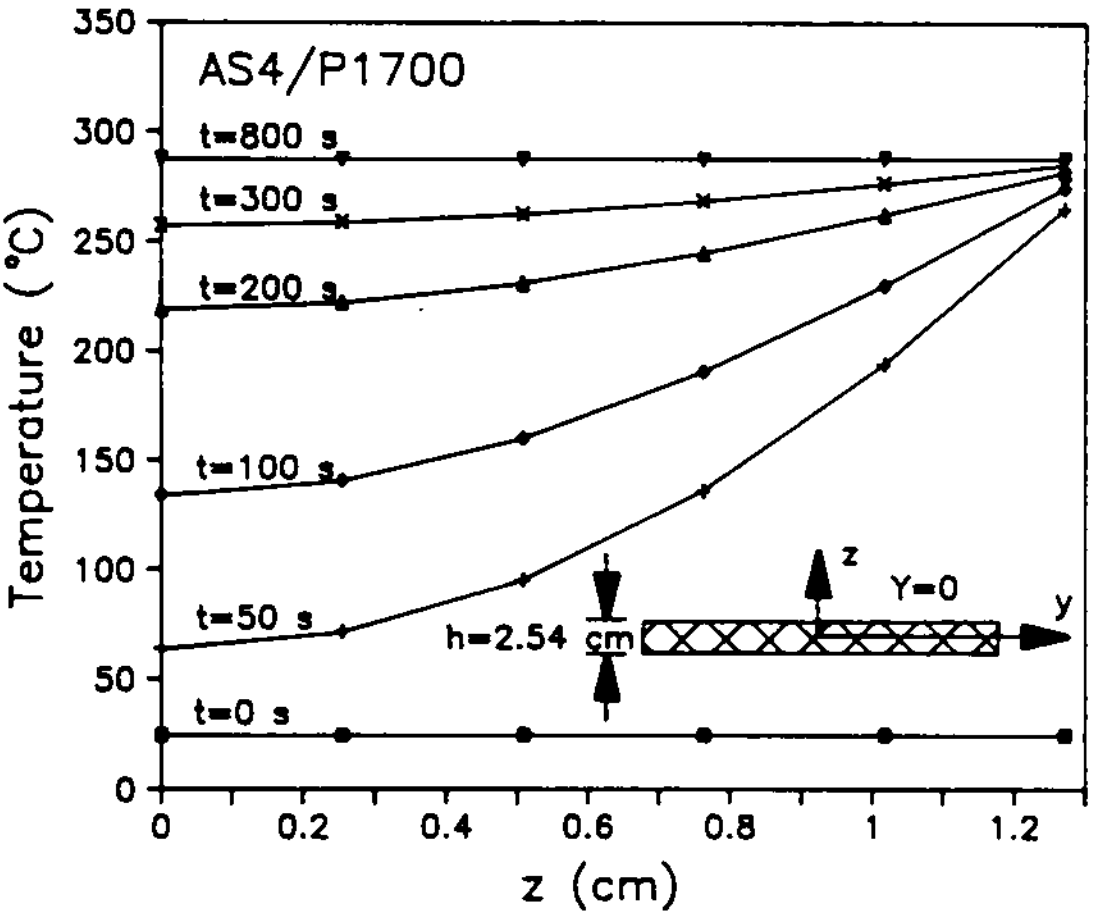

Figure 52. Temperature distribution along the vertical centerline (z-axis) of the 192-ply AS4/P1700 unidirectional composite. The processing temperature is 288°C.

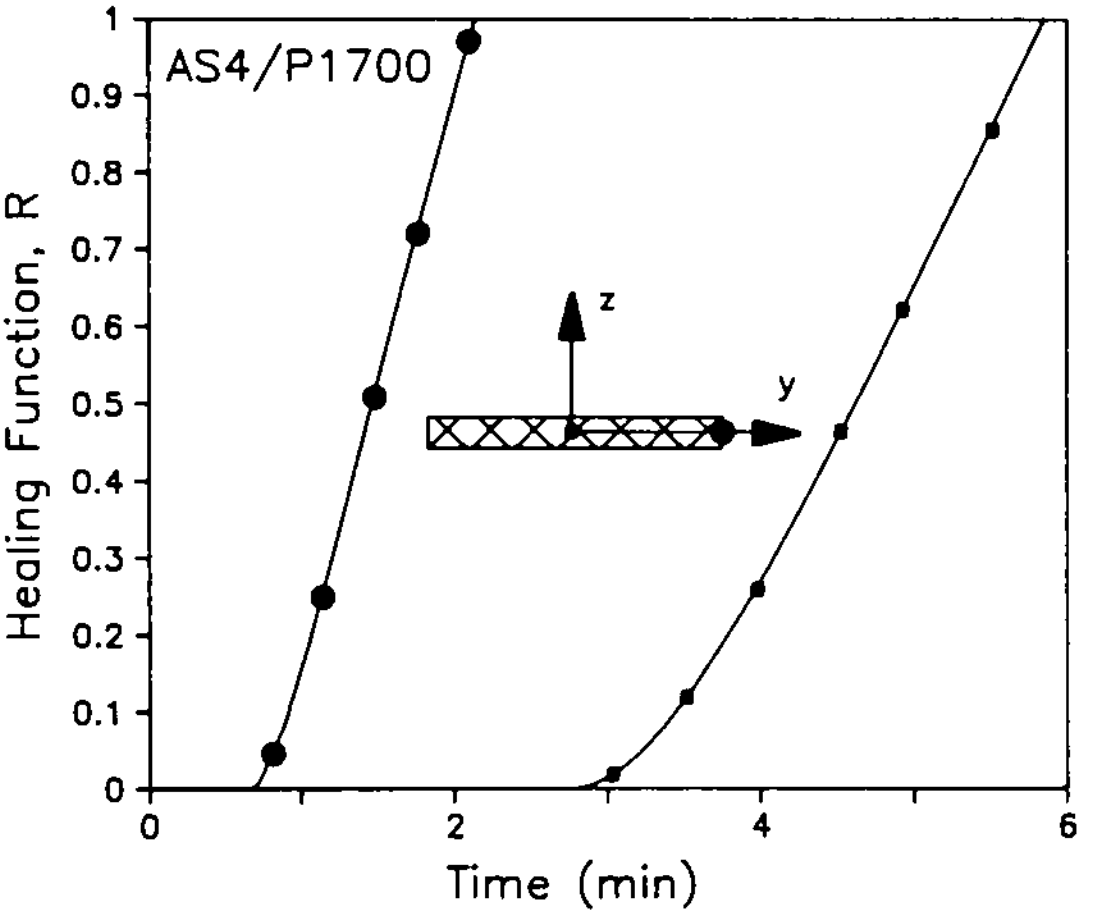

Figure 53. Model estimation of interply strength development at two positions in the 192-ply AS4/P1700 unidirectional composite. The processing temperature is 288°C.

6. Summary of Results

A non-isothermal autohesion model was developed by combining a transient finite element heat transfer model with the isothermal autohesion model. The results of the non-isothermal autohesion model were compared with the data obtained from healed P1700 polysulfone compact tension specimens by Howes and Loos [2]. The transient finite element heat transfer model estimated the temperature variations in the CT specimen very well. The non-isothermal autohesion model accurately predicted the onsets of autohesive bond formation and the times required for complete autohesive bonding for temperatures close to T_g of the resin (196°C). At higher temperatures, the model did not match the data as well, because most of the bonding occurred non-isothermally and the temperature dependence of the healing function was extrapolated from lower temperature data.

A healing test for studying interply bond development in AS4/P1700 unidirectional composites was examined. The double cantilevered beam test was selected. Fiber-bridging and fiber-breakage were observed in both the virgin and healed DCB specimens. The contributions of the fiber-bridging and breakage to the G_{IC} were much smaller for the healed specimens. The results showed the dependency of interply bond formation on the processing parameters (i.e., time, temperature and pressure). A plateau value of the healing function R was reached as each of the processing parameters was increased. As observed in the healing function (R) versus pressure graphs, the pressure is a key factor in the healing process. Higher pressure accelerated deformation of resin

which achieved the intimate contact at the fractured interface. The DCB test results were supported by ultrasonic C-scan tests performed on the selected healed specimens. The C-scan results showed that the degree of intimate contact and the amount of interply bonding were improved as one of the processing parameters (i.e. temperature, pressure and time) increased.

Optical and scanning electron microscopies were used to examine the cross-sections and the fracture surfaces of the selected virgin and healed specimens. Resin pockets existed behind the Kapton inserts in the virgin specimens. Resin flow occurred across the fracture surface during healing to achieve intimate contact. The fracture surfaces were not flat. Oval-shaped fibers existed at the healed interfaces because of the loose fibers due to fiber-breakage. The fracture mechanism was quite complex due to the existence of fiber-bridging, fiber-breakage, and poor fiber/matrix interfacial bonding. The complex fracture mechanism resulted in the low fracture toughness and the high standard deviation of experimental data. A minor debonded interface next to the main fracture interface was found in some healed specimens, due to the large cross-head displacement at larger crack lengths.

Because of the complex fracture mechanism and the complex conditions at the fracture interface before healing, it is not certain if the double cantilevered beam fracture toughness test is suitable to characterize the interply bond development in amorphous thermoplastic composites. The procedures of the specimen preparation and test procedures might be modified to simplify the fracture mechanism in the DCB test. Then, a more positive conclusion might be achieved.

The non-isothermal autohesion model was modified to estimate the interply bond development in a 64-ply T300/P1700 and a 192-ply AS4/P1700 unidirectional composites.

A 64-ply T300/P1700 unidirectional composite was processed twice using the same processing cycle. The matched metal mold consolidation technique was used. In RUN #1, a difference between the measured temperature data and the calculated values was found due to the low initial contact pressure at the beginning of the processing cycle. The low contact pressure was not suffi-

cient to achieve complete intimate contact of the ply interfaces, and the thermocouples did not have good contact with the surface of the plies. After the full consolidation pressure was applied, the measured and the calculated temperatures matched well. In RUN #2, good agreement between the measured and the calculated temperatures was observed due to the full consolidation during the entire processing cycle.

The use of the Equations 5.13 and 5.14 to calculate the heat transfer coefficient at the convective boundaries was justified by the good fit between the experimental data and the calculated values. In addition, the temperature distribution along the fiber direction was shown to be uniform. This justified the use of the two-dimensional heat transfer analysis for unidirectional composites.

The interply bond formation in the 64-ply T300/P1700 unidirectional composite was predicted by the non-isothermal autohesion model. Assuming initial and complete intimate contact of the ply interfaces, interply bond strength development was completed after 31 minutes into the processing cycle, or 11 minutes after bonding began. In comparison with the data of the DCB tests ($R = 0.86$ for 288°/2068kPa (300psi)/30min), the model estimated a higher interfacial strength developing in a shorter time. This is probably due to the extra time required for the fracture interface to achieve intimate contact. Without considering pressure effects, the non-isothermal autohesion model will predict that interply bond development is achieved in a shorter time.

For the 192-ply AS4/P1700 unidirectional composite, the temperature was predicted to rise very quickly due to the constant platen temperatures and the negligence of the pressure effects. Therefore, the interply bond formation was estimated to be achieved in a very short time.

In order to more accurately predict the interply bond development in a thermoplastic composite in processing, the effects of pressure must be studied. In addition, the non-isothermal autohesion model can be modified to consider the thermophysical heterogeneity caused by more general laminate lay-ups, to take into account the heat emitted during the crystallization in a semi-crystal matrix composite, and to calculate the residual stress after processing.

Reference

[1] Newas, G. M., "Advanced thermoplastic Composites", **ASTM STANDARDIZATION NEWS**, Oct., 1987, American Society for Testing and Materials, Philadelphia, 1987, pp.32-35.

[2] Howes, J. C. and Loos, A. C., "Interfacial Strength Development in Thermoplastic Resins and Fiber-Reinforced Thermoplastic Composites", CCMS-87-15, Sept. 1987, VPI&SU, Blacksburg, VA 24061.

[3] Voyutskii, S. S., **Autohesion and Adhesion of High Polymers**, Vol. 4, **Polymer reviews**, Interscience Publishers, New York, 1963.

[4] Loos, A. C. and Dara, P. H., "Processing of Thermoplastic Matrix Composites", **Review of Progress in Quantitative Nondestructive Evaluation**, D. O. Thompson and D. E. Chimenti, Eds., Plenum Press, New York, 1987, Vol. 6B, pp.1257-1265.

[5] Wool, R. P., "Molecular Aspects of Tack", **Rubber Chemistry and Technology**, Vol. 57, 1983, pp.307-319.

[6] De Gennes, P. G., "Entangled Polymers", **Physics Today**, June 1983, pp.33-39.

[7] Wool, R. P., "Relations for Healing, Fracture, Self-Diffusion and Fatigue of Random Coil Polymers", **ACS Polymer Preprints**, Vol. 23, No. 2, 1982, pp.62-63.

[8] Wool, R. P. and O'Connor, K. M., "Craze Healing in Polymer Glasses", **Polymer Engineering and Science**, Vol. 21, No. 14, Oct. 1982, pp.970-977.

[9] Wool, R. P. and O'Connor, K. M., "A Theory of Crack Healing in Polymers", **Journal of Applied Physics**, Vol. 52, No. 10, Oct. 1981, pp.5953-5963.

[10] Wool, R. P. and O'Connor, K. M., "Time Dependence of Crack Healing", **Journal of Polymer: Polymer Letters Edition**, Vol. 20, 1982, pp.7-16.

[11] Prager, S. and Tirrel, M., "The Healing Process at Polymer-Polymer Interfaces", **Journal of Chemical Physics**, Vol. 75, No. 10, Nov. 1981, pp. 5194-5198.

[12] Jud, K., Jausch, H. H., and Williams, J. G., "Fracture Mechanics Studies of Crack Healing and Welding of Polymers", **Journal of Materials Science**, Vol. 16, 1981, pp.204-210.

[13] Skewis, J. D., "Self-Diffusion Coefficients and Tack of Some Rubbery Polymers", **Rubber Chemistry and Technology**, Vol. 39, 1966, pp.217-225.

[14] Bauer, R. F., "Investigation into the Mechanism of Tack of Rubbers", **Journal of Polymer Science: Part A-2**, Vol. 10, 1972, pp. 541-548.

[15] Rhee, C. K. and Andries, J. C., "Factors Which Influence Autohesion of Elastomers", **Rubber Chemistry and Technology** Vol. 54, 1980, pp.101-114.

[16] Hamed, G. R., "Tack and Green Strength of NR, SBR, and NR/SBR Blends", **Rubber Chemistry and Technology**, Vol. 54, 1980, pp.403-412.

[17] Boenig, H. V., Miller, C. B., and Shottafer, J. E., "Tack in Urethan Elastomers", **Rubber Chemistry and Technology**, Vol. 39, 1966, pp.974-981.

[18] Bothe, L. and Rehage, G., "Autohesion of Elastomers", **Rubber Chemistry and Technology**, Vol. 55, 1981, pp.1308-1327.

[19] Chapman, A. J., **Heat Transfer**, 4th ed., Macmillan Publishing Company, New York, 1984, p.8.

[20] Reddy, J. N., **An Introduction to the Finite Element Method**, McGraw Hill Book Company, New York, 1984, pp.424-437.

[21] Reddy, J. N., **An Introduction to the Finite Element Method**, McGraw Hill Book Company, New York, 1984, p.51.

[22] Su, K. B., "Mechanisms of Interlaminar Fracture in A Thermoplastic Matrix Composite Laminate", Engineering Technology Laboratory, E. I. du Pont de Nemours & Co., Wilmington, DE 19898.

[23] Wilkins, D. J., Eisenmann, J. R., Camin, R. A., Margolis, W. S. ,and Benson, R. A., "Characterizing Delamination Growth in Graphite-Epoxy ", **Damage in Composite Materials, ASTM STP 775**, K. L. Reifsnider, Ed., American Society for Testing and Materials, Philadelphia ,1982, pp.168-183.

[24] Leach, D. C., Curtis, D. C., and Tamblin, D. R., " Delamination Behavior of Carbon Fiber/Poly(etheretherketone)(PEEK) Composites", **Toughened Composites, ASTM STP 937**, Norman J. Johnston, Ed., American Society for Testing and Materials, Philadelphia, 1987, pp.358- 380.

[25] Keary, P. E., Ilcewicz, L. B., Shear, C. ,and Trostle, J., "Mode I Interlaminar Fracture Toughness of Composites Using Slender Double Cantileverd Beam Specimens", **Journal of Composite Materials**, Vol.19, March, 1985, pp.154-177.

[26] Hunston, D. L., Moulton, R. J., Johnston, N. J., and Bascom, W. D. , "Matrix Resin Effects in Composite Delamination: Mode I Fracture Aspects", **Toughened Composites, ASTM STP 937**, Norman J. Johnston, Ed., American Society for Testing and Materials, Philadelphia, 1987, pp.74-94.

[27] Crick, R. A., Leach, D. C., and Moore, D. R., "Interpretation of Toughness in Aromatic Polymer Composites Using a Fracture Mechanics Approach", **SAMPE Journal**, Nov./Dec., 1986, Vol.22-6, pp.30- 36.

[28] Hinkley, J. A., Johnston, N. J., and O'Brien, T. K., "Interlaminar Fracture Toughness of Thermoplastic Composites", **NASA Technical Memorandum 100532**, Feb, 1988.

[29] Martin, R. H., "Effect of Initial Delamination on G_{IC} and G_{IR} Values from Glass/Epoxy Double Cantilever Beam Tests", Proceedings of the American Society for Composites, Third Technical Conference, Sept. 25-29, 1988, Stouffer-Madison Hotel, Seattle , Washington.

[30] Devitt, D. F., Schapery, R. A., and Bradley, W. L., "A Method for Determining the Mode I Delamination Fracture Toughness of Elastic and Viscoelastic Composite Materials", **Journal of Composite Materials**, Vol.14, Oct., 1980, pp.270-285.

[31] Leach, D. C., "Tough and Damage Tolerant Composites", ICI Advanced Materials, P.O. Box 54, Wilton, Middlesbrough, Cleveland, TS6 8JA, England.

[32] Chamis, C. C., "Simplified Composite Micromechanics Equations for Hydral, Thermal and Mechanical Properties", 38th Annual Conference, Reinforced Plastics/Composites Institute, The society of the Plastics Industry, Inc., Feb.7-11, 1983.

[33] Springer, G. S. and Tsai, S. W., "Thermal Conductivities of Unidirectional Composite Materials", **Journal of Composite Materials** , Vol.1, 1967, pp.166-173.

[34] Jones, R. M., **Mechanics of Composite Materials**, Scripta Book Company, Washington, D. C., 1975, p.87.

[35] Lambert, J. D., **Computational Methods in Ordinary Differential Equations**, p.241.

[36] Chapman, A. J., **Heat Transfer**, 4th ed, Macmillan Publishing Company, New York, 1984, p.316.

The vita has been removed from the scanned document